Design and Fabrication of Centre Frequency and Bandwidth Tunable Cavity Filters

by

Mitra Nasresfahani

A thesis
presented to the University of Waterloo
in fulfillment of the
thesis requirement for the degree of
Master of Applied Science
in
Electrical and Computer Engineering

Waterloo, Ontario, Canada, 2014

I hereby declare that I am the sole author of this thesis. This is a true copy of the thesis, including any required final revisions, as accepted by my examiners.

I understand that my thesis may be made electronically available to the public.

Abstract

To facilitate efficient utilization of limited and expensive frequency spectrum in communication systems, fully tunable filters are highly demanded. Realizing a constant absolute bandwidth, a reasonable return loss, and a high Q value over a relatively wide tuning range are some of the challenges in developing tunable filters for real system applications. This thesis deals with the design and implementation of combline cavity filters with bandwidth and centre frequency tunability. Cavity filters offers high Q and good power handling capability.

This dissertation is organized in three parts. In the first part, we study the design of constant absolute bandwidth tunable filters. We first design and implement a 5-pole C-band Chebyshev tunable filter with 40 MHz bandwidth and frequency tuning range of $4.9-6$ GHz. The inter-resonator coupling elements are realized using horizontal irises. The fabricated filter exhibits a stable response over the tuning range with a bandwidth variation of $\pm 5.3\%$. We then exploit semi-vertical irises to realized adjacent coupling values in a 7-pole X-band Chebyshev tunable filter with 80 MHz bandwidth and frequency tuning range of $7-7.9$ GHz. The fabricated filter reveals a stable response over the tuning range with a bandwidth variation of $\pm 6.7\%$. We also show that using vertical irises, the normalized coupling values remain almost independent of the cavity resonant frequency. This is in contrast to horizontal or semi-vertical irises where a tedious optimization is required to achieve the same goal.

In the second part, the objective is to design a fully tunable filter with wide tuning range. To achieve bandwidth tuning, two tunable filters are cascaded. Due to the wide tuning range and large bandwidth requirements, each individual filter can not maintain a constant absolute bandwidth over the tuning range. Since only the cascaded response matters, the concept of constant return loss design is introduced where the return loss remains constant while the bandwidth could change over the tuning range. All the inter-resonator coupling elements as well as normalized input and output impedances should

scale with the same factor in a constant return loss design. We show that this requirement can be achieved by careful design of filter geometry for a 6-pole tunable Chebyshev filter with tuning range of $1.8 - 2.6$ GHz. Despite the large bandwidth variation ($\pm 12.8\%$), the return loss of the fabricated filter is better than 15 dB over the tuning range. Two of such filters are then cascaded by an isolator to provide the bandwidth tunability. The cascaded response exhibits a tunable bandwidth of $20 - 100$ MHz.

In the third part, the focus is on the design of a fully tunable two-port triplexer in which three fully tunable bandpass filters are connected together through input and output manifolds. After designing three fully tunable filters, manifold dimensions are optimized in ADS circuit simulator. Simulation results show that the bandwidth and centre frequency of each band can be independently tuned.

Acknowledgements

I would like to express my sincere gratitude to my advisor, Professor Raafat Mansour for his continuous guidance and encouragement throughout the course of my graduate studies. I have had a great opportunity to work with him and have learned a lot from him throughout the course of my MSc research. I wish to thank him for his support which was not limited to research work.

It was such a great opportunity for me to be a member of the Centre for Integrated RF Engineering (CIRFE) research group. I would like to specially acknowledge Dr. Siamak Fouldai for always being available to provide guidance and for endless support; to Mostafa Azizi for his valuable insight and fruitful discussions during these years; to Dr. Fengxi Huang for his collaboration on this research; to Dr. Sara Attar for always encouraging and listening to me and for being a great office-mate, and to Marco Iskandar for the joint work on other interesting research topics. I am also indebted to Bill Jolley, the CIRFE lab manager, for his support and friendship.

I would also like to recognize my colleagues Ahmed Abdel Aziz, Sormeh Sotodeh, Dr. Neil Sarkar, Saman Nazari, Bahaedinne Jlassi, Desireh Shojaei, and Raisa Pesel. I would like to extend my gratitude to all members of the CIRFE research group.

My warm wishes and thanks go as well to my dear friends Noushin Shiran, Bahador Biglari, Alexandra Sevastianova, and many other friends who have enriched my life beyond my studies.

I would like to thank my parents, Maryam Malekahmadi and Morteza Nasresfahani, my brother Mohammad, and my grand mother Fereshteh Sajjadi for their support and encouragement throughout my life. Last but not least, I would like to express my warmest gratitude to my beloved husband, Akbar, for his endless support, patience, and encouragements, without which I would not achieve this.

To my beloved husband, Akbar,
for his dedicated support,
to my lovely boy,
and to my family.

Table of Contents

List of Tables **xv**

List of Figures **xvii**

1 Introduction **1**

1.1 Motivation 1

1.2 Objectives 2

1.3 Thesis Outline 3

2 Literature Review **5**

2.1 Introduction 5

2.2 Tunable Centre Frequency Filters 7

2.3 Constant Bandwidth Tunable Filters 8

2.4 Fully Tunable Filters 10

2.4.1 Fully tunable filters using extra elements for coupling adjustment . 10

2.4.2 Fully tunable filters based on dual band structures 11

2.4.3 Fully tunable filters based on cascading two tunable filters 13

2.5 Tunable multiplexers 14
2.5.1 Tunable diplexers 15
2.5.2 Tunable triplexers 17

3 Tunable Filters with Constant Absolute Bandwidth 21

3.1 Introduction 21
3.2 Design Principles 22
3.2.1 Theoretical Background 22
3.2.2 Tunable Resonator Design 26
3.2.3 Inter-resonator Coupling Design 28
3.2.4 Input/Output Coupling Design 32
3.2.5 Design Optimization 33
3.3 5-pole Filter Design 41
3.3.1 Resonator Design 41
3.3.2 Inter-resonator Coupling Design 43
3.3.3 Input/Output Coupling Design 44
3.3.4 EM Simulation Results 45
3.3.5 Measurement Results 45
3.4 7-pole Filter Design 50
3.4.1 Resonator Design 50
3.4.2 Inter-resonator Coupling Design 51
3.4.3 Input/Output Coupling Design 53
3.4.4 EM Simulation and Measurement Results 55
3.5 Conclusions 58

4 Fully Tunable Bandpass Filters with a Wide Tuning Range 59

4.1 Introduction . . . 59

4.2 Objectives . . . 60

4.3 Theoretical Background . . . 61

4.3.1 Constant Return Loss Filter Design . . . 61

4.3.2 Cascading Element Design . . . 63

4.4 6-pole Filter Design . . . 65

4.4.1 Design . . . 66

4.4.2 Measurement and Test Results . . . 69

4.5 Conclusions . . . 76

5 Fully Tunable Two Port Triplexer Design 77

5.1 Introduction . . . 77

5.2 Objective . . . 78

5.3 Proposed Method . . . 78

5.4 Filter Design . . . 80

5.4.1 Coupling Routing Diagrams . . . 80

5.4.2 Low Pass Filter Design . . . 83

5.4.3 High Pass Filter Design . . . 88

5.5 Manifold Design . . . 95

5.6 Simulation Results . . . 96

5.7 Conclusions . . . 98

6 Conclusions **99**

6.1 Contributions 99

6.2 Future Work 101

APPENDICES **103**

A TULA motor control **105**

Bibliography **109**

List of Tables

3.1 Cubical resonator's dimensions. 42

3.2 Optimized iris sizes to attain constant coupling for different coupling values. 43

3.3 Probe dimensions for constant input/output coupling. 44

3.4 7-pole resonator's dimensions. 50

3.5 Optimized iris dimensions to achieve constant normalized couplings in the 7-pole Chebyshev tunable filter. 52

3.6 Probe dimensions for constant input/output coupling. 54

5.1 Frequency and bandwidth tuning requirement for the two port triplexer . . 78

List of Figures

2.1 The side view of in-line irises 9

2.2 Measured tuning performance 10

2.3 2-pole tunable filter and its circuit model 10

2.4 Measured Fully tunable 2-pole filter performance. 11

2.5 Equivalent circuit model of dual-band combline filter 12

2.6 Measured bandwidth tuning performance 12

2.7 4-pole elliptic filter structure using long and short irises 13

2.8 Cascaded fully tunable filter transmission response 14

2.9 Schematic layout of the tunable diplexer 15

2.10 Measured results of tunable diplexer 16

2.11 Triplexer filter bank layout 18

2.12 Tuning response of three tunable filters in a filter bank 18

2.13 Two port triplexer layout 19

2.14 Triplexer filter bank layout 20

3.1 Impact of λ variations on filter shape for a six pole filter with BW = 100 MHz and RL = 20 dB: The coupling matrix $\mathbf{M}$ and the normalized impedance matrix $\mathbf{R}$ are held constant in the tuning range. 23

3.2 Combline tunable resonator with tuning disk 27
3.3 Schematic diagram of two coupled resonators using horizontal iris. 28
3.4 Normalized coupling variation vs. gap in a horizontal iris for different iris heights. 29
3.5 An iterative procedure to optimize the horizontal iris dimensions to achieve a constant normalized coupling. The same procedure can be applied to optimize the input/output probe dimensions. 30
3.6 Schematic diagram of two coupled resonators using a vertical iris. 31
3.7 Normalized coupling variation vs. gap in a vertical iris for different iris openings. 32
3.8 Schematic diagram of the input/output resonator loaded with a long probe 33
3.9 Group delay peak variation vs. resonant frequency for different L_{pr} values. 34
3.10 Schematic of the coarse model in ADS simulator 36
3.11 HFSS simulation of inter-resonator coupling vs. iris window length 37
3.12 HFSS simulation of normalized input/output impedance vs. probe length. 38
3.13 EM model for calculating resonant frequency, including the effect of irises. 39
3.14 Self-resonator coupling versus the Gap calculated from HFSS simulation results. 40
3.15 Coupling-routing diagram of the 5-pole filter. 41
3.16 The resonant frequency and unloaded Q versus gap size: HFSS simulation result 42
3.17 EM simulation results of adjacent normalized coupling over the tuning range 43
3.18 EM simulation result of group delay over the tuning range. 44
3.19 EM model of 5-pole tunable filter. 45

3.20 EM simulated tuning performance of the 5-pole filter 46
3.21 Fabricated 5-pole bandpass tunable filter. 47
3.22 Measured tuning response of the 5-pole tunable filter. 48
3.23 Measured group delay response of the 5-pole filter. 49
3.24 Coupling-routing diagram of the 7-pole tunable Chebyshev filter. 50
3.25 Simulation results of resonant frequency and unloaded Q vs. gap size for a cylindrical resonator made from copper or aluminium. 51
3.26 Schematic diagram of two coupled resonators using a semi-vertical iris. . . 52
3.27 EM simulation results of adjacent normalized coupling over the tuning range. 53
3.28 EM simulation of the reflection coefficient group delay of the first resonator over the tuning range. 54
3.29 EM model of the 7-pole tunable filter with absolute constant bandwidth. . 55
3.30 EM and ideal response of the 7-pole constant bandwidth tunable filter at the middle of the tuning range. 55
3.31 Physical structure of the 7-pole filter. 56
3.32 Measured tuning response of the constant bandwidth 7-pole tunable filter. 57

4.1 Coupling-routing diagram of the six-pole Chebyshev filter. 60
4.2 Scaling the coupling matrix and normalized input and output impedance of a six pole Chebyshev filter for $\gamma = 0.7, 1.4$. 62
4.3 Impact of mismatch in scaling of the coupling matrix and normalized input/output impedance on return loss of a six pole Chebyshev filter with $RL = 25$ dB. 63
4.4 Two filters cascaded through an interconnecting two-port network 64

4.5 EM simulation results of the tunable resonator 66
4.6 Scaling factor of coupling elements and normalized input/output impedance across the tuning range. 67
4.7 EM model of the 6-pole Chebyshev filter 68
4.8 EM simulation response of the 6-pole tunable filter. 68
4.9 Measured response of the 6-pole filter over the tuning range. 69
4.10 Cascading two 6-pole filters using an isolator. 70
4.11 Measured results of fully tunable filter. 71
4.12 Transmission and return loss responses of the filter for different bandwidths over the tuning range. 72
4.13 Cascading two 6-pole filters using Coaxial line. 73
4.14 Measured cascaded response using different interconnecting networks. . . . 74
4.15 Transmission and return loss responses of the filter for different bandwidths over the tuning range. 75

5.1 Proposed fully tunable two port triplexer structure 79
5.2 Coupling routing diagram for a 4-pole Chebyshev filter with one transmission zero 80
5.3 Alternative coupling routing diagrams for having a transmission zero on the left side of the passband 82
5.4 Ideal frequency response of the low-pass and high-pass filters 82
5.5 Coupling-routing diagram for realizing asymmetric 4-pole filter. 84
5.6 Structure of the low-pass filter 85
5.7 EM simulation results of 4-pole low-pass filters for different frequency bands 85

5.8 Measurement results for the first band filter across the tuning range. 86

5.9 Measurement results for the second band filter across the tuning range. . . 87

5.10 Measurement results for the third band filter across the tuning range. . . . 87

5.11 Impact of the parasitic coupling $M_{14} = 0.03$ on the filter response for two different realizations of the box section configuration. 88

5.12 Structure of the high-pass filter in the box section configuration. 89

5.13 EM simulation results of 4-pole high-pass filters for different frequency bands using the box section configuration. 90

5.14 Measured response of the third band 4-pole high-pass filter with box section configuration. Note that the same filter can be tuned such that the transmission zero will appear on the right side of the passband. 91

5.15 EM simulation results for the second band elliptic filter across the tuning range. 92

5.16 Measurement results for the first band elliptic filter across the tuning range. 93

5.17 Measurement results for the second band elliptic filter across the tuning range. 93

5.18 Measurement results for the third band elliptic filter across the tuning range. 94

5.19 The measured cascaded response of all three bands. 94

5.20 Two port triplexer response in ADS circuit simulator using optimized manifold lengths. 96

5.21 Bandwidth and centre frequency tuning of the two port triplexer in ADS circuit simulator. 97

A.1 Piezoelectric motor assembled on top of the resonator. 106

Chapter 1

Introduction

1.1 Motivation

Filters are key components in many RF/microwave systems including satellite, radar, and cellular telecommunication systems. The complex requirements of modern communication systems enforce more stringent requirements on the design of RF/microwave filters. RF/microwave tunable filters have received considerable attention in communication systems due to their potentials to reduce the system size, complexity, and cost. For example, since the centre frequency or bandwidth of a tunable filter can be electronically controlled remotely, one installation of a tunable filter can serve many years as it can be easily adjusted to meet the future requirements.

Maintaining a constant absolute bandwidth over the tuning range of a filter is highly desired in some applications. This is the case in systems which are designed for a fixed baud rate or systems that have a fixed-bandwidth baseband infrastructure. Even though various methods have been proposed to maintain constant absolute bandwidth as the passband frequency is tuned, most of them relies on some kind of compensation circuit which adds to the tuning complexity. It was recently shown in [1] that the absolute bandwidth can

maintain constant by careful design of filter geometry and without using any compensation circuit. This attractive approach is explored in detail in this study.

To efficiently support multiple frequency bands in the next generation wireless networks, the RF front end needs to be fully configurable. A fully tunable bandpass filter is essential to support multiple frequency band coverage in a small form factor. In a fully tunable filter, both centre frequency and bandwidth are tunable. A common approach to achieve bandwidth tunability is to cascade two tunable filters. Each individual tunable filter needs to maintain a stable return loss over the tuning range. Constant return loss design is more general than constant absolute bandwidth design in that the bandwidth can change over the tuning range. The theory and experiment of constant return loss filters are investigated in this study.

Supporting multi-band and multi-standard communication is an important requirement in the next generation cellular systems. To support multi-band communication, multiple fully tunable filters need to be integrated in a switch-less filter bank. Manifold coupled multiplexers are common structure to channelize/combine several frequency channels. Tunable two-port multiplexers, where a number of tunable filters are connected to each other using manifolds at the input and output, is an attractive solution to support multi-band/multi-standard communication. Two-port triplexer design will be explored in this thesis.

1.2 Objectives

The objective of this study is to explore the theory and design of fully tunable (centre frequency and bandwidth) cavity combline filters. In specific, the following research topics are investigated in this thesis:

- Theory and design of constant absolute bandwidth tunable filters.
- Theory and design of constant return loss tunable filters.

- Theory and design of two-port tunable triplexers.

1.3 Thesis Outline

In Chapter 2, relevant literature on tunable filters, constant absolute bandwidth tunable filters, and tunable multiplexers are reviewed. Chapter 3 presents the theory and design of constant bandwidth tunable filters for combline cavity filters. In Chapter 4, fully tunable filters with a wide tuning range are investigated where the concept of constant return loss filter design is introduced. The theory and design of two-port fully tunable triplexers are addressed in Chapter 5. In Chapter 6, a summary of the thesis contribution and suggestions for future research are provided.

Chapter 2

Literature Review

2.1 Introduction

Microwave filters serve as key components in satellite and cellular telecommunication systems. Despite substantial advances in the area of microwave filter design, the complex requirements of the modern communication systems still call for development and furtherance of microwave filter theory.

Coupling matrix representation is a powerful and yet general method to synthesize microwave filters. In this representation, a bandpass filter is represented by a number of microwave resonators coupled to one another where *coupling* means exchange of electromagnetic energy. This representation provides some key advantages relative to the classical element extraction method: First, each individual physical component of the filter is in a one to one correspondence with an element in the coupling matrix. Second, the coupling matrix can be tailored to match any particular filter structure through so called similarity transformations. Third, the coupling matrix can naturally support asymmetric characteristics with transmission zeros. These features are essential in order to achieve the stringent specifications of the current microwave systems.

CHAPTER 2: Literature Review

In-band linearity (small group delay variation in passband), out-of-band selectivity (high rejection close to passband), low loss (high Q), and compact size (small form factor) are the main desired characteristics of a microwave filter. In tunable filters, additional requirements are maintaining a stable frequency response across the tuning range and achieving a relatively wide tuning range. Realizing an absolute constant bandwidth, a reasonable return loss, and a high Q value over a relatively wide tuning range are some of the challenges in developing tunable filters for real system applications [1, 2].

Microwave tunable filters are usually designed for a single passband[†]. In multi-channel communication systems, a multi-port network, commonly referred to as a multiplexer, is required to separate/combine different frequency channels. A common application of multiplexers is in cellular base stations wherein several microwave signals interface with a common port of an antenna system [3]. Tunable multiplexers are required to enable multi-band selection for next generation wireless systems. The main challenge in designing a tunable multiplexer is to minimize the interaction between channel filters.

In this chapter, we examine some of the existing literature on tunable filters/multiplexers: In the first section, the focus would be on microwave filters with tunable centre frequency. Bandwidth is usually changed in these filters when the tuning range is wide. In the next section, we review relevant works on microwave filters with a constant absolute bandwidth and tunable centre frequency. Next, existing works on fully tunable microwave filters (tunable bandwidth and tunable centre frequency) are reviewed. Finally, a review of literature on tunable multiplexers is presented.

[†]Note that multiple passband filters do not easily lend themselves to independent tuning of different bands.

2.2 Tunable Centre Frequency Filters

Different tuning mechanisms have been developed to achieve centre frequency tuning in microwave filters including mechanical, electrical, magnetic, and micro electromechanical system (MEMS) tuning. Tuning methods are evaluated in terms of different metrics including their tuning range, quality factor, power handling capability, fabrication complexity, size, and tuning speed. None of the tuning mechanisms is superior in terms of all metrics and therefore depending on the application and design constraints, each tuning method might be preferred over the other.

Mechanical tuning is based on physical movement of an element to tune the centre frequency of the resonators. For example, in a combline resonator, the height of the tuning disk above the metallic post is mechanically adjusted through tuning screws and thereby the capacitance between the metallic post and the tuning disk is adjusted [4]. Mechanical tuning structures enjoy easy fabrication, high Q, and high power handling capability and have been realized in dielectric resonator, coaxial, and waveguide configurations [5,6]. However, they are bulky and suffer from low tuning speed. The tuning speed can be improved by automated tuning using piezoelectric or stepper motors instead of hand tuning [7]. Tuning a combline resonator in the lower frequency ranges requires a larger penetration of tuning screws inside the cavity which leads to a Q degradation. In [8], an alternative method is presented where a disk moves radially instead of up/down over the metallic post. Therefore, the volume of metal inside the resonator is not changed which gives a constant Q over the fairly wide tuning range.

In magnetic tuning, a ferrite material, usually Yttrium-Iron-Garnet (YIG), whose magnetic intensity can be controlled by an external voltage is exploited to control the magnetic field pattern inside the resonators. Magnetically tuned dielectric resonators using ferrite material have been reported in [9]. The YIG magnetically tunable filters offer an ultra-wideband tuning range. However, they are usually bulky/heavy and are not efficient in terms of power consumption.

In electrical tuning, semiconductor diode varactors are exploited as variable capacitors whose capacitance are adjusted by the applied reverse bias voltage. Semiconductor varactors are compact and easily tunable and have been extensively used in planar filter configurations such as microstrip line filters, and suspend strip-line filters. However, their tuning range is limited and their quality factor degrades as the capacitance gets bigger.

In MEMS tuning, the state or capacitance value of a electro-mechanical device is changed according to the external applied DC voltage. MEMS switches have been exploited in microstrip tunable filters, CPW filters, lumped element filters , and cavity filters [4, 10–14]. While MEMS have a small size, their integration with 3-D high-Q resonators is challenging. Also, to cover a wide tuning range using MEMS tuning, a high order switched capacitor bank is required which usually yields high losses [2].

2.3 Constant Bandwidth Tunable Filters

In tunable filters, maintaining a stable frequency response across the tuning range and achieving a relatively wide tuning range are challenging. In tuning procedure, the variation of inter-resonator coupling is different from input/output coupling with respect to centre frequency. This leads to deterioration in return loss response. To maintain a constant bandwidth, one solution is to add tuning elements such as semiconductor varactors and MEMS to control both inter-resonator and input/output coupling values over the tuning range of the filter. In planar tunable filters, semiconductor varactors and MEMS devices are employed to control the bandwidth over the tuning range [15,16]. Planar super conductive tunable filters with constant absolute bandwidth have been reported in [17,18]. They have a high quality factor, but they are bulky and have low operating temperature. Cavity filters with capability of tuning both centre frequency and bandwidth have been reported in [19]. Cavity filters usually offer a high quality factor and good power handling capability.

A Ku-band high-Q tunable elliptic filter with a stable bandwidth and transmission

zeros has been presented in [20]. The 4-pole elliptic filter has been realized using two dual-mode cylindrical resonators operating in the TE_{113} mode. The flexible bellow with two convolution is mounted on the top of the resonator for realizing the frequency tuning. The cavity length is adjusted through the expansion or compression of the bellows. To maintain the bandwidth constant, both input/output and cross couplings need to be independent from frequency variation. To this end, the in-line irises have been used to realize the inter-resonator coupling. The side view of the inline irises is depicted in Fig 2.1

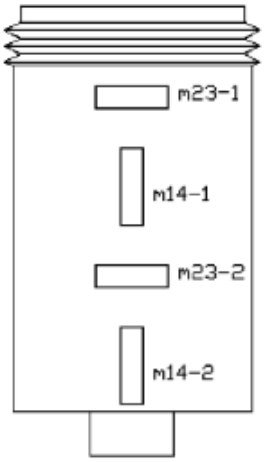

Figure 2.1: The side view of in-line irises [20].

In order to have the lowest variation in input/output coupling, the dual-slot iris is positioned at the end of the cavities.

The measured tuning response of the filter is depicted in Fig. 2.2. One can see that filter covers the tuning range of 460 MHz from 11.74 to 12.2 GHz with a bandwidth variation of 10 MHz from 156 to 166 MHz (less than 3.5%). The filter maintains a high Q (extracted Q is around 8000) over the tuning range. There is deterioration in return loss in the both edges of the tuning range.

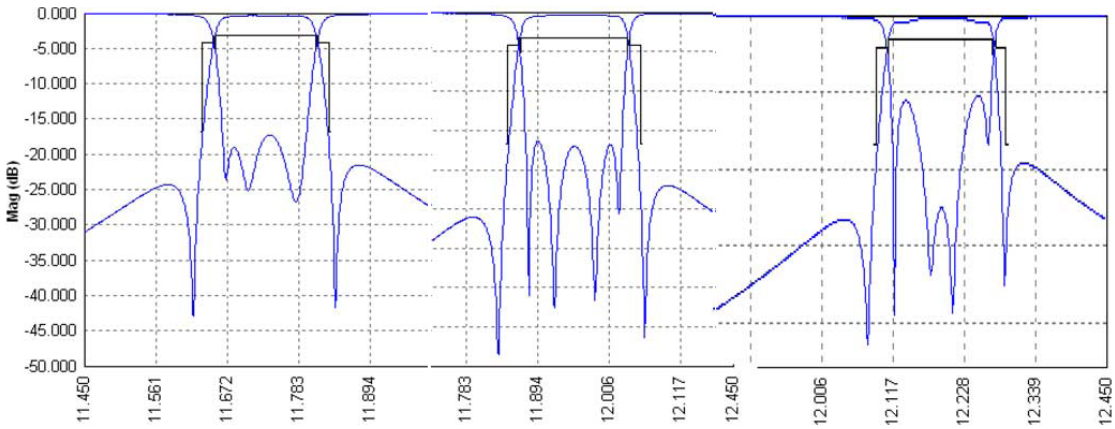

Figure 2.2: Measured tuning performance [20].

2.4 Fully Tunable Filters

2.4.1 Fully tunable filters using extra elements for coupling adjustment

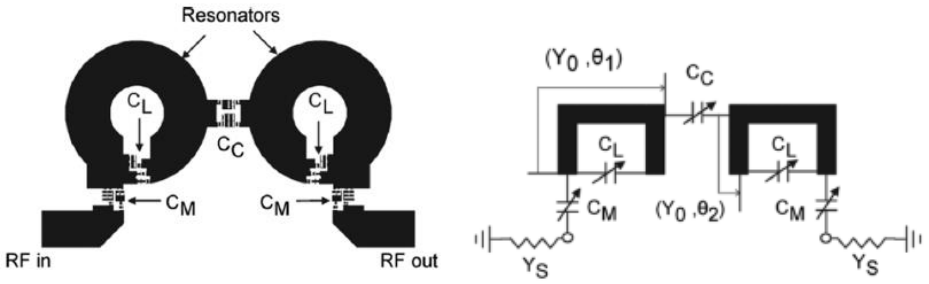

(a) 2-pole tunable filter (b) Circuit model

Figure 2.3: 2-pole tunable filter and its circuit model [21]

A high Q two-pole suspended fully tunable filter has been presented in [21] with a both bandwidth and center frequency tuning capability. In order to have high Q, the filter is implemented using suspended stripline resonators [22]. The MEMS systems capacitive

network is used to tune the both centre frequency and bandwidth. The filter structure and its circuit model are depicted in Fig. 2.3. One can see from this figure that the resonant frequency is tuned by varactor (C_L). Moreover, the inter-resonator coupling and input/output normalized impedance are controlled by varactors (C_c) and (C_M) respectively.

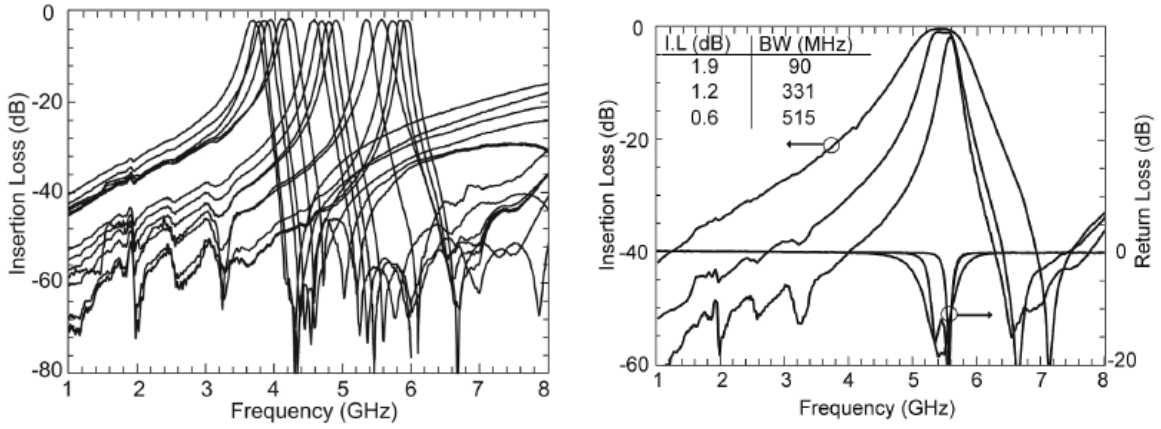

(a) Measured transmission responce of tunable frequency filter with a constant bandwidth

(b) Measured filter response with 1-dB bandwidth control.

Figure 2.4: Measured Fully tunable 2-pole filter performance [21]

The measured filter response cover the tuning range from 3.7 to 5.95 GHz as depicted in Fig. 2.4a. The bandwidth can be tuned at any frequency. Therefore, the filter can be tuned over tuning range with absolute constant bandwidth. As one can see from Fig. 2.4b, the 1-dB bandwidth is tuned from 90 to 515 MHz at 5.5 GHz.

2.4.2 Fully tunable filters based on dual band structures

A fully tunable filter based on dual band combline structure has been presented in [23]. In this method the lower frequency band-pass can be fully tuned without any coupling adjustment. As one can see from Fig. 2.5, each resonator of the band pass filter is coupled to a bandstop resonator. Therefore, The bandwidth can be increased if the centre frequency

of bandpass resonators shifted down by increasing the capacitance and the centre frequency of the bandstop shifted up by decreasing their capacitance. The resonators are manually tuned using an inserted screw on the top of each resonator.

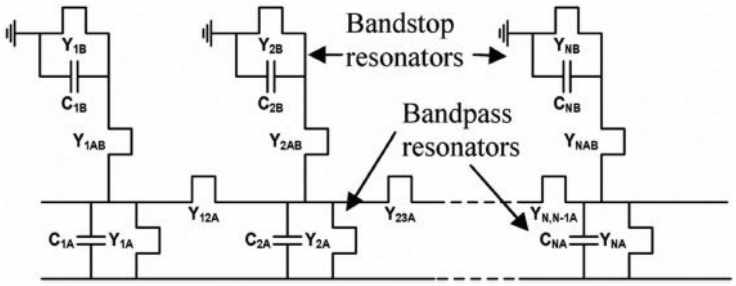

Figure 2.5: Equivalent circuit model of dual-band combline filter [23].

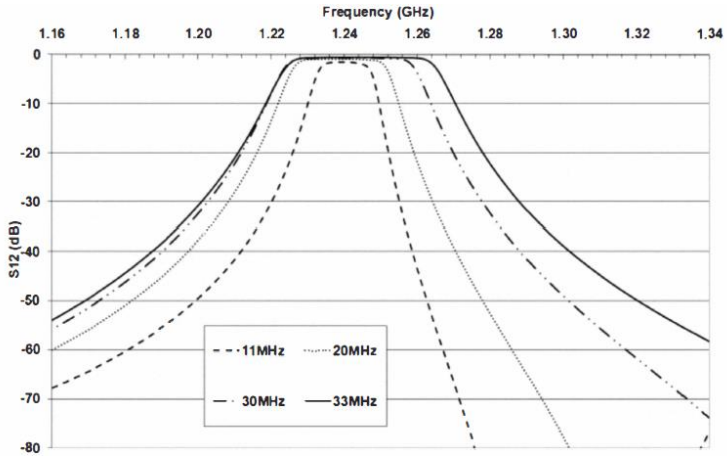

Figure 2.6: Measured bandwidth tuning performance [23].

It is worth to mention that due to the interaction between the bandpass and bandstop resonators, any change in the lower band affects the higher band response. The measured results of the lower passband bandwidth tuning are presented in Fig. 2.6. As one can see, the bandwidth can be adjusted over 300%.

2.4.3 Fully tunable filters based on cascading two tunable filters

A K_a-band fully tunable filter working in TE_{01} mode has been presented in [24]. The bandwidth tuning is realized by cascading two six pole filters. One of the filter has a high rejection on the left side using negative cross coupling (pseudo-high-pass filter). The other one has a high rejection on the right side (pseudo-Low-pass filter). The long (respectively short) irises with the length more than (respectively less than) half of the free space wavelength have been used to realize the positive (respectively negative) couplings. The 4-pole filter structure using long and short irises is depicted in Fig. 2.7. The proposed tunable metal-ring loaded TE_{01} cavity and long coupling irises are the key elements to realize a tunable filter with a stable in-band and rejection response. Both 6-pole filters cover the frequency range of 500 MHz with a stable response.

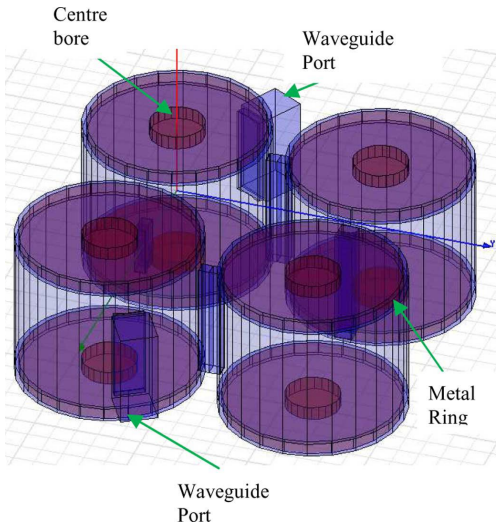

Figure 2.7: 4-pole elliptic filter structure using long and short irises [24].

Bandwidth tunability is realized by cascading two (low-pass and high-pass) tunable filters. The overlap of two filters determines the bandwidth of the cascaded filter. The measured cascaded filter covers the tuning range of 500 MHz while the bandwidth is tuned from 40 to 160 MHz as it is depicted in Fig. 2.8. In this method, both centre frequency

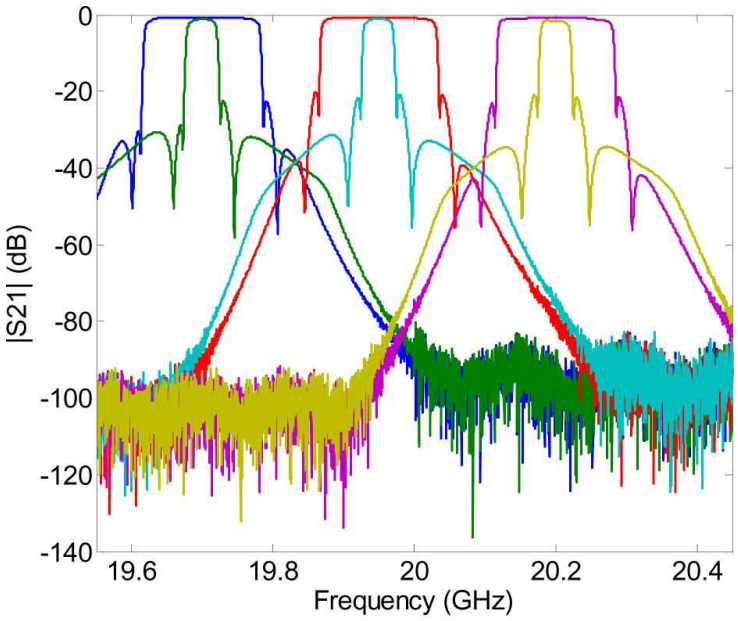

Figure 2.8: Cascaded fully tunable filter transmission response [24].

and bandwidth are tuned just by adjusting the centre frequencies of the constituent filters and without any coupling adjustment.

2.5 Tunable multiplexers

Supporting multi-band and multi-standard transmission/reception is an important requirement in the next generation cellular communication systems. Different methods are proposed for design and implementation of multiplexing networks including hybrid-coupled, circulator coupled, directional filter, and manifold-coupled multiplexer. [25–27]

2.5.1 Tunable diplexers

Different methods for design and implementation of tunable diplexers has been proposed. In [28], a tunable diplexer is presented based on a multilayer structure. In order to tune the band-pass and band-stop independently, a combination of high-pass, low-pass and band-pass filters are used.

Common-resonator method was used in [29] to design and implement a tunable diplexer. The two channels of the diplexer can be tuned independently or simultaneously. The silicon varactors are used to realize the frequency tuning; however, the varactor Q limits the filter performance. This method suffers from low Q which results from the varactor Q and microstrip resonator Q_u. Moreover, this method has a low power handling capability.

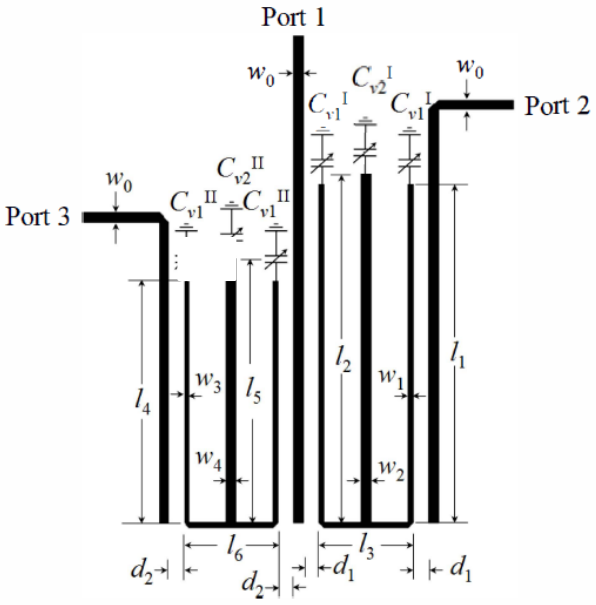

Figure 2.9: Schematic layout of the tunable diplexer [30].

A tunable microstrip diplexer based on varactor-tuned dual-mode stub-loaded has been presented in [30]. In order to design each channel filter independently, the dual coupling paths are used. The dual mode resonators are loaded by varactors to tune the centre

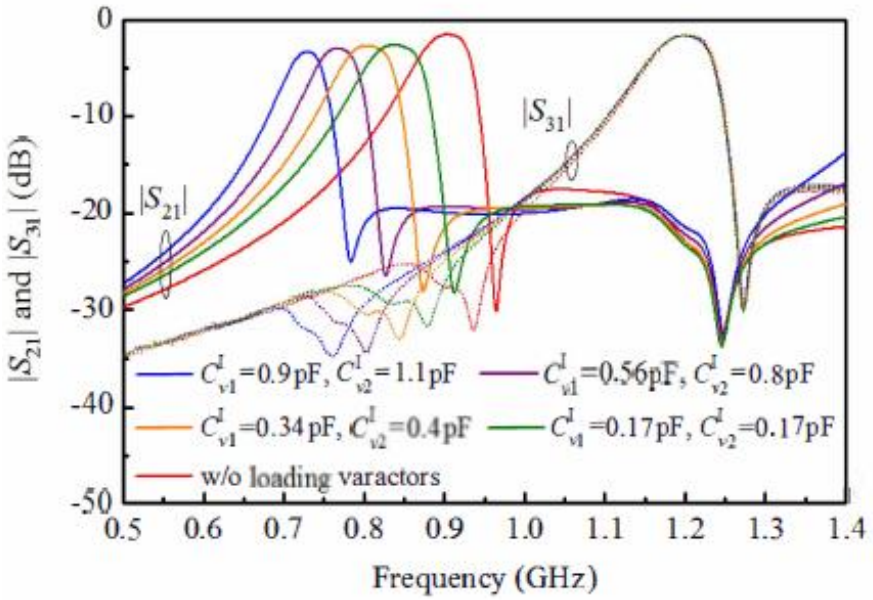

(a) Higher frequency channel is unchanged

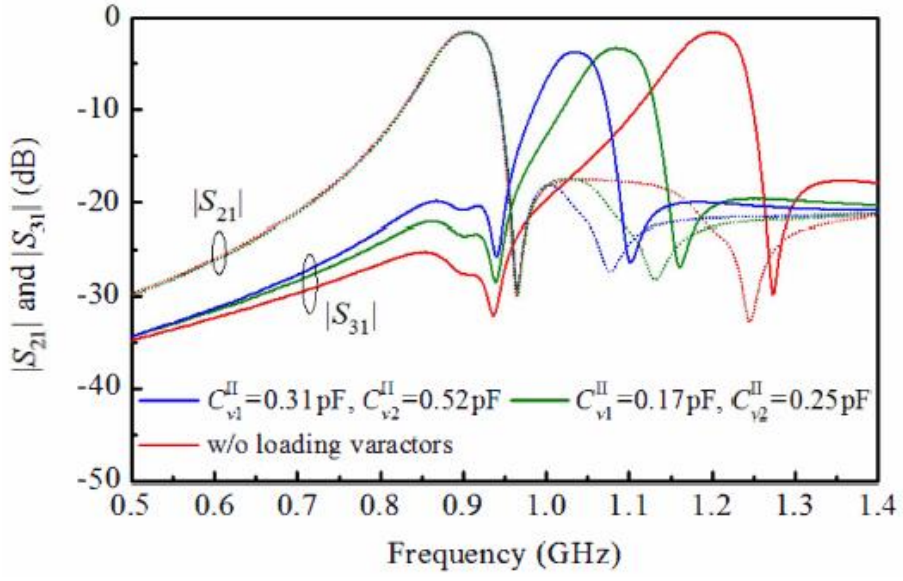

(b) Lower frequency channel is unchanged

Figure 2.10: Measured results of tunable diplexer [30]

frequency of each channel. The schematic layout of the tunable diplexer is depicted in Fig. 2.9. As can be seen, the lower (respectively higher) channel filter resonant frequency can be tuned by changing the capacitance C_{v1}^{I} and C_{v2}^{I} (respectively C_{v1}^{II} and C_{v2}^{II}) over a wide tuning range. In this method the two band can be tuned independently. As one can see, in Fig. 2.10a the lower band is tuned while the higher band is unchanged, and in Fig. 2.10b the higher band is tuned while the lower band is fixed. This design has a low Q factor which is due to the conductor loss. Moreover, the larger capacitance attributes more loss in the filter performance.

2.5.2 Tunable triplexers

Different methods have been used to design band-pass filters with tunable centre frequency and/or bandwidth. The multi band filters can be design by integration of such tunable bandpass filters. A lot of methods have been proposed on combining bandpass filters to select multiple bands [31, 32]. In this section we investigate the triplexer without/with switches.

A switchless triplexer has been presented in [33]. The triplexer is realized by integration of three 2-pole bandpass filters. Filters are working in a high Q evanescent mode. Moreover, their centre frequency can be tuned by adjusting the gap on top of their resonator posts using piezoelectric actuators. The input feed-line network is used to connect the three filters as is depicted in Fig. 2.13. As one can see, each filter is connected to a specific feed line. The feed line is designed carefully to achieve impedance match over the tuning range. It is worth mentioning that to match the input impedance over the tuning range, the length of the line should be smaller than $\lambda/4$. The triplexer covers the frequency range from 1.7 to 3.4 GHz. The bandwidth of each channel is smaller than 30 MHz. The measured performance of the triplexer is depicted in Fig. 2.12. As one can see, each channel can be tuned independently over the tuning range. This design has a very compact size and it achieves the insertion loss better than 4 dB over the tuning range.

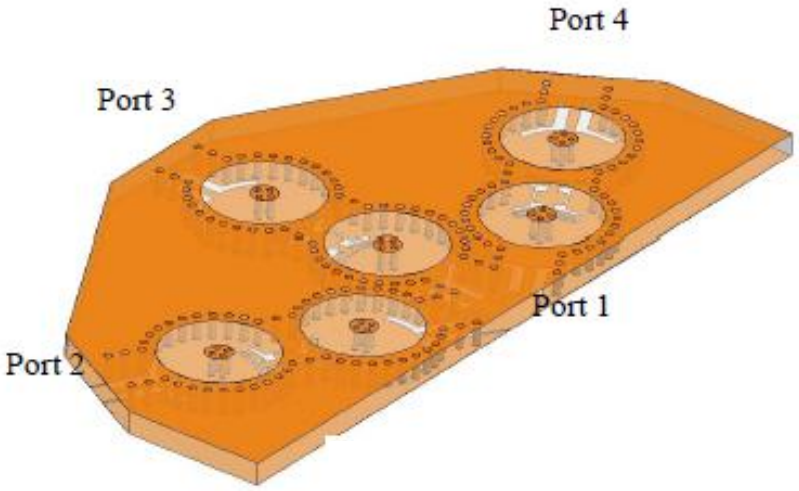

Figure 2.11: Triplexer filter bank layout [33].

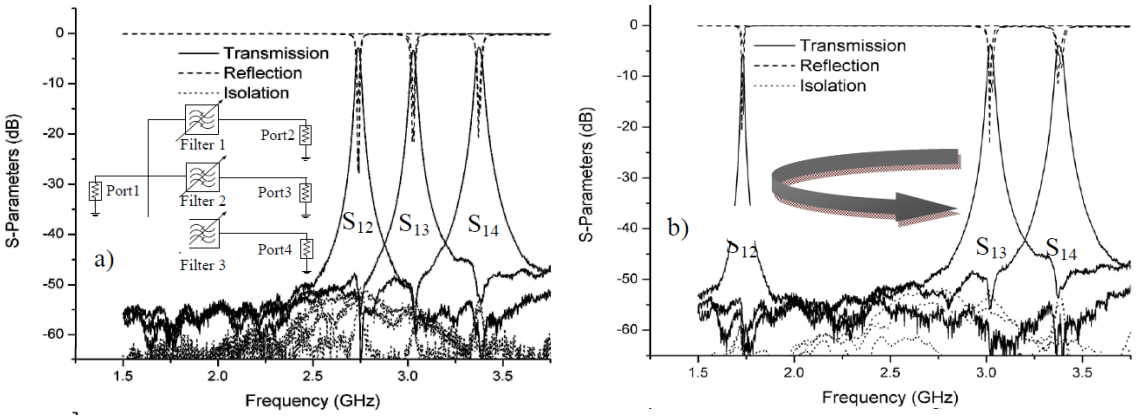

(a) Triplexer response (b) Lower channel is tuned

Figure 2.12: Tuning response of three tunable filters in a filter bank [33]

A manifold coupled switched two port triplexer has been presented in [34]. The triplexer consists of three 8-pole filters which are connected together using coupled manifolds. The triplexer layout is depicted in Fig. 2.13. Filters and manifolds are design separately using EM simulation. In the first step, the resonators are detuned using a piece of wire. Then, a MEMS cantilever beam switch is proposed for detuning the resonators. The transmission response of the manifold coupled switched triplexer is depicted in Fig. 2.14. As one can see, the rejection of the second channel can be tuned, by detuning different number of resonators. With the two, four, and six middle resonators detuned, the rejection of the second channel increased to 40, 60, and 80 dB. In this method, the filters are implemented with superconducting material. Therefore, the fabricated triplexer provides a fairly good insertion loss.

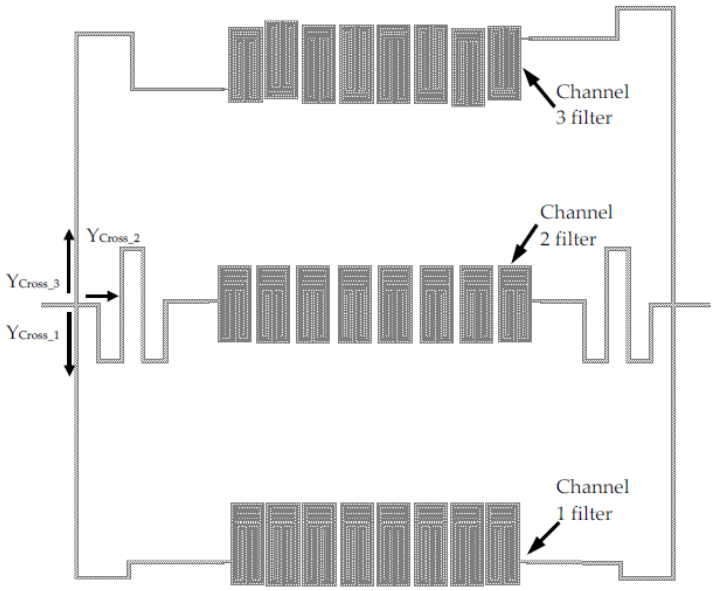

Figure 2.13: Two port triplexer layout [34].

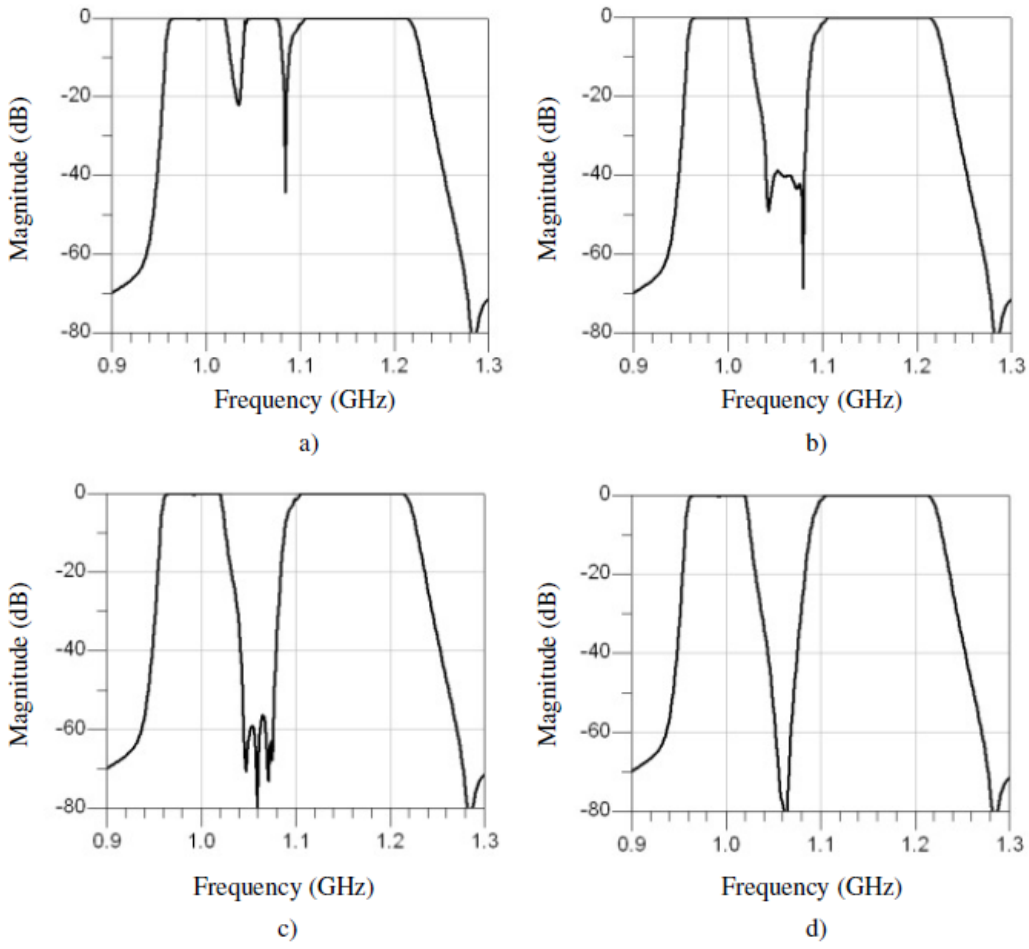

Figure 2.14: Two port triplexer response [34].

Chapter 3

Tunable Filters with Constant Absolute Bandwidth

3.1 Introduction

RF tunable filters have received considerable attention in multi-band communication systems in order to reduce the system size and complexity. In some applications, keeping the absolute bandwidth constant across the tuning range of the filter is highly desired. This is the case in systems which are designed for a fixed baud rate or systems that have a fixed-bandwidth baseband infrastructure. Generally speaking, in order to achieve a constant absolute bandwidth across the filter tuning range, not only the resonant frequencies of resonators but also the coupling coefficients among different resonators need to be controlled. It has been recently found in [1,35] that by careful design of filter geometry, one can make the coupling coefficients almost independent of the resonant frequencies of resonators. In specific, they designed a 4-pole S-band filter which operates at 2.45 GHz with a constant absolute bandwidth of 30 MHz. The filter achieves a stable response with ±3.7% MHz bandwidth variation over 400 MHz tuning range from 2.25 GHz to 2.65 GHz. In this chap-

ter, first an investigation is done on the design principles in [1]. Then this methodology is applied to the design of the following C-band and X-band cavity filters:

- a 5-pole filter operating at 5.5 GHz with a constant absolute bandwidth of 40 MHz which achieves a stable response with ±5.3% MHz bandwidth variation over 1100 MHz tuning range from 4.9 GHz to 6 GHz.
- a 7-pole filter operating at 7.5 GHz with a constant absolute bandwidth of 80 MHz which achieves a stable response with ±6.7% MHz bandwidth variation over 900 MHz tuning range from 7 GHz to 7.9 GHz.

3.2 Design Principles

3.2.1 Theoretical Background

Bandpass filters are usually consist of a number of resonators coupled to one another by coupling elements. The S parameters of a bandpass filter with centre frequency f_0 and bandwidth BW are described in terms of its coupling elements by

$$\begin{aligned} S_{11} &= 1 + 2jR_S[\lambda\mathbb{I}_N - j\mathbf{R} + \mathbf{M}]^{-1}_{11}, \\ S_{21} &= -2j\sqrt{R_S R_L}[\lambda\mathbb{I}_N - j\mathbf{R} + \mathbf{M}]^{-1}_{N1}, \end{aligned} \tag{3.1}$$

where $\mathbf{R}$ is the $N \times N$ normalized impedance matrix with all entries zero except for $[\mathbf{R}]_{11} = R_S$ and $[\mathbf{R}]_{NN} = R_L$, R_S is the normalized source impedance, R_L is the normalized load impedance, $\mathbb{I}_N$ is the $N \times N$ identity matrix, $\mathbf{M}$ is the $N \times N$ symmetric coupling matrix of the filter, and λ is the normalized frequency variable which is obtained from

$$\lambda = \frac{f_0}{BW}\left(\frac{f}{f_0} - \frac{f_0}{f}\right). \tag{3.2}$$

According to (3.1), one way to achieve a stable frequency response across a tuning range is to satisfy the following conditions

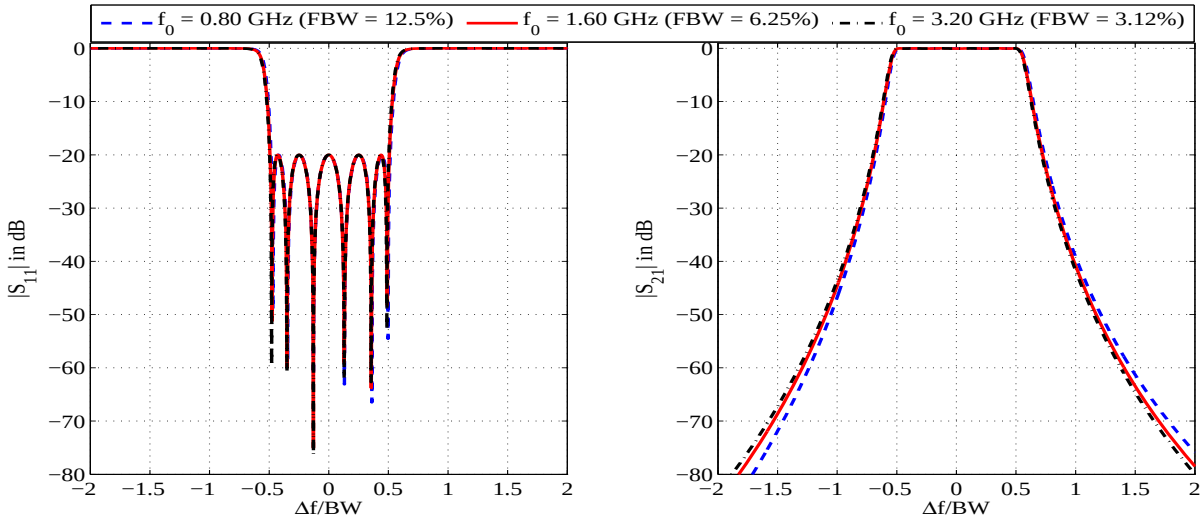

Figure 3.1: Impact of λ variations on filter shape for a six pole filter with $BW = 100$ MHz and $RL = 20$ dB: The coupling matrix $\mathbf{M}$ and the normalized impedance matrix $\mathbf{R}$ are held constant in the tuning range.

a) The frequency variable λ remains independent of the centre frequency.

b) The coupling matrix $\mathbf{M}$ and the normalized impedance matrix $\mathbf{R}$ are held constant over the tuning range.

For $f = f_0 + \Delta f$, one can write

$$\lambda = \frac{\Delta f}{BW}\frac{2 + \Delta f/f_0}{1 + \Delta f/f_0} \approx \frac{2\Delta f}{BW}, \qquad \Delta f/f_0 \ll 1. \tag{3.3}$$

That is if the fractional bandwidth ($FBW = BW/f_0$) of the filter remains small enough in the filter tuning range, λ will be almost independent of the centre frequency and a) is automatically satisfied. The dependency of the frequency response on the λ variations is illustrated in Fig. 3.1 for a 6-pole bandpass filter with a return loss of 20 dB and a bandwidth of 100 MHz. As it can be seen from this figure, the impact of λ variations on the filter response is negligible provided that the FBW of the filter does not change

drastically over the tuning range. In the rest of this study, we assume that λ is constant over the tuning range.

In order to realize constant inter-resonator coupling as well as normalized source/load impedances across the tuning range, we first need to relate these quantities to some experimentally measurable parameters of the filter. As we see in the following, these parameters are the physical coupling coefficients for the coupling elements and the group delay of the input/output reflection coefficient for the normalized source/load impedance.

Element $[\mathbf{M}]_{ij}$ of the coupling matrix represents the coupling between resonators i and j. The value of each coupling element generally depends on the filter structure as well as the filter bandwidth and centre frequency. More precisely,

$$[\mathbf{M}]_{ij} = \frac{f_0}{BW} k_{ij}, \tag{3.4}$$

where k_{ij} is the physical coupling coefficient between resonators i and j and is given by [3]

$$k_{ij} = \frac{1}{2}\left(\frac{f_0^{[i]}}{f_0^{[j]}} + \frac{f_0^{[j]}}{f_0^{[i]}}\right)\sqrt{\left(\frac{(f_{[e]}^{[ij]})^2 - (f_{[m]}^{[ij]})^2}{(f_{[e]}^{[ij]})^2 + (f_{[m]}^{[ij]})^2}\right)^2 - \left(\frac{(f_0^{[i]})^2 - (f_0^{[j]})^2}{(f_0^{[i]})^2 + (f_0^{[j]})^2}\right)^2}, \tag{3.5}$$

in which $f_0^{[i]}$ and $f_0^{[j]}$ are respectively the resonant frequencies of resonators i and j, $f_{[e]}^{[ij]}$ and $f_{[m]}^{[ij]}$ are respectively the even and odd resonant frequencies and are obtained by setting the appropriate boundary conditions between resonators i and j. Note that for a synchronous design, $f_0^{[i]} = f_0^{[j]} = f_0$ and (3.5) is reduced to

$$k_{ij} = \frac{(f_{[e]}^{[ij]})^2 - (f_{[m]}^{[ij]})^2}{(f_{[e]}^{[ij]})^2 + (f_{[m]}^{[ij]})^2} \tag{3.6}$$

One can use an EM simulator with an eigen-mode calculation capability such as HFSS to experimentally calculate $f_{[e]}^{[ij]}$ and $f_{[m]}^{[ij]}$. From (3.4), $[\mathbf{M}]_{ij}$ remains constant across the tuning range for a constant bandwidth tunable filter provided that $f_0 k_{ij}$ remains constant as the centre frequency changes. In other words,

$$f_0 k_{ij} = [\mathbf{M}]_{ij} BW = \text{constant}. \tag{3.7}$$

Therefore, for a constant bandwidth tunable filter, k_{ij} should be inversely proportional to the centre frequency f_0.

The normalized impedances R_S and R_L can be extracted from the group delay of the reflection coefficient at the input and output resonators, respectively. Let $\tau(w)$ denote the group delay of the input/output reflection coefficient of the filter. That is

$$\tau(\omega) = -\frac{\partial \angle S_{ii}}{\partial \omega}, \quad i = 1 \text{ or } 2 \tag{3.8}$$

Then, the normalized input/output impedance R is given by [3]

$$R = \frac{4}{2\pi BW \tau(\omega_0)}, \tag{3.9}$$

where $\omega_0 = 2\pi f_0$. Note that the group delay attains its maximum value at the resonance, $\tau_{max} = \tau(\omega_0)$. The group delay can be experimentally calculated using an EM simulator like HFSS. For a constant bandwidth filter, R should remain constant across the tuning range. From (3.9), this is equivalent to having a constant group delay peak across the tuning range.

To summarize, for a constant bandwidth tunable filter, the following two conditions need to be satisfied:

C1) The physical coupling coefficient k_{ij} should be inversely proportional to the centre frequency f_0 with a proportional constant of $[\mathbf{M}]_{ij}BW$.

C2) The group delay peak of the input/output reflection coefficient should remain constant across the tuning range.

The design principles C1 and C2 can be utilized to design constant bandwidth tunable filters in any microwave filter structure. In this study, our focus would be on combline cavity filters. In this filter structure, a resonator is realized by a metallic post inside a metallic enclosure with conducting walls. To change the resonant frequency of the resonator, a tuning disk with an adjustable position is placed above the post. The coupling between

two resonators is realized using an iris, and input/output coupling is achieved using a probe. Therefore, the design of a tunable constant bandwidth combline cavity filter involves the following four steps:

1) Tunable resonator design: The following design considerations should be addressed in designing a tunable cavity combline resonator:
   - tuning frequency range
   - quality factor
   - smooth variation of resonant frequency with respect to gap variations for fine tuning
   - minimum gap requirement to satisfy the required power handling capability
2) Inter-resonator coupling design: This involves the design of iris geometry and position such that the desired coupling value is achieved and maintained constant across the tuning range (for different gap values).
3) Input/Output coupling design: This involves the design of probe geometry and position such that the desired input/output normalized impedance value is achieved and maintained constant across the tuning range (for different gap values). The loading effect of the probe can potentially change the tuning range of the resonator, and a change in the design of the resonator might be required.
4) Design optimization

In the following, we elaborate on the above four steps.

3.2.2 Tunable Resonator Design

Combline cavity resonators could have different geometries. In Fig. 3.2, two of the most common geometries, namely cubical and cylindrical cavity resonators, are depicted along

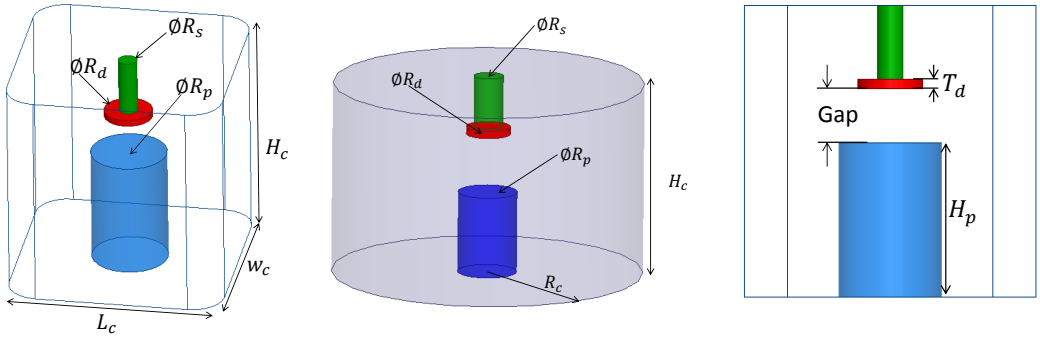

(a) Cubical cavity (b) Cylindrical cavity (c) Two dimensional view

Figure 3.2: Combline tunable resonator with tuning disk

with their two-dimensional view. The tuning element consists of a disk and a screw which grounds the disk through the cavity lid [7]. The resonant frequency of the resonator is tuned by adjusting the gap between the tuning disk and the metallic post (Gap in Fig. 3.2c). Design parameters include (see Fig. 3.2)

- cavity size: (L_c, W_c, H_c) in case of cubical cavity and (H_c, R_c) in case of cylindrical cavity
- metallic post size: (H_p, R_p)
- tuning element size: (R_d, T_d, R_s)

For any set of design parameters, one can use an EM simulator with eigen-mode calculation capability such as HFSS to obtain the resonant frequency of the resonator as well as the unloaded quality factor. The design parameters are being changed until the desired tuning range, unloaded quality factor, and other requirements are achieved.

3.2.3 Inter-resonator Coupling Design

Coupling between different resonators can be inductive or capacitive. In combline cavity filters, inductive coupling is usually realized by using an iris whereas capacitive coupling is normally realized by using a probe. In order to realize a specific inter-resonator coupling value, the geometry of the iris/probe should be designed properly.

In constant bandwidth tunable combline cavity filters, the centre frequency is tuned by adjusting the gap size between the tuning disk and the metallic post. Changing the gap size generally changes the electric and magnetic field distribution inside the cavity and consequently the inter-resonator coupling values are changed. Therefore, it seems that in order to realize a constant inter-resonator coupling in a tunable cavity filter, we must have an adjustable iris/probe configuration. However, it was shown in [1] that one can achieve almost-constant *inductive* inter-resonator coupling merely by using a horizontal iris with carefully chosen location and without any adjusting mechanism. The core observation of [1] is that the desired normalized coupling value not only depends on the iris dimensions but

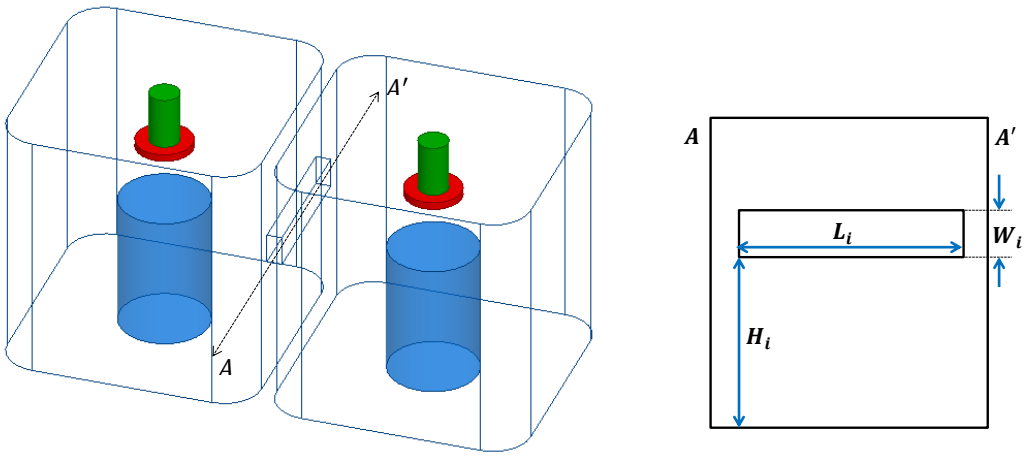

(a) Coupled resonator (b) Cross section view

Figure 3.3: Schematic diagram of two coupled resonators using horizontal iris.

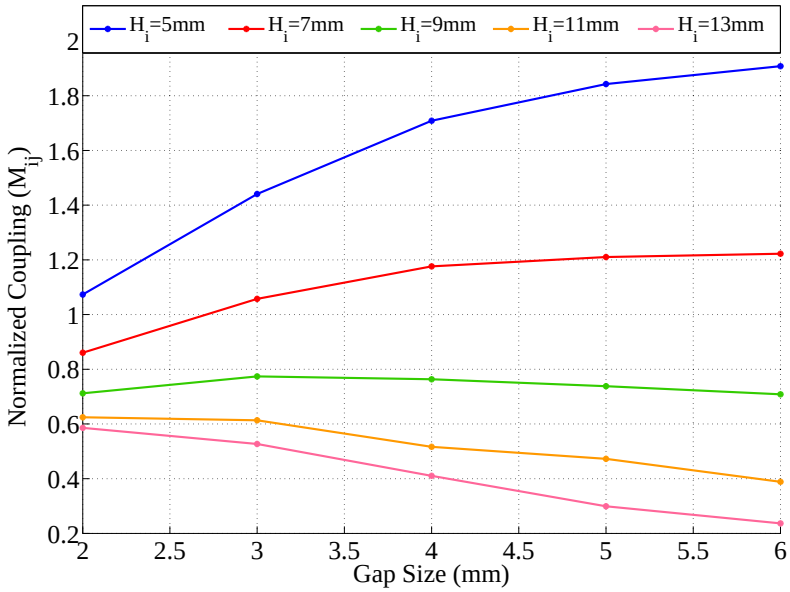

Figure 3.4: Normalized coupling variation vs. gap in a horizontal iris for different iris heights.

also on iris position. Therefore, the normalized coupling value (M_{ij}) can maintain constant by adjusting the vertical position of the horizontal iris. The structure of the two coupled resonators and the schematic diagram of the horizontal iris are depicted in Fig. 3.3. The coupling value between two resonators depends on three parameters, namely the iris height (H_i), the iris width (W_i), and the iris length (L_i). Fig. 3.4 shows the variation of simulated inter-resonator coupling for $L_i = 16.61$ mm, $W_i = 2$ mm, and different height values for the horizontal iris as the centre frequency is tuned by adjusting the gap. One can observe that for a height of $H_i = 9$ mm, the normalized coupling value remains almost constant at approximately 0.75 independent of the gap size. In this case, the resonant frequency tuning range is from 5 GHz to 6.1 GHz while the gap size is changing from 2 mm to 6 mm. Note that the achieved constant coupling value dictated by all three parameters. Hence, one can use the iterative method described in Fig. 3.5 to attain the desired constant coupling value.

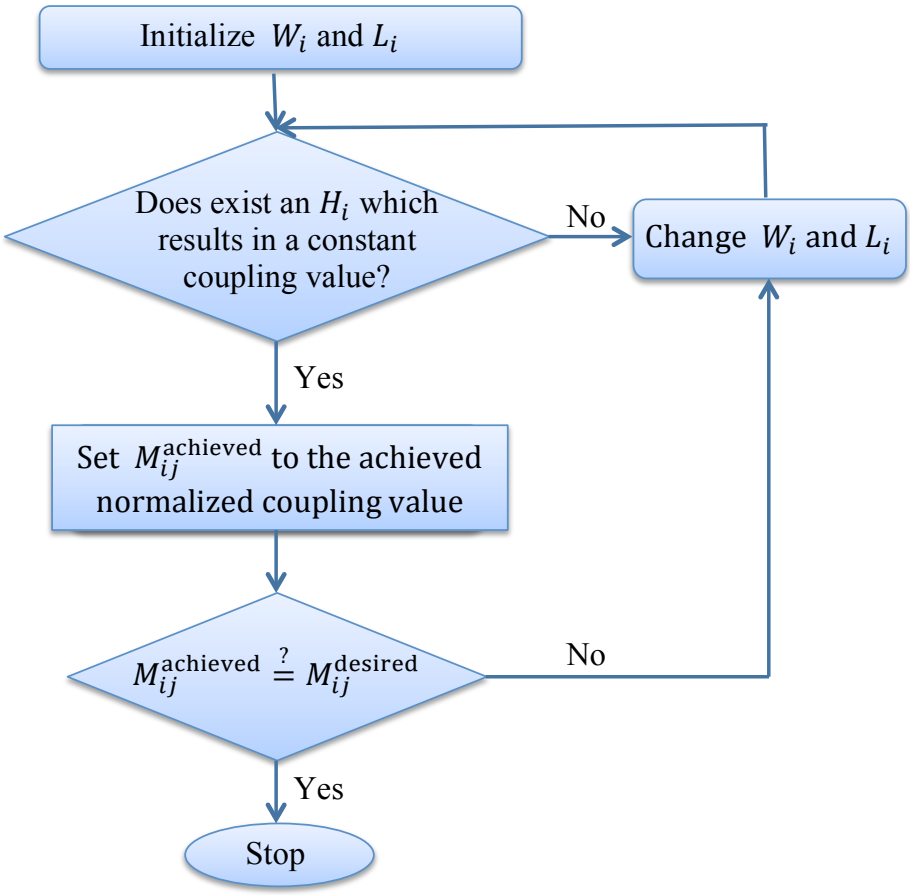

Figure 3.5: An iterative procedure to optimize the horizontal iris dimensions to achieve a constant normalized coupling. The same procedure can be applied to optimize the input/output probe dimensions.

Horizontal irises could not provide the high coupling values required in a large bandwidth tunable filter. In this study, we investigate the design of constant normalized coupling using vertical irises at the centre of the cavity side wall between two adjacent resonators. The structure of two coupled resonators using a vertical iris and the cross section view of the iris are depicted in Fig. 3.6. The iris opening is denoted by L_i. The variation of nor-

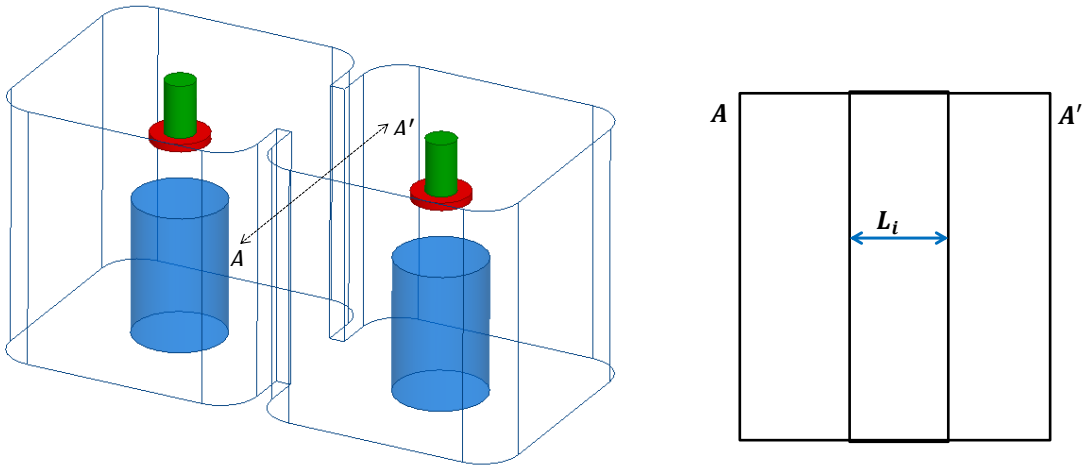

(a) Coupled resonator (b) Cross section view

Figure 3.6: Schematic diagram of two coupled resonators using a vertical iris.

malized coupling value over tuning range for different iris openings is depicted in Fig. 3.7. One can observe that different normalized coupling values can be obtained by changing the iris opening (L_i) and in each case the coupling remains approximately constant over the tuning range (no optimization is required). Therefore, vertical irises offer significant advantages over the horizontal irises in terms of design simplicity and versatility of the attainable coupling values. In this case, the resonant frequency tuning range is from 5.1 GHz to 5.9 GHz while the gap size is changing from 2.5 mm to 6 mm. In the following section, we use semi-vertical irises to design a constant bandwidth 7-pole tunable filter in the X band.

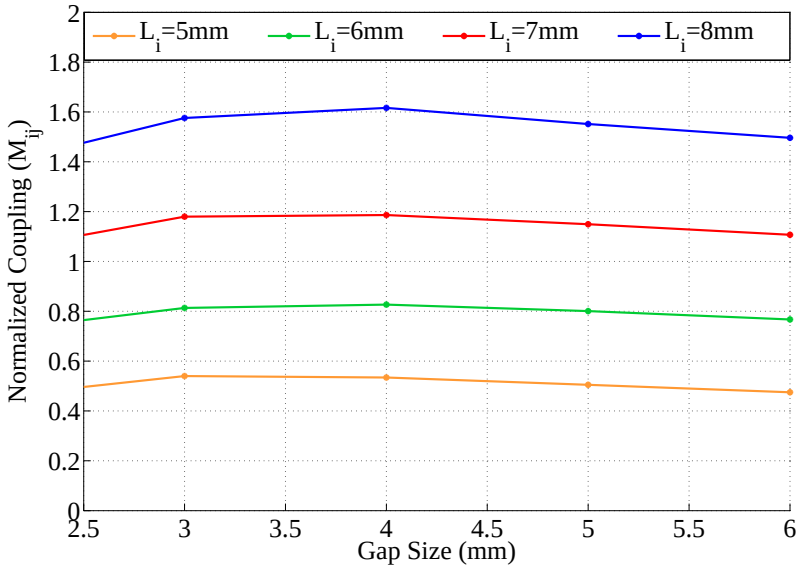

Figure 3.7: Normalized coupling variation vs. gap in a vertical iris for different iris openings.

3.2.4 Input/Output Coupling Design

To design a constant bandwidth tunable filter, the normalized impedance (R) and accordingly the group delay peak should remain constant across the tuning range. It has been shown in [1] that a constant group delay peak can be achieved if a long input/output probe is used to realize the input/output coupling. The EM model of the first resonator loaded with the input probe and its cross section view are depicted in Fig. 3.8. Note that the second resonator is detuned by removing the metallic post. The value of the normalized input/output coupling depends on three parameters namely the probe length (L_{pr}), the probe height (H_{pr}), and the probe distance to the cavity side wall (Y_{pr}). Fig. 3.9 shows the variation of simulated reflection coefficient group delay peak for $Y_{pr} = 4$ mm, $W_{pr} = 2.34$ mm, and different length values for the probe as the centre frequency is tuned. As one can see, for $L_{pr} = 15.7$ mm, the group delay peak value decreases as the resonant frequency increases from 4.9 GHz to 6.1 GHz. For $L_{pr} = 16.7$ mm, on the other hand,

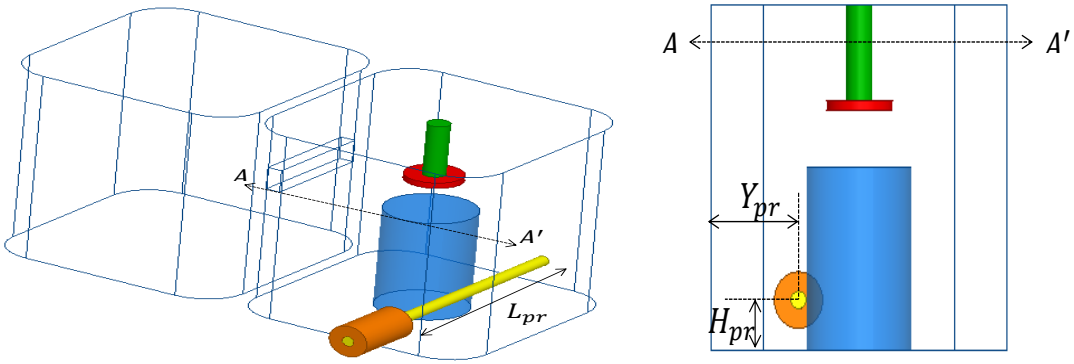

(a) First resonator loaded with input probe

(b) Cross section view

Figure 3.8: Schematic diagram of the input/output resonator loaded with a long probe

the group delay peak value increases as the resonant frequency increases. So, there is an optimum length for the probe which will result in a constant group delay peak value and consequently a constant normalized input/output impedance over the tuning range. This optimum length is approximately $L_{pr} = 16.2$ mm in Fig. 3.9 with the corresponding normalized impedance of approximately 1.25. Note that the achieved normalized impedance depends on all three parameters (Y_{pr}, H_{pr}, L_{pr}) and therefore one can use an iterative method similar to what explained in Fig. 3.5 to attain a desired normalized impedance. This method will be used in this and following chapters to design 5-pole, 6-pole, and 7-pole tunable filters with a constant absolute bandwidth.

3.2.5 Design Optimization

The EM-based synthesis technique [3] is used to design the filter. In this method, the unwanted coupling between the different resonators is neglected, and therefore the actual response of the filter does not match the ideal response. In order to decrease the mismatch between these two responses, one needs to optimize the filter. To this end, we need to adjust the design parameters such as iris and probe dimensions in a systematic way such that its

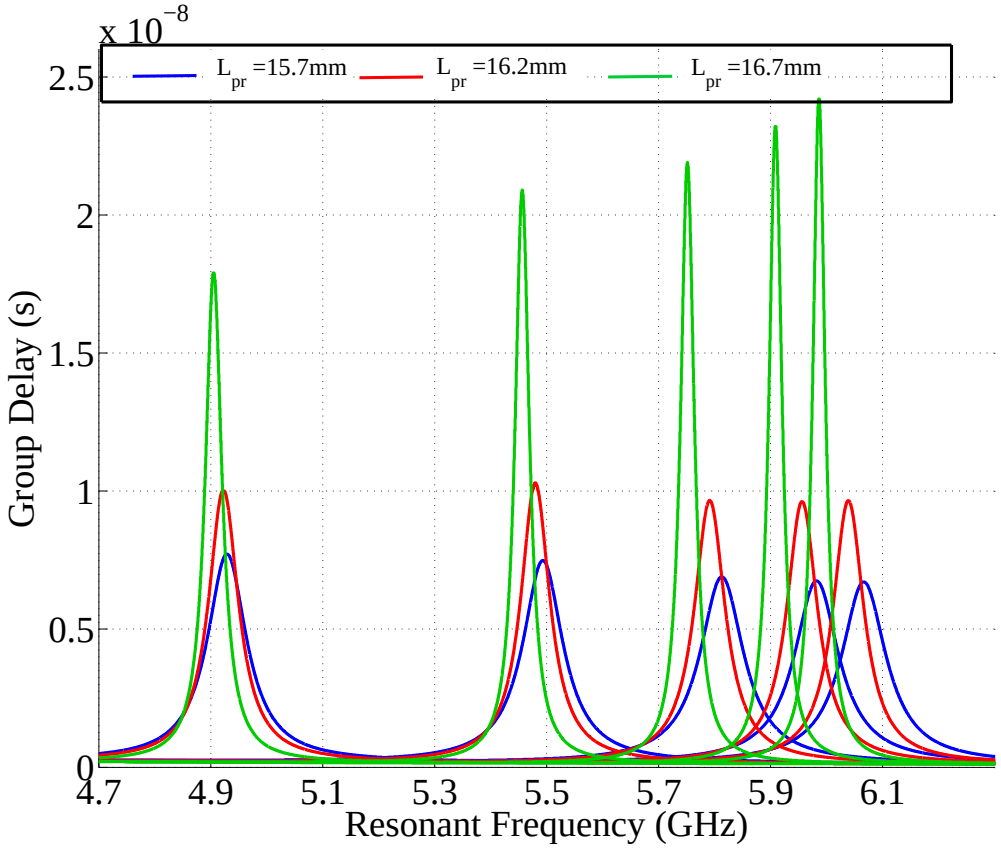

Figure 3.9: Group delay peak variation vs. resonant frequency for different L_{pr} values.

corresponding filter response in HFSS meet the design specification. We use the aggressive space mapping (ASM) method to optimize the filter [36,37]. In the ASP method, there are two sets of design parameters: fine model design parameters (x_f) and coarse model design parameters (x_c). The fine model parameters are obtained by an EM simulator like HFSS whereas the coarse model parameters are obtained by a circuit simulator like ADS. The ultimate goal is to iteratively adjust the fine model design parameters by adjusting the coarse model design parameters and then establishing a mapping between parameters of the two models. Let X_c^* represent the optimal coarse model parameters which can be easily obtained using low-pass prototype model. In other words $R_c(x_c^*)$ approximately gives the

desired response in the coarse model. Also, let $R_c(x_c^{(k)})$ and $R_f(x_f^{(k)})$ respectively denote the response of the coarse model and fine model at iteration k of the algorithm. The ASM algorithm can be summarized as follows [3]:

- **Step 1.** Initialize $k = 1$, and set $x_f^{(1)}$ as the initial designed parameters using HFSS. Also, let $B(1) = \mathbb{I}$.
- **Step 2.** Find $R_f(x_f^{(1)})$.
- **Step 3.** Extract $x_c^{(1)}$ such that $R_c(x_c^{(1)}) \approx R_f(x_f^{(1)})$.
- **Step 4.** Evaluate $f^{(1)} = x_c^{(1)} - x_c^*$. Stop if $\|f^{(1)}\| \leq \eta$.
- **Step 5.** Find $h^{(k)} = -[B^{(k)}]^{-1} f^{(k)}$.
- **Step 6.** Set $x_f^{(k+1)} = x_f^{(k)} + h^{(k)}$.
- **Step 7.** Evaluate $R_f(x_f^{(k+1)})$.
- **Step 8.** Extract $x_c^{(k+1)}$ such that $R_c(x_c^{(k+1)}) \approx R_f(x_f^{(k+1)})$
- **Step 9.** Evaluate $f^{(k+1)} = x_c^{(k+1)} - x_c^*$. Stop if $\|f^{(k+1)}\| \leq \eta$.
- **Step 10.** Update $B^{(k+1)} = B^{(k)} + \frac{f^{(k+1)}[h^{(k)}]^T}{[h^{(k)}]^T h^{(k)}}$
- **Step 11.** Set $k = k + 1$ and go to step 5.

The coupling matrix elements will form the vector x_c. This is accomplished by simulating the coupling matrix using the J-admittance inverter model in ADS circuit simulator as illustrated in Fig. 3.10 for a 5-pole filter. In other words, for any given S_{11}, we can find the corresponding elements of the J-admittance inverter model and consequently the coupling matrix elements. We also select x_f as the physical filter parameters (iris, probe, and gap size) that need to be optimized. Since x_c and x_f are not representing the same

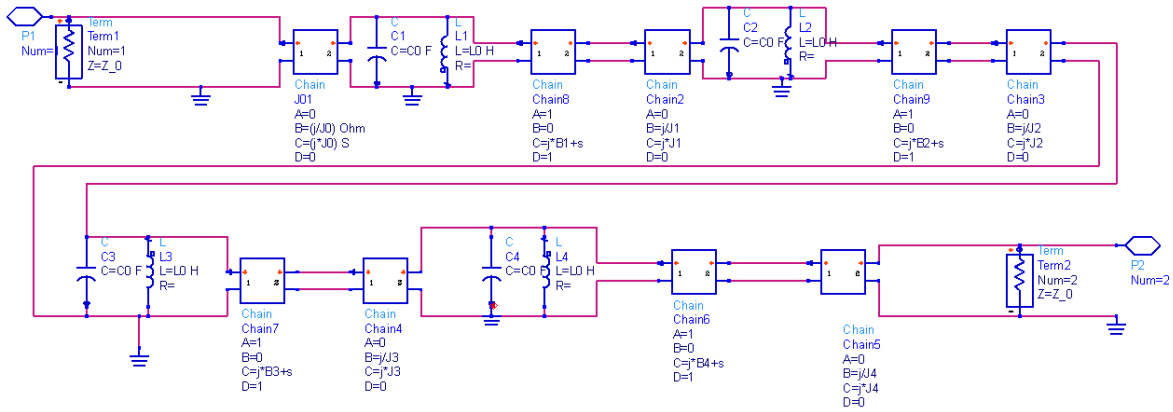

Figure 3.10: Schematic of the coarse model in ADS simulator

parameters, one needs to take care of this in updating x_f in Step 6 of the algorithm. This can be accomplished by modifying the Step 6 of the algorithm as follows:

$$x_f^{(k+1)} = x_f^{(k)} + Q(h^{(k)}), \tag{3.10}$$

where $Q(\cdot)$ is a function which maps $h^{(k)}$ from the coarse model domain (coupling matrix) to $Q(h^{(k)})$ in the fine model domain (physical parameters). In other words, $Q(\cdot)$ translates a change in coupling matrix elements to the corresponding change in physical parameters of the filter. Assuming a linear model, a change ΔL_{ij} in iris window length is translated into a proportional change in inter-resonator coupling elements

$$\Delta M_{ij} = \alpha \times \Delta L_{ij}, \tag{3.11}$$

where the proportional constant α can be obtained using HFSS simulation of the two-coupled resonator structure illustrated in Fig. 3.3. By changing L_{ij} and recording the corresponding values of f_e and f_m in HFSS simulation, it turns out $\alpha = 0.18703$ as depicted in Fig. 3.11.

Similarly, a change ΔH_{pr} in probe height is translated into a proportional change in normalized input/output impedance

$$\Delta R = \gamma \times \Delta H_{pr}, \tag{3.12}$$

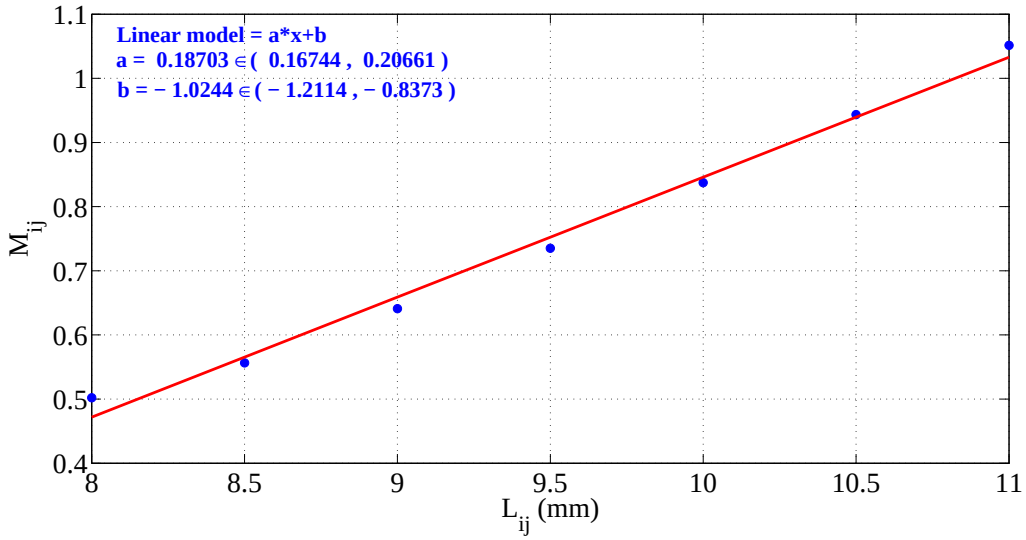

Figure 3.11: HFSS simulation of inter-resonator coupling vs. iris window length

where the proportional constant γ can be obtained by changing H_{pr} and recording the corresponding values of $\tau(\omega_0)$ in HFSS simulation. As illustrated in Fig. 3.12, $\gamma = 0.63145$. Finally, a change ΔG_i in gap size is translated into a proportional change in the corresponding self-coupling element

$$\Delta M_{ii} = \beta \times \Delta G_i, \tag{3.13}$$

with the proportional constant β given by

$$\beta = -\frac{2}{BW}\frac{\Delta\omega_0}{\Delta G}, \tag{3.14}$$

where $\Delta\omega_0$ is the change in the resonant frequency of a single resonator resulting from a change ΔG in its gap size. In order to obtain β for the first and last resonator, the loading effect of the probe should be considered as illustrated in the EM model of Fig. 3.13. As one can see, the adjacent cavities are detuned by removing their corresponding posts. Also, the impact of irises in calculation of resonant frequency of other resonators is considered in this model. From the HFSS simulation results in Fig. 3.14, $\beta = -20.61$. The same method can be used to calculate β for other resonators. A couple of comments are in order:

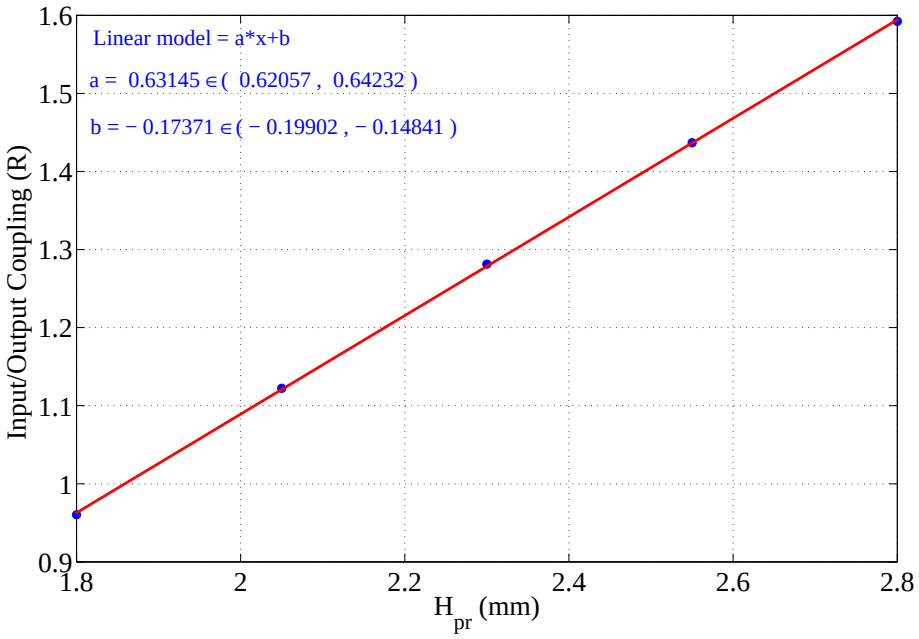

Figure 3.12: HFSS simulation of normalized input/output impedance vs. probe length.

- The symmetrical structure of the filter impose some restrictions on the coupling matrix elements. In specific, $W_{12} = W_{n-1,n}$, leads to $M_{12} = M_{n-1,n}$. Similarly, $G_1 = G_n$, results in $M_{11} = M_{nn}$. Also, since the input and output ports are designed to have the same length, we need to have $R_S = R_L$. These restrictions need to be considered when we are looking for a coupling matrix corresponds to a given S_{11} response in ADS circuit simulator.

- Since one can find different coupling matrices that give the exact same S_{11} response, the elements of the coupling matrix should have values close to ideal coupling matrix values. Otherwise, the space mapping approach does not converge.

- It is experimentally observed that the ASM method will not converge if HFSS simulation is not fully converged. In specific, when the gap size is small compare to the other parts of structure, a mesh seeding might be required to achieve the convergence.

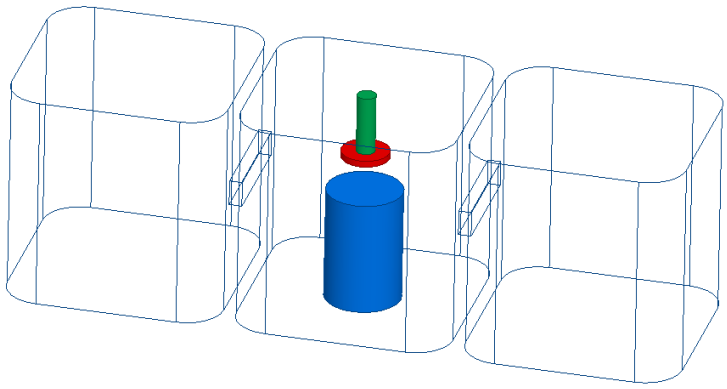

Figure 3.13: EM model for calculating resonant frequency, including the effect of irises.

By optimizing design parameters including probe, iris, and gap dimensions, the filter is tuned to meet the required specification at the middle of the frequency range. In a constant bandwidth design, all input/output coupling, cross coupling, and mainline coupling should be independent of the resonant frequencies of resonators. Therefore, after the filter dimensions are optimized for the middle of the tuning range, the probe and iris dimensions are held fixed, and gap sizes are adjusted to tune the filter over the tuning range. In this study, a combination of Ness and ASM methods is used for filter tuning [38, 39]. The fine and coarse parameters are respectively the gap sizes and self coupling values with the corresponding mapping in (3.13). The tuning process can be described as follows:

- **Step 1.** Detune all resonators except for the first and last resonators, namely 1 and n. The gap size of these two resonators is then adjusted using the ASM method such that the reflection coefficient group delay responses in EM simulation match those in the circuit model simulation.

- **Step 2.** Detune all resonators except for the first two resonators, namely 1 and 2, and the last two resonators, namely $n-1$ and n. The gap size of resonators 2 and $n-1$ is then adjusted using the ASM method such that the reflection coefficient group delay responses in EM simulation match those in the circuit model simulation.

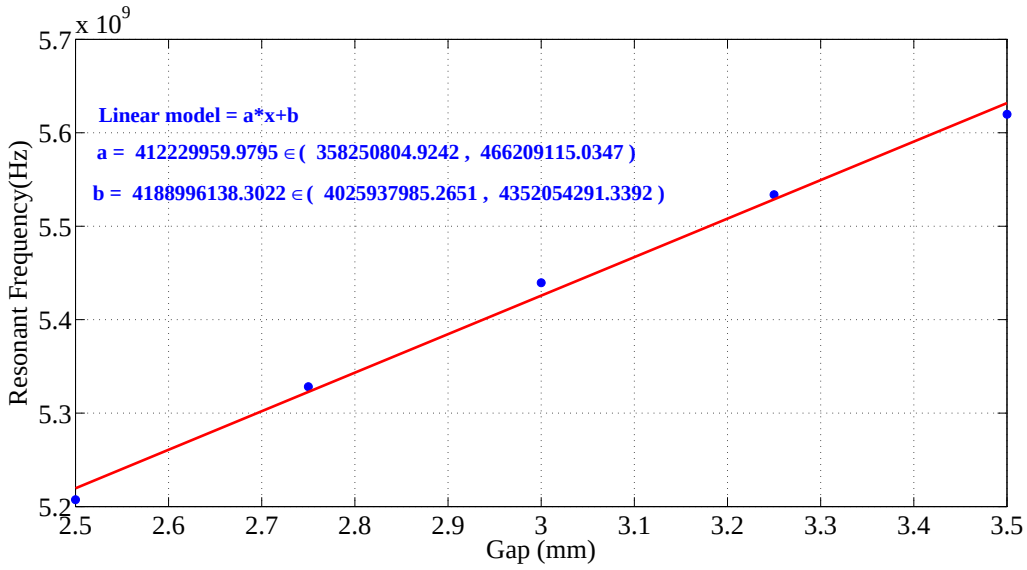

Figure 3.14: Self-resonator coupling versus the Gap calculated from HFSS simulation results.

- **Step $\frac{n}{2}$ for n even.** Adjust the gap size of the last two remaining resonators, namely $\frac{n}{2}$ and $\frac{n}{2}+1$, to optimize the final response.
- **Step $\frac{n-1}{2}$ for n odd.** Adjust the gap sizes of the last two symmetric resonators, namely $\frac{n-1}{2}$ and $\frac{n-1}{2}+2$, while the middle resonator, namely $\frac{n-1}{2}+1$, is detuned.
- **Step $\frac{n+1}{2}$ for n odd.** Adjust the gap size of the last remaining resonator, namely $\frac{n-1}{2}+1$, to optimize the final filter response.

A couple of comments are in order:

- In symmetrical structures, all symmetrical parameters have the same value. So, only $\frac{n}{2}$ resonators need to be tuned to optimize the filter response.
- For lab tuning of symmetrical tunable filters, the first and last resonators are first tuned such that the group delay response at the input and output ports match each

other while other resonators are detuned (grounded). Next, the first and last two resonators are tuned such that the group delay response at the input and output ports match each other while other resonators are detuned (grounded) and so on. This method significantly reduces the tuning time and effort and help to achieve a better measured response.

3.3 5-pole Filter Design

In this section, a C-band in-line 5-pole tunable Chebyshev filter with the middle frequency point of 5.5 GHz, a constant absolute bandwidth of 42 MHz, and a return loss of 25 dB is synthesized and tested. The desired tuning range is from 4.9 GHz to 6 GHz. The coupling-routing diagram of the filter is depicted in Fig. 3.24.

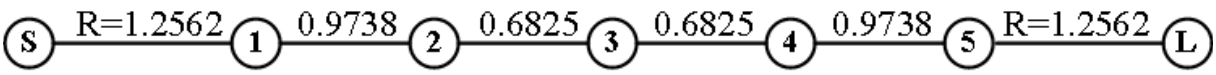

Figure 3.15: Coupling-routing diagram of the 5-pole filter.

3.3.1 Resonator Design

A cubical tunable resonator is selected to realize frequency tuning (see Fig. 3.2a). The resonator is tuned by adjusting the gap size between the tuning screw and the metallic post. The EM simulation results for the tuning range and unloaded Q values of the resonator are presented in 3.16. As the gap size changes from 2 mm to 6 mm, the centre frequency is tuned from 4.9 GHz to 6 GHz, while the unloaded Q varies from 3500 to 4300. The resonator housing is made of aluminium. The geometrical dimensions of the filter are listed in Table 3.1

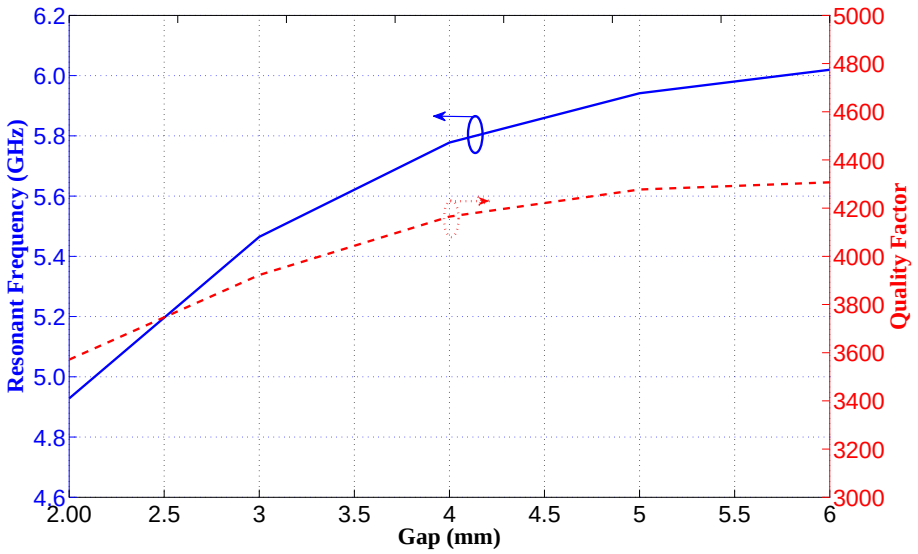

Figure 3.16: The resonant frequency and unloaded Q versus gap size: HFSS simulation result

Table 3.1: Cubical resonator's dimensions.

	Cavity			Post		Tuning element		
Parameters	L_c	W_c	H_c	H_p	ϕR_p	ϕR_d	T_d	ϕR_s
Size(mm)	17	17	17	9	3	1.9	0.5	0.75

3.3.2 Inter-resonator Coupling Design

A horizontal iris is used to realized the coupling between adjacent resonators (see Fig. 3.3). The desired couplings to be realized are $M_{12} = M_{45} = 0.9835$ and $M_{23} = M_{34} = 0.6825$. Using the iterative method described in the previous section, the optimized iris sizes to achieve constant coupling over the tuning range are listed in Table 3.2 for the desired coupling values. The HFSS simulation results of adjacent normalized coupling values over the tuning range are depicted in Fig. 3.17.

Table 3.2: Optimized iris sizes to attain constant coupling for different coupling values.

	Iris (M_{12} and M_{45})			Iris (M_{23} and M_{34})		
Parameters	L_i	W_i	H_i	L_i	W_i	H_i
Size(mm)	16.61	2	9.3	9.83	2	8.92

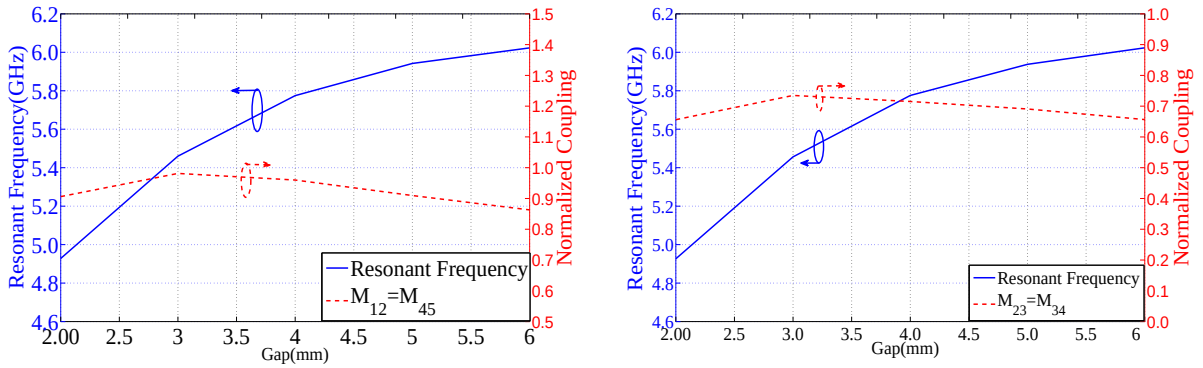

(a) $M_{12} = M_{45} = 0.9835$ (b) $M_{23} = M_{34} = 0.6825$

Figure 3.17: EM simulation results of adjacent normalized coupling over the tuning range

3.3.3 Input/Output Coupling Design

A long probe is used to realize the input/output coupling (see Fig. 3.8). Using the iterative method described in Fig. 3.5, the iris dimensions are optimized to achieve a constant normalized input/output coupling in HFSS EM simulation. The optimized probe dimensions are summarized in Table 3.3. The group delay of input reflection coefficient of the first resonator is illustrated in Fig. 3.18. Note that the group delay peak value remains almost constant over the tuning range.

Table 3.3: Probe dimensions for constant input/output coupling.

	Probe		
Parameters	L_{pr}	Y_{pr}	H_{pr}
Size(mm)	16.21	4	2.34

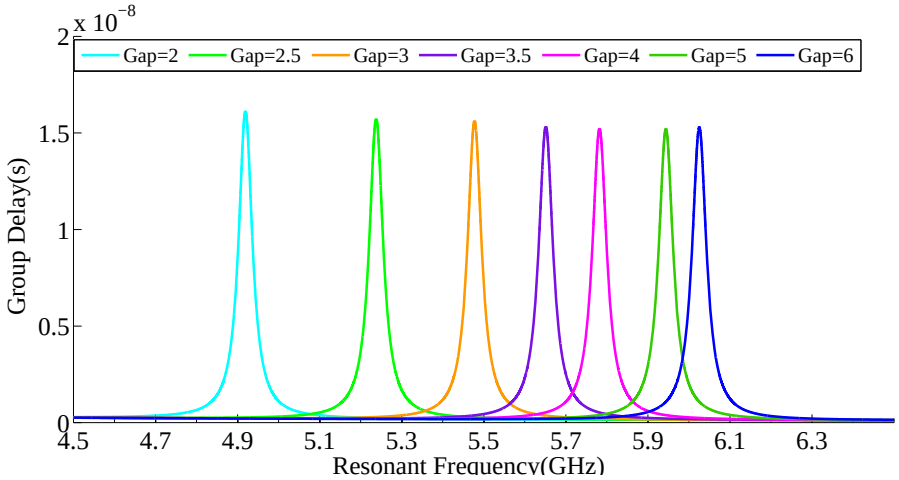

Figure 3.18: EM simulation result of group delay over the tuning range.

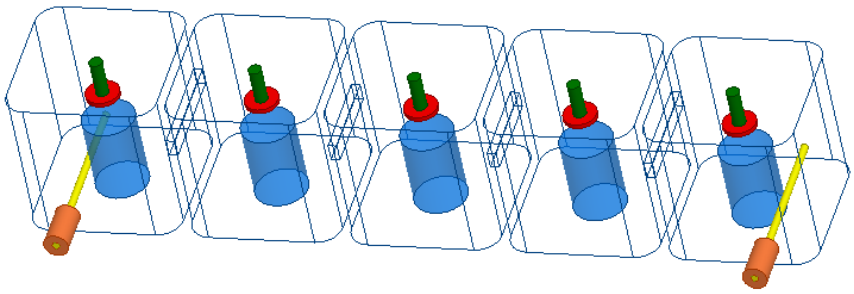

Figure 3.19: EM model of 5-pole tunable filter.

3.3.4 EM Simulation Results

The EM model of the complete filter design is illustrated in Fig. 3.19. Using the optimization technique described in the previous section, the filter is tuned over the desired frequency range by adjusting the gap sizes. The EM simulation response of the filter over the tuning range is depicted in Fig. 3.20. As one can see, the filter achieves a stable frequency response over the frequency tuning range of 4.89 GHz to 6 GHz. The bandwidth variation over the tuning range is less than $\pm 5.3\%$.

3.3.5 Measurement Results

The prototype designed filter is fabricated with aluminium. The centre frequency of the filter can be tuned either manually using tuning screws or automatically using piezoelectric motors as illustrated in Fig. 3.21. For automatic tuning, the tuning element of each resonator is connected to a tiny ultrasonic linear actuator (TULA) [40, 41]. This actuator is controlled by changing the frequency and duty ratio of its driving voltage. A detailed description of TULA motor control can be found in Appendix A.

The measured tuning transmission and return loss responses of the filter with piezoelectric motors are depicted in Fig. 3.22. As it can be seen from this figure, the measured

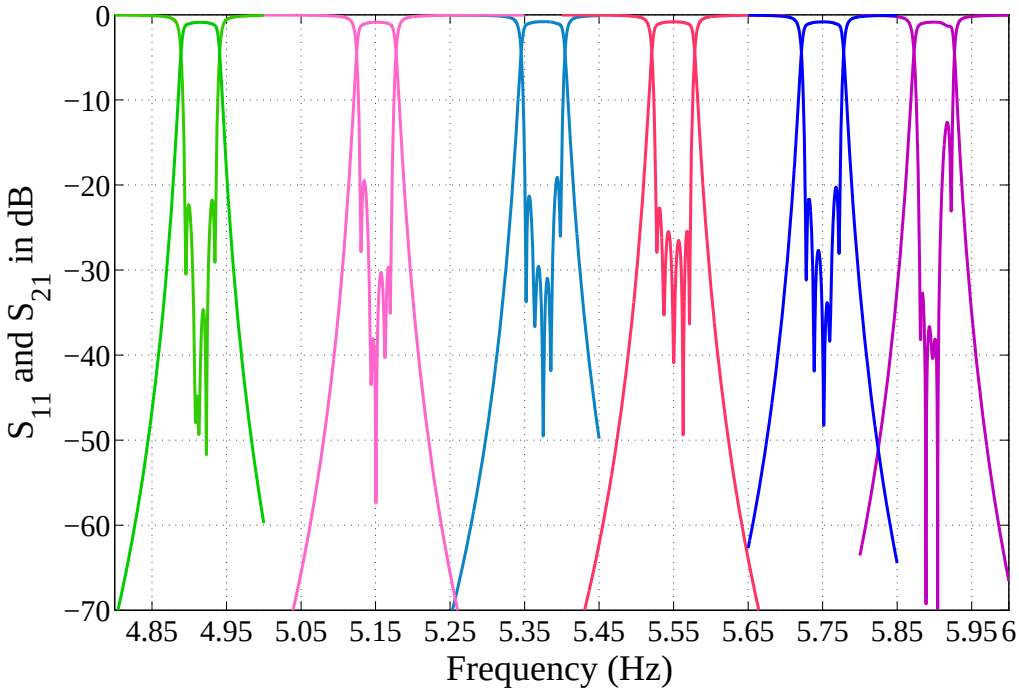

Figure 3.20: EM simulated tuning performance of the 5-pole filter

response is in close agreement with EM simulation results. The insertion loss of the filter can be improved by using silver-plated aluminium housing. The filter response maintains an excellent stable return loss response (better than 18 dB) over more than 1 G tuning range. The measured S_{21} group delay response is shown in Fig. 3.23. As one can see, the filter has a pretty stable group delay response across the tuning range. The group delay variation inside the filter passband is less than 10 nsec.

(a) Filter with tuning screws.

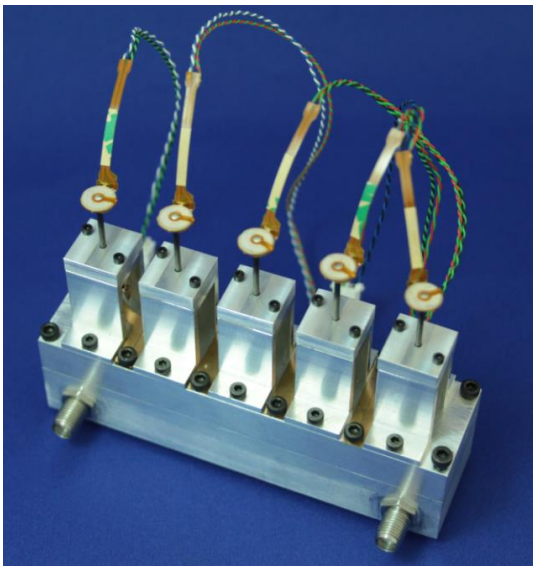

(b) Filter with piezoelectric motors: side view.

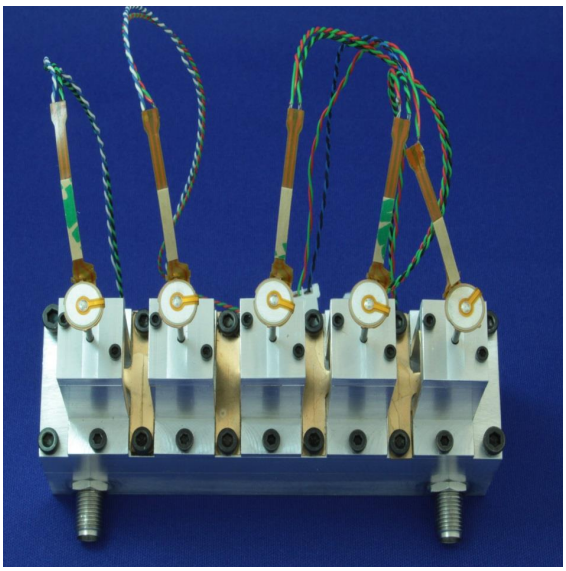

(c) Filter with piezoelectric motors: top view.

Figure 3.21: Fabricated 5-pole bandpass tunable filter.

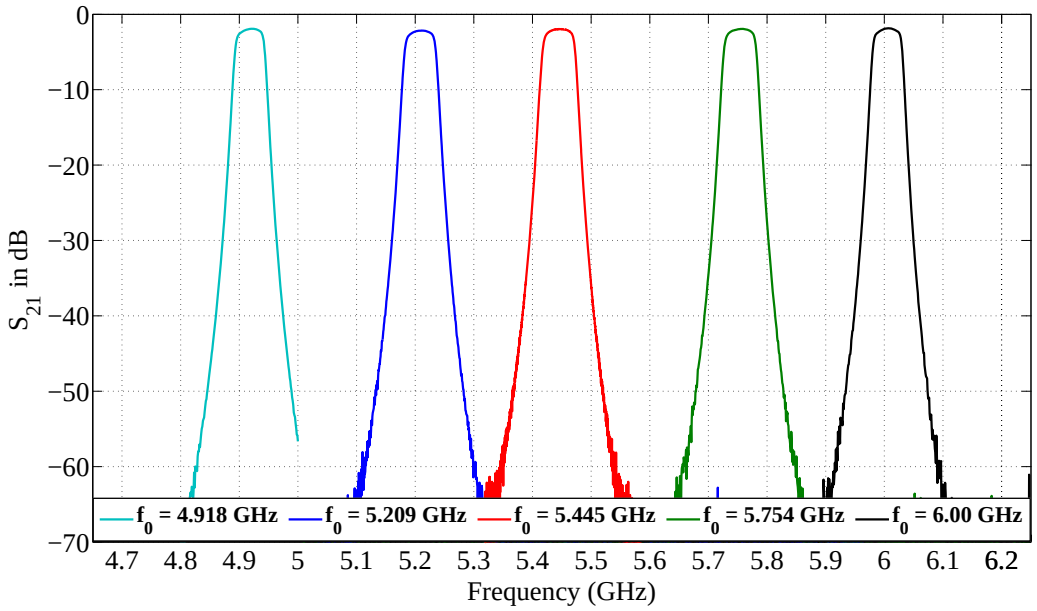

(a) Transmission Response $|S_{21}|$

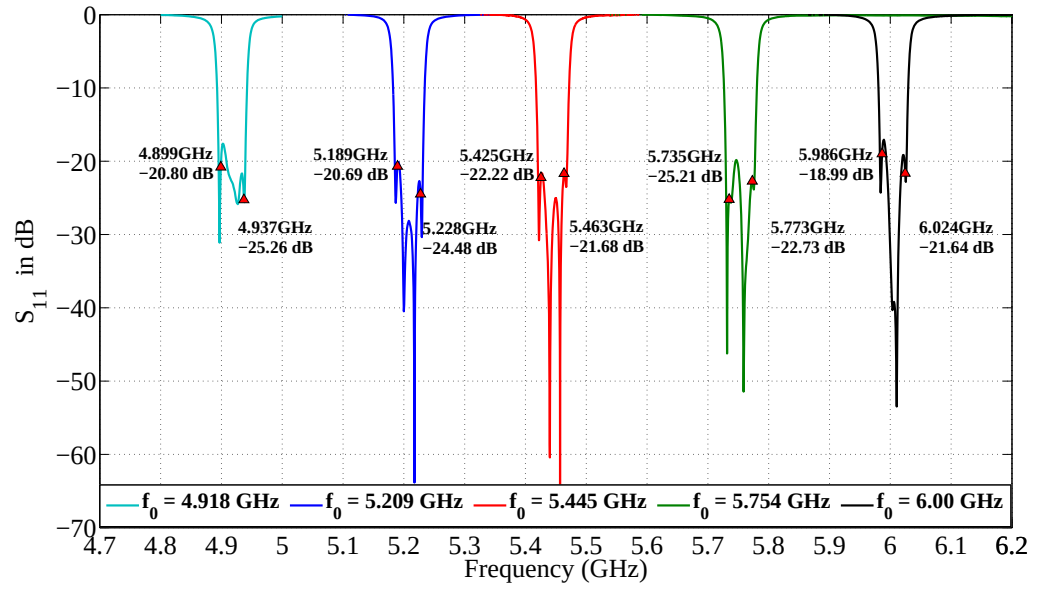

(b) Return Loss Response

Figure 3.22: Measured tuning response of the 5-pole tunable filter.

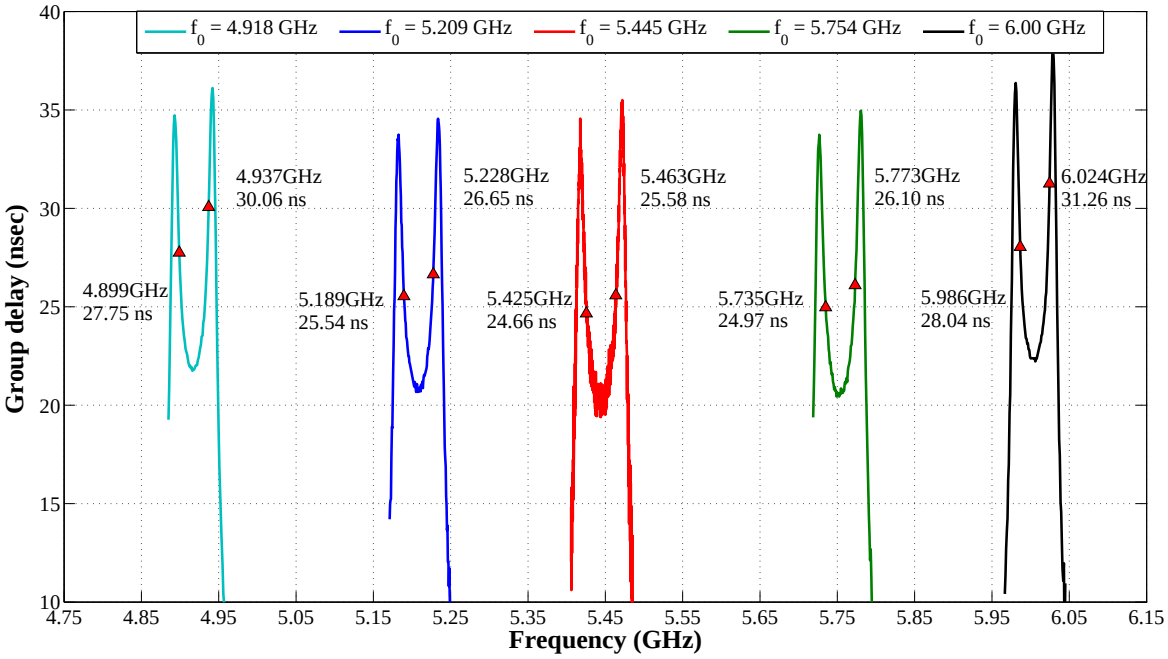

Figure 3.23: Measured group delay response of the 5-pole filter.

3.4 7-pole Filter Design

In this section, an X-band in-line 7-pole tunable Chebyshev filter with middle frequency point of 7.5 GHz, a constant absolute bandwidth of 80 MHz, and a return loss of 25 dB is synthesized and tested. The desired tuning range is from 7 GHz to 7.9 GHz. The coupling-routing diagram and coupling values of the filter are depicted in Fig. 3.24.

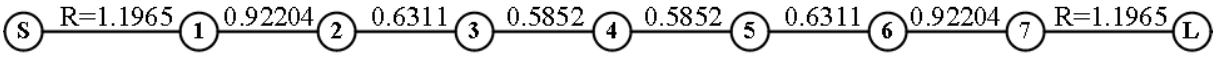

Figure 3.24: Coupling-routing diagram of the 7-pole tunable Chebyshev filter.

3.4.1 Resonator Design

A cylindrical resonator is selected to realize frequency tuning (see Fig. 3.2b). The EM simulation results for the tuning range and unloaded Q values of the resonator are presented in Fig. 3.25 for two different materials, namely copper and aluminium. The resonant frequency is tuned from 7 GHz to 8 GHz by adjusting the gap size from 3 to 6 mm. The resonator unloaded Q is above 4900 in case of copper housing and above 4000 in case of aluminium housing over the entire tuning range. The geometrical dimensions of the resonator are listed in Table 3.4.

Table 3.4: 7-pole resonator's dimensions.

	Cavity		Post		Tuning element		
Parameters	R_c	H_c	H_p	ϕR_p	ϕR_d	T_d	ϕR_s
Size(mm)	2	13	5.5	2	1.5	0.5	1

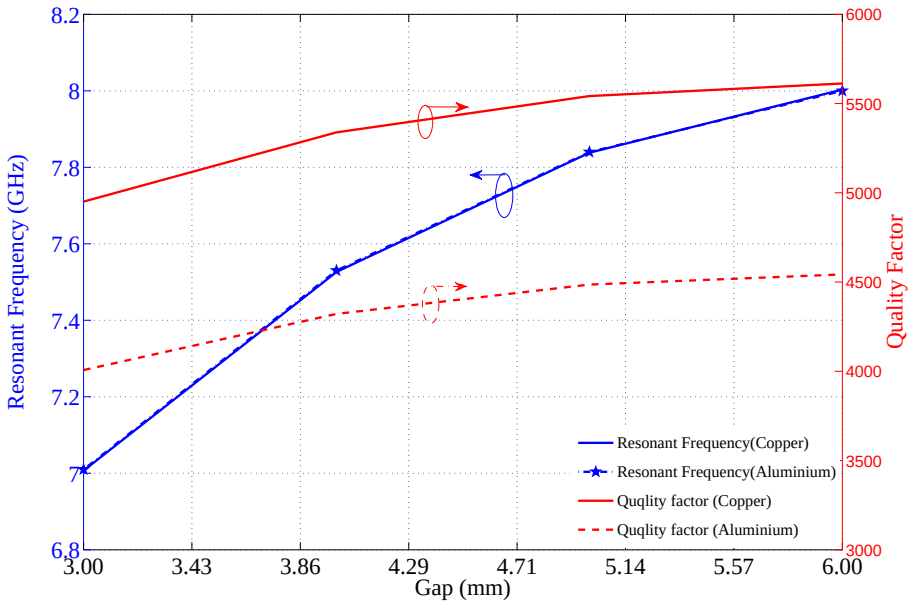

Figure 3.25: Simulation results of resonant frequency and unloaded Q vs. gap size for a cylindrical resonator made from copper or aluminium.

3.4.2 Inter-resonator Coupling Design

The normalized adjacent couplings of the 7-pole filter are realized using semi-vertical irises. The structure of two adjacent resonators coupled through a semi-vertical iris and the schematic diagram of the semi-vertical iris are depicted in Fig. 3.26. The desired normalized coupling values are $M_{12} = M_{67} = 0.92204$, $M_{23} = M_{56} = 0.6311$, and $M_{34} = M_{45} = 0.5852$. The iterative algorithm described in Fig. 3.5 is used to achieve constant normalized coupling over the tuning range. The optimized iris dimensions for different coupling values are summarized in Table 3.5.

The EM simulation results of normalized coupling values over the frequency tuning range are depicted in Fig. 3.27. As it can be seen from this figure, each individual coupling value remains approximately constant over the tuning range.

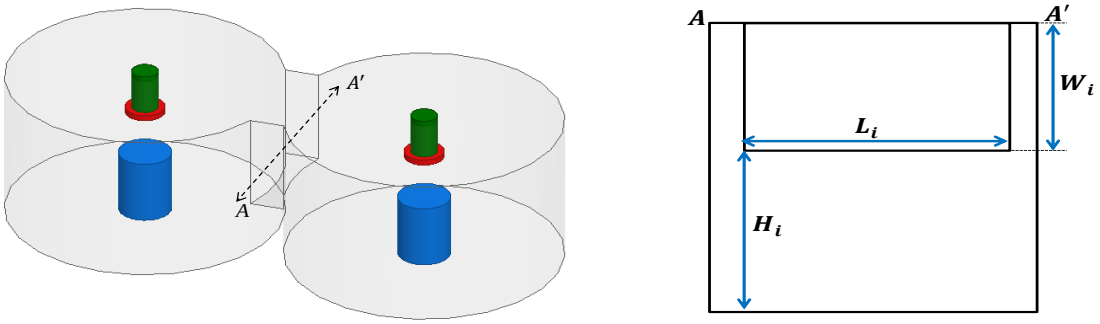

(a) Two adjacent resonators coupled by a semi-vertical iris.

(b) Cross section view of the semi-vertical iris.

Figure 3.26: Schematic diagram of two coupled resonators using a semi-vertical iris.

Table 3.5: Optimized iris dimensions to achieve constant normalized couplings in the 7-pole Chebyshev tunable filter.

	Iris (M_{12} and M_{67})			Iris (M_{23} and M_{56})			Iris (M_{34} and M_{45})		
Parameters	L_i	W_i	H_i	L_i	W_i	H_i	L_i	W_i	H_i
Size(mm)	11	5	7	8.35	7.2	4.8	8.1	7.2	4.8

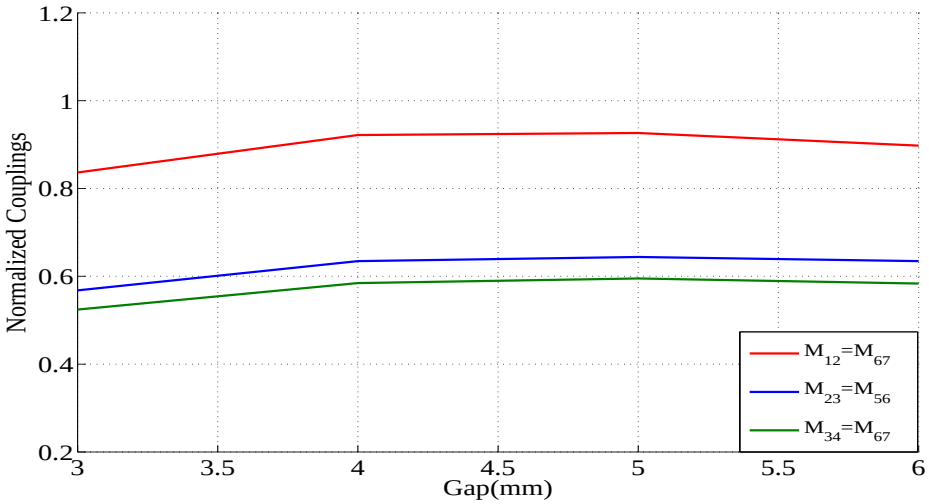

Figure 3.27: EM simulation results of adjacent normalized coupling over the tuning range.

3.4.3 Input/Output Coupling Design

A long probe is used to realized input/output coupling (see Fig. 3.8). An iterative method similar to Fig. 3.5 is used to optimize the probe dimensions for a constant normalized input/output impedance. It is observed that the loading effect of the probe shifts the tuning range of the first and last resonators toward lower frequency values. To compensate this loading effect, the resonator post height (H_p) needs to be optimized such that the desired frequency range (7 to 7.9 GHz) is achieved. The optimized post height for the first and last resonators in the presence of the probe is 5.15 mm. After this change, the probe dimensions need to be optimized again. This routine is repeated until the convergence happens. The optimized probe dimensions are listed in Table 3.6.

The EM simulation results of the reflection coefficient group delay of the first resonator are illustrated in Fig. 3.28. As one can see, the group delay peak value is approximately constant across the tuning range.

Table 3.6: Probe dimensions for constant input/output coupling.

	Probe		
Parameters	L_{pr}	Y_{pr}	H_{pr}
Size(mm)	16.89	5.84	4.18

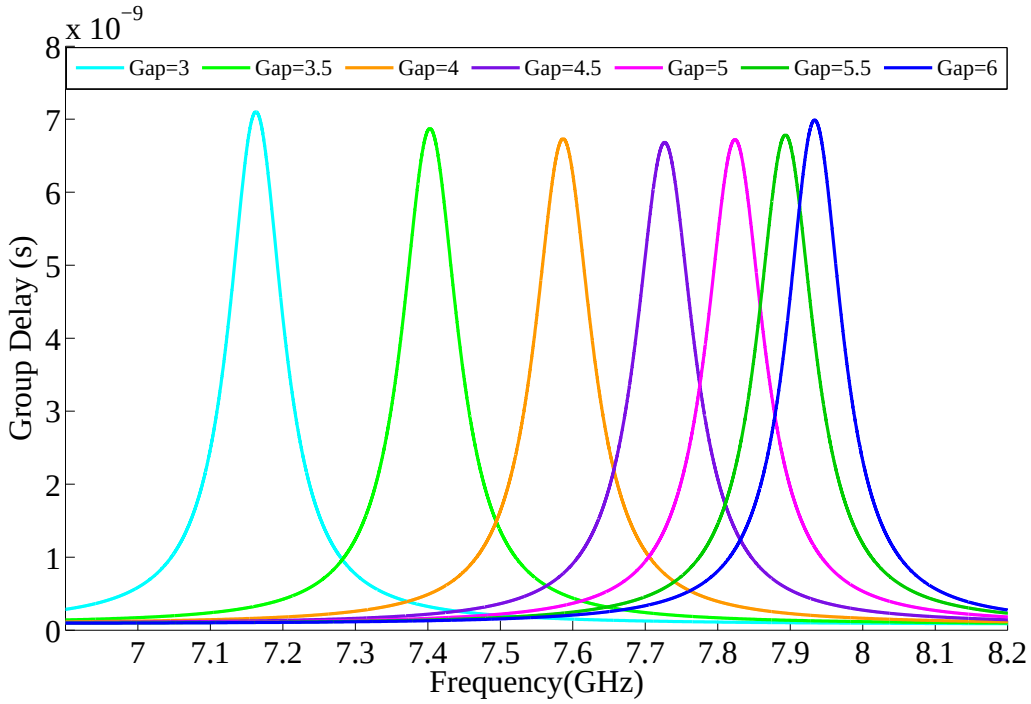

Figure 3.28: EM simulation of the reflection coefficient group delay of the first resonator over the tuning range.

3.4.4 EM Simulation and Measurement Results

The EM model of the complete design is illustrated in Fig. 3.29. The gap sizes are optimized using the space mapping method to obtain the required filter response at any point inside the tuning range. The EM simulation and ideal circuit results of the filter at $f_0 = 7.5$ GHz are depicted in Fig. 3.30. As it can be seen from this figure, there is a close

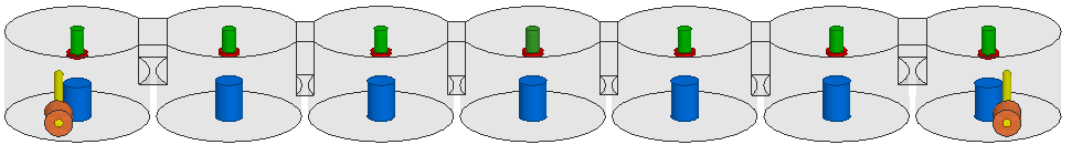

Figure 3.29: EM model of the 7-pole tunable filter with absolute constant bandwidth.

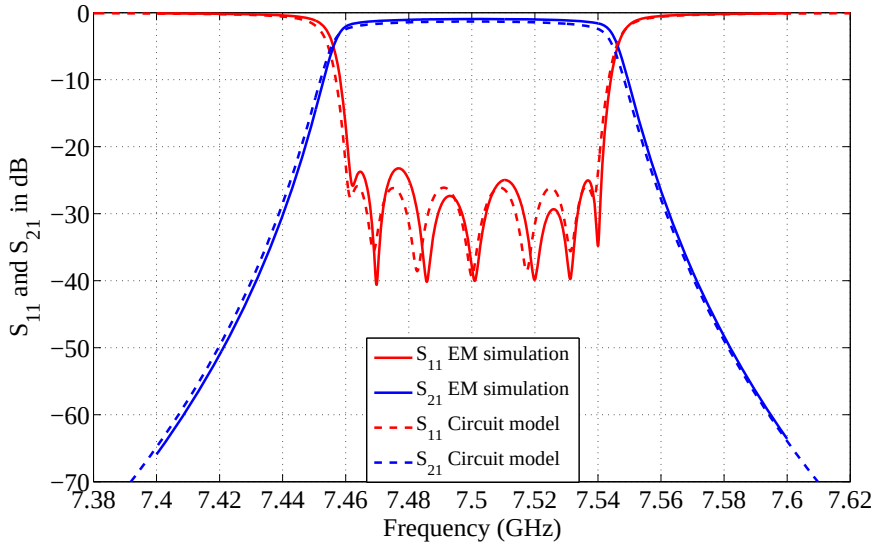

Figure 3.30: EM and ideal response of the 7-pole constant bandwidth tunable filter at the middle of the tuning range.

agreement between these two results. Note that the quality factor has been considered in the ideal circuit model.

The prototype designed filter is fabricated with aluminium. The 3D CAD drawing of the filter is depicted in Fig. 3.31a.

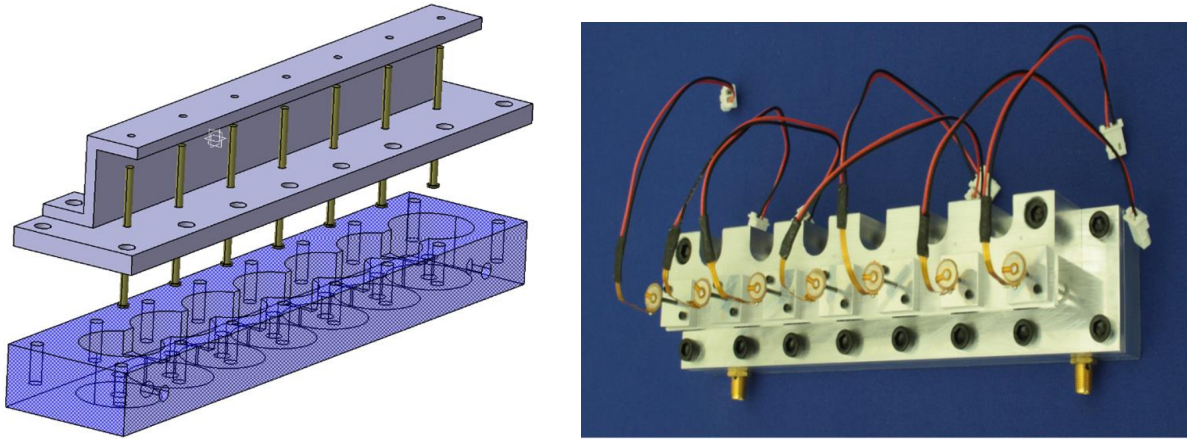

(a) The 3D CAD drawing

(b) Fabricated filter with automated piezoelectric motor tuning

Figure 3.31: Physical structure of the 7-pole filter.

The centre frequency of the filter can be tuned in an automated fashion using piezoelectric motors as depicted in Fig. 3.31b.

The measured tuning responses of the filter are depicted in Fig. 3.32. The filter exhibits a tuning range of approximately 900 MHz from 7 GHz to 7.9 GHz with an insertion loss better than 2.7 dB. The return loss is better than 14 dB across the tuning range. The bandwidth variation is from 77 MHz to 88 MHz, less than $\pm 6.7\%$ over the entire tuning range.

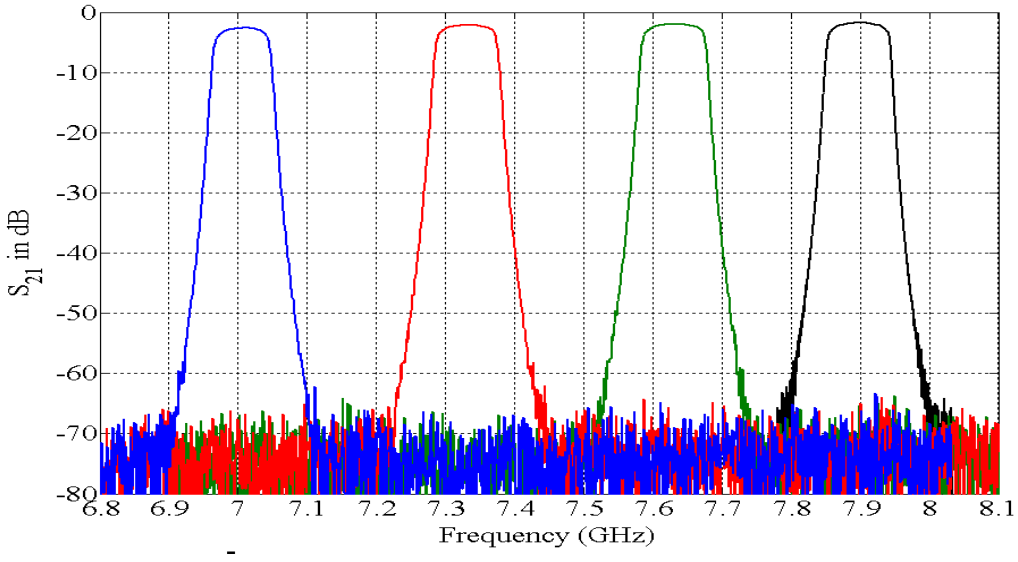

(a) Transmission Response

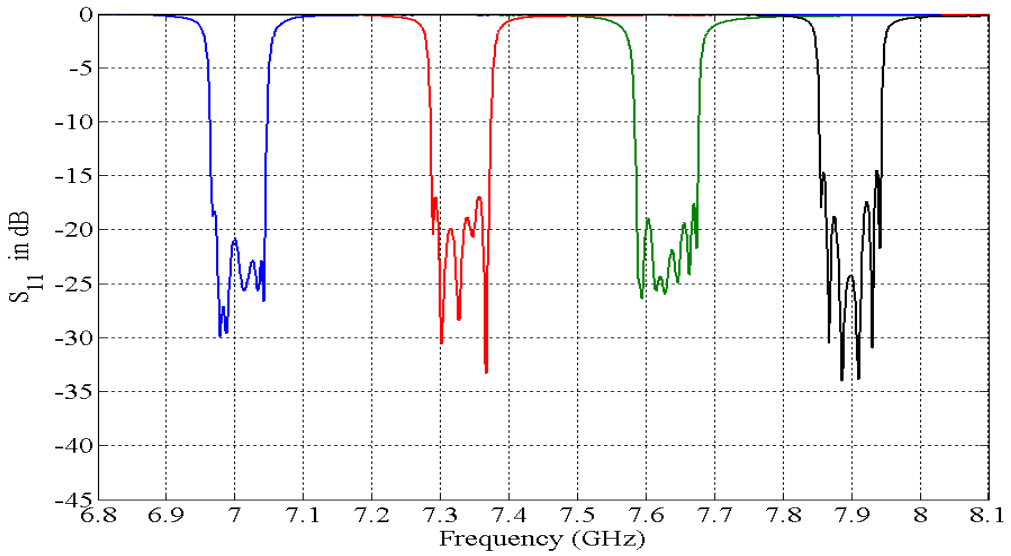

(b) Return Loss Response

Figure 3.32: Measured tuning response of the constant bandwidth 7-pole tunable filter.

3.5 Conclusions

Frequency-tunable cavity combline bandpass filters with constant absolute bandwidth have been investigated. It was shown in theory and experiment that the normalized coupling values can be held constant just by careful design of filter geometry and without using any extra compensation circuit. Since coupling values remain fairly independent of the resonant frequency, only the gap sizes between tuning discs and metallic posts need to be adjusted in order to tune the filter. This methodology was applied to design/implement two different tunable filters: a 5-pole C-band tunable Chebyshev filter with the tuning range of $4.9 - 6$ GHz and the constant absolute bandwidth of 42 MHz and an X-band 7-pole tunable Chebyshev filter with the tuning range of $7 - 8$ GHz and the constant absolute bandwidth of 80 MHz. Filters were tuned using an automated piezoelectric motor tuning. A stable frequency response was observed over the tuning range in both filters. In specific, the bandwidth variation of the 5-pole and 7-pole filters were respectively $\pm 5.3\%$ and $\pm 6.7\%$ over their tuning range.

Chapter 4

Fully Tunable Bandpass Filters with a Wide Tuning Range

4.1 Introduction

To efficiently support multiple frequency bands in the next generation wireless networks, the RF front end needs to be fully configurable. The band select filter is one of the key component of the RF front end. To support multiple frequency band coverage in a small form factor, a fully tunable bandpass filter is required. In a fully tunable filter, both centre frequency and bandwidth are tunable. In the previous chapter, the design of constant bandwidth tunable cavity combline filters was discussed. The focus of this chapter is on bandwidth tuning. A common method to achieve bandwidth tunability is by individual control of the coupling coefficients. That is to have coupling mechanisms that are capable of adjustment during the filter tuning process [42, 43]. For a recent review of this method in planar filters see [44]. In another method, two tunable bandpass filters are cascaded through a transmission line or an isolator to form a frequency and bandwidth tunable filter [24]. The main challenge in this approach is that both filters should maintain their

in-band and rejection performance when the centre frequency is being tuned, a problem that was addressed in the previous chapter. Therefore, we use the cascaded method to achieve the bandwidth tunability.

4.2 Objectives

Bandwidth flexibility is a key characteristic of radio transmitter in 4G/5G cellular communication systems and different 3GPP LTE Advanced bands with flexible bandwidth requirements are expected to be covered. Our objective in this chapter is to design a fully tunable highly selective bandpass filter from 1.8 GHz to 2.6 GHz with $20-100$ MHz bandwidth tunability.

The bandwidth tunability is achieved by cascading two properly designed tunable bandpass filters connected to each other through an isolator or a transmission line. To have a highly selective cascaded response, each of the constituent bandpass filters needs to be highly selective. To achieve high selectivity, order six Chebyshev filters with 25 dB return loss are used to realize the constituent filters with the coupling-routing diagram depicted in Fig. 4.1.

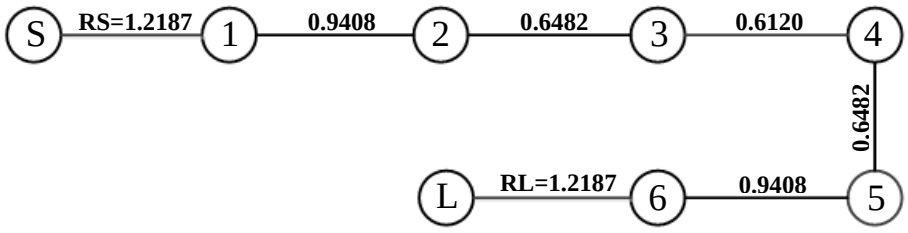

Figure 4.1: Coupling-routing diagram of the six-pole Chebyshev filter.

4.3 Theoretical Background

4.3.1 Constant Return Loss Filter Design

The simplest method to achieve bandwidth tunability over a frequency range is to cascade two constant bandwidth tunable filters. However, as discussed in Chapter 3, designing constant bandwidth tunable filters over a wide tuning range is challenging. Since only the cascaded response matters, the constituent filters should only maintain a constant return loss in the tuning range and it is absolutely unnecessary to keep their absolute bandwidth constant. In fact, as we show in the following, it is possible to maintain the return loss constant over a wide tuning range while the bandwidth is changing.

The return loss of a bandpass filter with centre frequency f_0 and bandwidth BW is described in terms of its coupling elements by

$$S_{11}(\lambda) = 1 + 2jR_S[\lambda\mathbb{I}_N - j\mathbf{R} + \mathbf{M}]^{-1}_{11}. \tag{4.1}$$

The return loss of a band pass filter with $\mathbf{M}^{\text{new}} = \gamma\mathbf{M}$ and $\mathbf{R}^{\text{new}} = \gamma\mathbf{R}$ would be

$$S^{\text{new}}_{11}(\lambda) = 1 + 2j\gamma R_S[\lambda\mathbb{I}_N - j\gamma\mathbf{R} + \gamma\mathbf{M}]^{-1}_{11} \tag{4.2}$$

$$= 1 + 2jR_S[\frac{\lambda}{\gamma}\mathbb{I}_N - j\mathbf{R} + \mathbf{M}]^{-1}_{11} = S_{11}(\frac{\lambda}{\gamma}). \tag{4.3}$$

Therefore, the new return loss at normalized frequency λ is equal to the previous return loss evaluated at λ/γ. As it was shown in Chapter 3, λ is almost independent of the centre frequency and hence, the mapping $\lambda \to \lambda/\gamma$ is equivalent to $BW^{\text{new}} = \gamma BW$.

As an example, the impact of scaling the coupling elements and normalized input/output impedance parameters on transmission and reflection coefficients is depicted in Fig. 4.2 for a six pole Chebyshev filter with 25 dB return loss and $\gamma = 0.7, 1.4$.

From a practical viewpoint, it is difficult to have an identical scaling factor for all coupling coefficients and normalize input/output impedance. Specially, the scaling factor

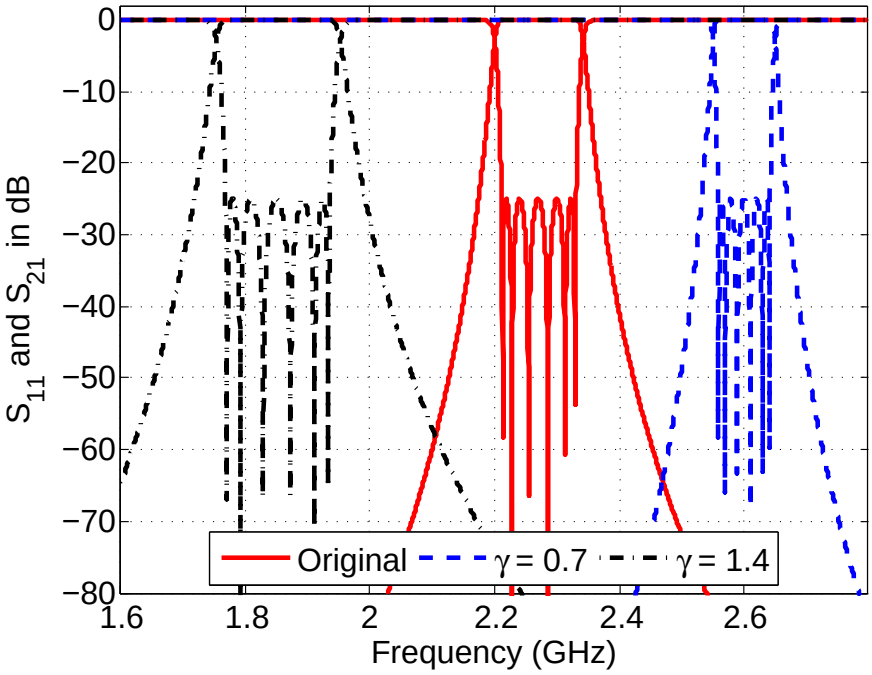

Figure 4.2: Scaling the coupling matrix and normalized input and output impedance of a six pole Chebyshev filter for $\gamma = 0.7, 1.4$.

of input/output impedance is slightly different from that of coupling matrix elements. Therefore, we need to consider two scaling factors: γ_M for coupling matrix elements and γ_R for normalized input/output impedance. The impact of mismatch in scaling factors (γ_M/γ_R) on return loss is depicted in Fig. 4.3 for a six pole Chebyshev filter with 25 dB return loss. As it can be seen from this figure, a mismatch of 20% can deteriorates the return loss by almost 12 dB. Therefore, it is essential to keep the mismatch factor small in order to maintain an acceptable return loss in the tuning range.

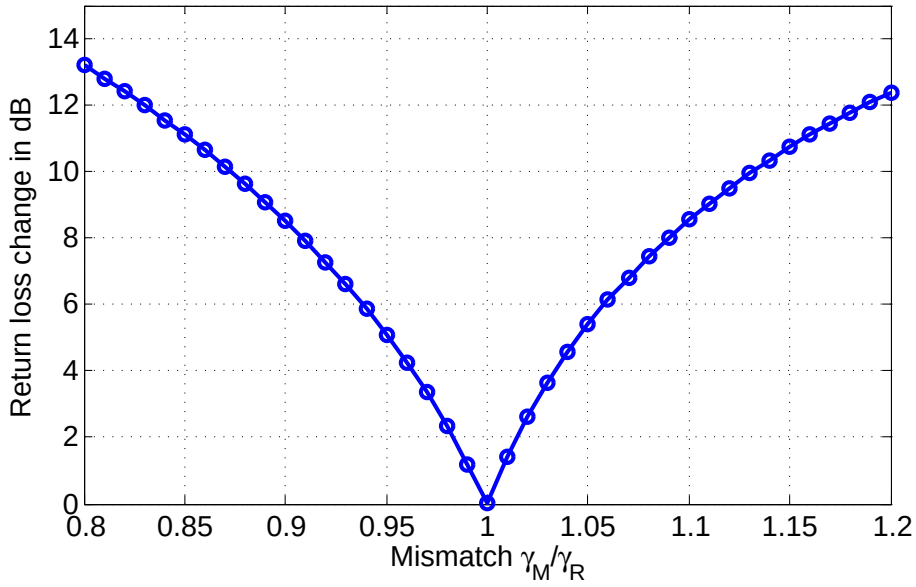

Figure 4.3: Impact of mismatch in scaling of the coupling matrix and normalized input/output impedance on return loss of a six pole Chebyshev filter with $RL = 25$ dB.

4.3.2 Cascading Element Design

Consider a network consisting of two filters with scattering matrices $[S^A]$ and $[S^B]$ which are connected to each other through an interconnecting network with scattering matrix $[S^M]$ as depicted in Fig. 4.4. Furthermore, assume that

$$[S^M] = \begin{bmatrix} 0 & \alpha \\ \beta & 0 \end{bmatrix}. \tag{4.4}$$

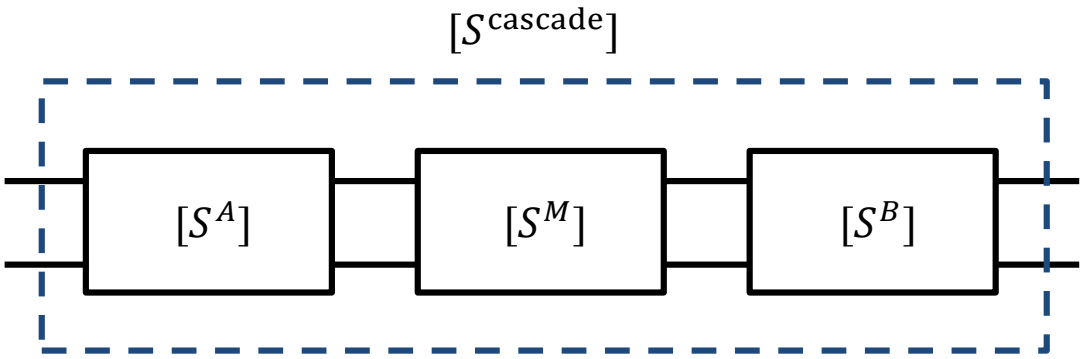

Figure 4.4: Two filters cascaded through an interconnecting two-port network

It is not difficult to show that the scattering matrix of the overall network is given by

$$\begin{aligned} S_{11}^{\text{cascade}} &= S_{11}^{A} + \frac{\alpha\beta S_{12}^{A} S_{11}^{B} S_{21}^{A}}{\Delta}, \\ S_{12}^{\text{cascade}} &= \frac{\alpha S_{12}^{A} S_{12}^{B}}{\Delta}, \\ S_{21}^{\text{cascade}} &= \frac{\beta S_{21}^{A} S_{21}^{B}}{\Delta}, \\ S_{22}^{\text{cascade}} &= S_{22}^{B} + \frac{\alpha\beta S_{12}^{B} S_{22}^{A} S_{21}^{B}}{\Delta}, \end{aligned} \tag{4.5}$$

with $\Delta = 1 - \alpha\beta S_{22}^{A} S_{11}^{B}$. In case the interconnecting network is an ideal isolator, $\alpha = 0$ and $\beta = 1$ and hence

$$\begin{aligned} S_{11}^{\text{cascade, iso}} &= S_{11}^{A}, \\ S_{12}^{\text{cascade, iso}} &= 0, \\ S_{21}^{\text{cascade, iso}} &= S_{21}^{A} S_{21}^{B}, \\ S_{22}^{\text{cascade, iso}} &= S_{22}^{B}, \end{aligned} \tag{4.6}$$

and the overall transmission coefficient would be the multiplication of individual transmission coefficients. Since isolator has a unidirectional transmission characteristic, the overall

network is not reciprocal. If the reciprocity is a requirement of the filter design, the isolator can be replaced by a lossless transmission line with length ℓ for which $\alpha = \beta = e^{-j\beta\ell}$. In this case

$$\begin{aligned} S_{11}^{\text{cascade, TL}} &= S_{11}^{A} + \frac{e^{-j2\beta\ell} S_{12}^{A} S_{11}^{B} S_{21}^{A}}{\Delta_{TL}}, \\ S_{12}^{\text{cascade, TL}} &= \frac{e^{-j\beta\ell} S_{12}^{A} S_{12}^{B}}{\Delta_{TL}}, \\ S_{21}^{\text{cascade, TL}} &= \frac{e^{-j\beta\ell} S_{21}^{A} S_{21}^{B}}{\Delta_{TL}}, \\ S_{22}^{\text{cascade, TL}} &= S_{22}^{B} + \frac{e^{-j2\beta\ell} S_{12}^{B} S_{22}^{A} S_{21}^{B}}{\Delta_{TL}}, \end{aligned} \tag{4.7}$$

with $\Delta_{TL} = 1 - e^{-j2\beta\ell} S_{22}^{A} S_{11}^{B}$. Therefore, the magnitude of the overall transmission coefficient using an interconnecting transmission line with length ℓ is given by

$$|S_{21}^{\text{cascade, TL}}| = \frac{1}{|\Delta_{TL}|} |S_{21}^{A}||S_{21}^{B}|. \tag{4.8}$$

As it can be seen from the above equation, when $|\Delta_{TL}| \to 0$, the overall transmission coefficient is magnified with a factor of $\frac{1}{|\Delta_{TL}|}$ which adversely affects the out of band rejection. It is possible to reduce this effect by adjusting the length of the transmission line.

4.4 6-pole Filter Design

In order to achieve the required out of band rejection and other design considerations, a tunable 6-pole Chebyshev filter with centre frequency of 2.07 GHz, a bandwidth of 120 MHz, and a return loss of 25 dB is selected for design. Two such filters are then cascaded using an isolator/transmission line to tune the bandwidth over the tuning range. In the following, the design procedure is described in detail.

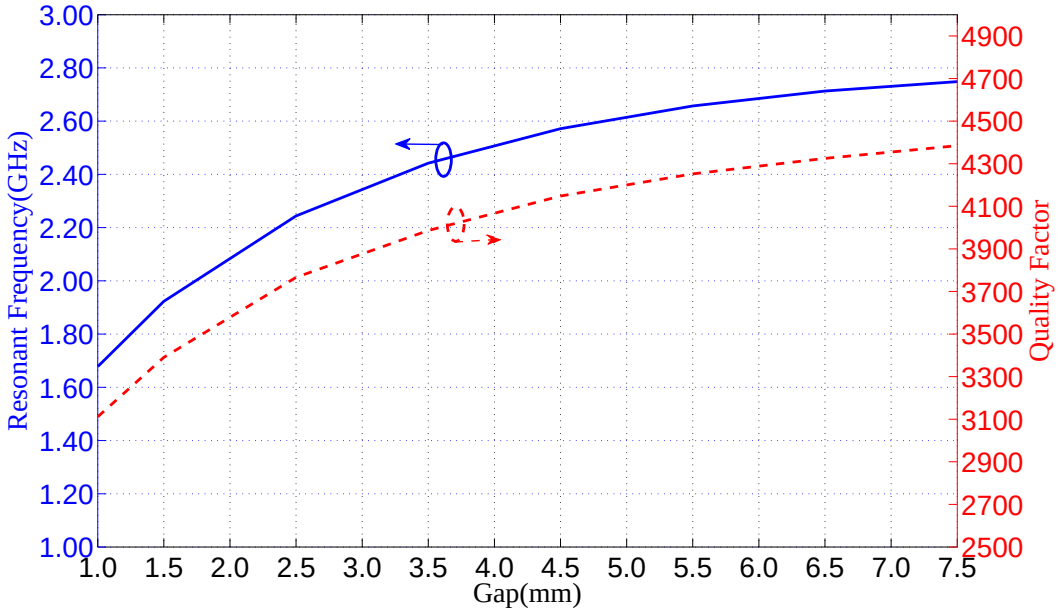

Figure 4.5: EM simulation results of the tunable resonator

4.4.1 Design

In order to obtain the required wide frequency tuning range (more than 800 MHz), a cubical resonator is designed according to the procedure described in Chapter 3. The resonator dimensions are 28mm×28mm×30mm (length×width×height). A tuning range from 1.8 MHz to 2.6 MHz is achieved by adjusting the gap from 1.5 mm to 6.5 mm. EM simulation results for the tuning range and the unloaded Q values of the proposed resonator are presented in Fig. 4.5. The resonator maintains $Q \geq 3100$ over the tuning range. Note that he resonant frequency is more sensitive to gap variations in lower frequencies.

In order to achieve a stable return loss over the tuning range, adjacent and input/output coupling values are designed to scale with the same factor. Therefore, while the bandwidth is changing over the tuning range, the return loss remains approximately constant as it was discussed before. The variations of adjacent coupling elements and normalized input/output impedance are depicted in Fig. 4.6. As it can be seen from this figure, the

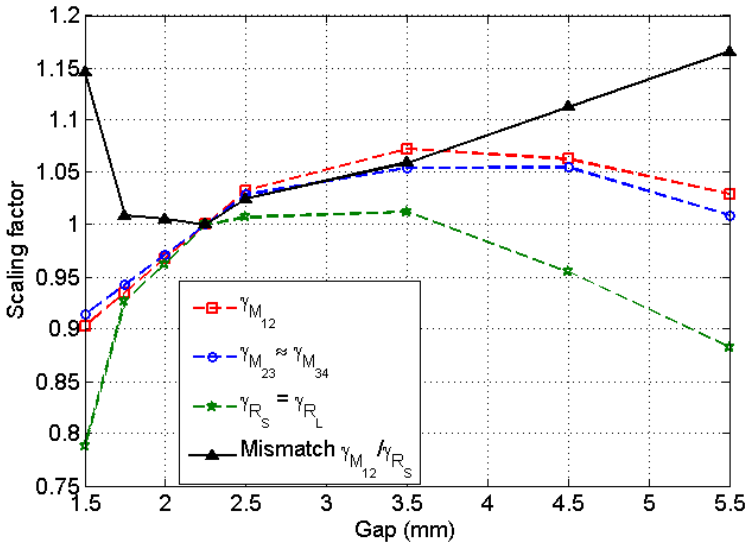

Figure 4.6: Scaling factor of coupling elements and normalized input/output impedance across the tuning range.

maximum mismatch factor over the tuning range does not exceed 15% which according to Fig. 4.3 corresponds to a maximum deterioration of approximately 11 dB in return loss. Note that the coupling values decrease as the centre frequency of filter gets farther from the middle of the tuning range and they are in fact close to their maximum values in the middle of the tuning range. Therefore, the filter bandwidth would be maximum in the middle of the tuning range and decreases as one moves towards the edges of the tuning range.

The 6-pole filter operating at 2.07 GHz with a bandwidth of 120 MHz is then designed using HFSS simulation. The EM model of the filter is illustrated in Fig. 4.7. The vertical irises are exploited to have a better control over the adjacent coupling variations. Moreover, long input/output capacitance probes are used to decrease the variations of input/output coupling value over the tuning range. The reason for selecting an asymmetric structure is to place two such filters in a pre-defined box.

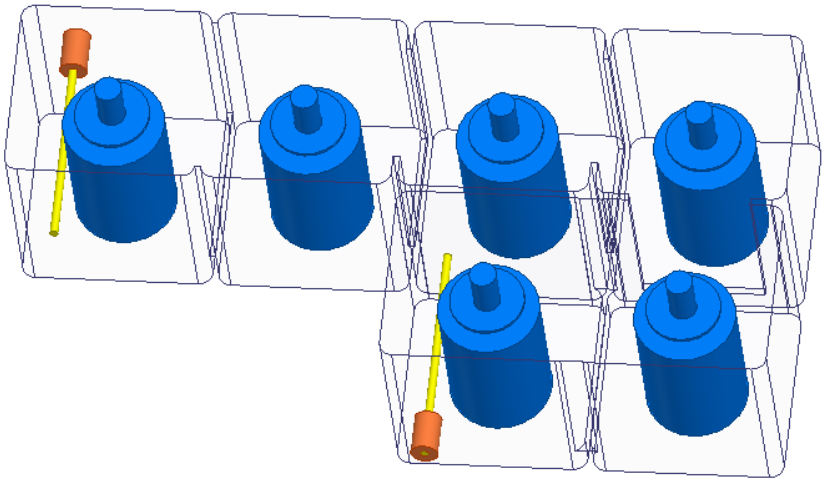

Figure 4.7: EM model of the 6-pole Chebyshev filter

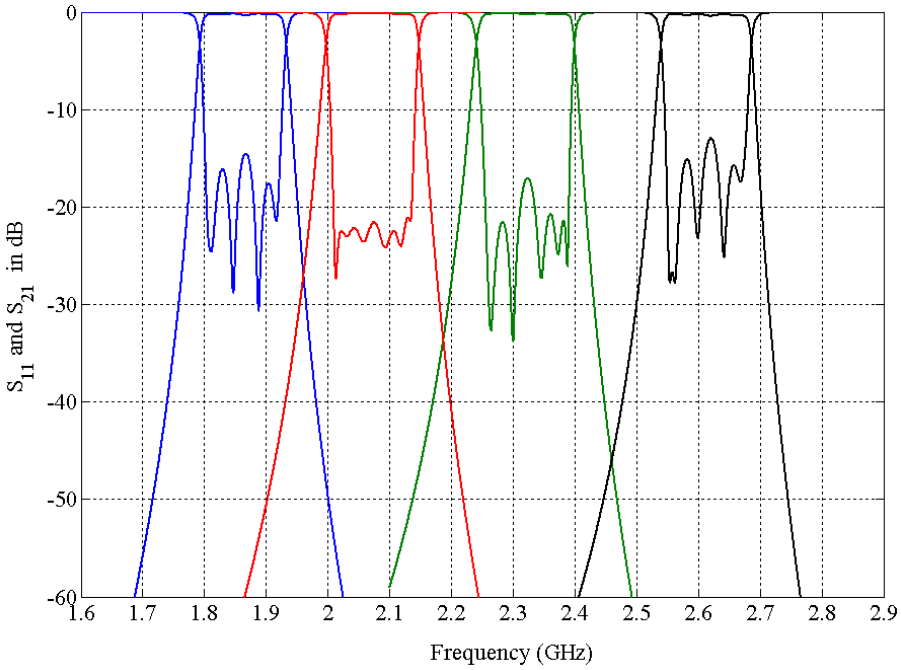

Figure 4.8: EM simulation response of the 6-pole tunable filter.

Filter's parameters are first optimized using the space mapping technique to obtain the desired filter response at $f_0 = 2.07$ GHz. Next, the space mapping technique is applied to the Ness method as described in Chapter 3 to tune the filter across the frequency tuning range by successive adjustment of gap values. The simulation results over the tuning range are depicted in Fig. 4.8. As it can be seen from this figure, the return loss is close to ideal in the middle of the tuning range while it decreases by almost 12 dB at both ends of the tuning range. Moreover, at $f_0 = 2.07$ GHz, the bandwidth is 137 MHz while it decreases to around 100 MHz at both edges of the tuning range. This is in agreement with Fig. 4.6. The group delay follows a similar trend.

4.4.2 Measurement and Test Results

According to prototype designed filter, two identical 6-pole filters are fabricated. The filter housing is made of copper. The centre frequency of each filter can be adjusted manually using tuning screws. The measured tuning response of the filters is demonstrated

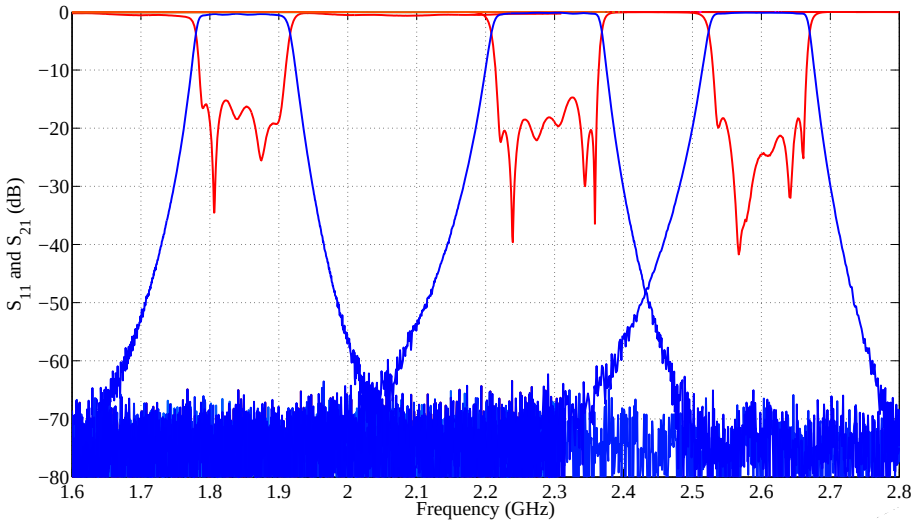

Figure 4.9: Measured response of the 6-pole filter over the tuning range.

in Fig. 4.9. The filter has a tuning range from 1.83 GHz to 2.6 GHz with a stable return loss

over the tuning range. The maximum achievable bandwidth is maximum at the middle of the tuning range (142 MHz) and reduces toward both ends of the tuning range (112 MHz and 125 MHz). The insertion loss is better than 0.5 dB in the passband.

Cascading by Isolator

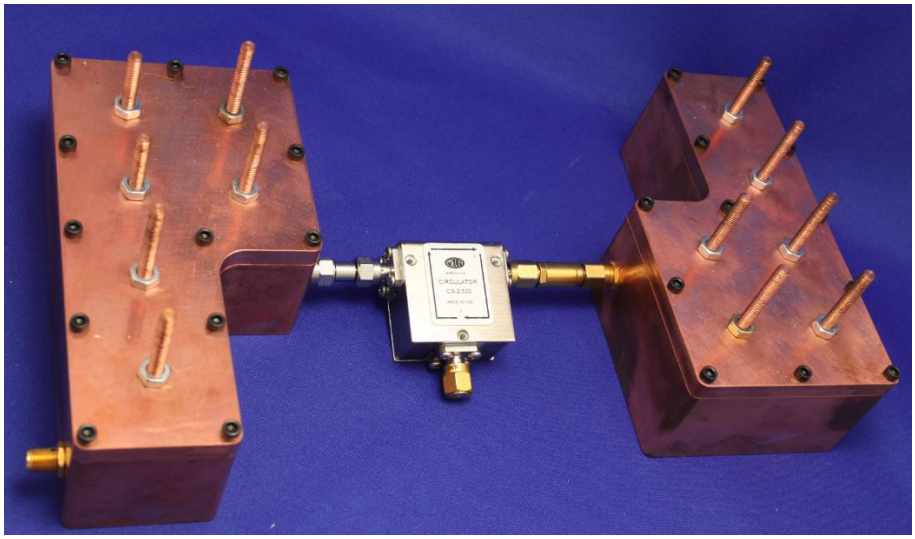

Figure 4.10: Cascading two 6-pole filters using an isolator.

In order to achieve bandwidth tunability, fabricated 6-pole filters are used in cascaded configuration using an isolator or circulator as shown in Fig. 4.10. In order to realize the isolator, the port 3 of the circulator is terminated with a matched 50 Ω load. By tuning the centre frequency of filters with respect to each other, both bandwidth and centre frequency can be tuned. The overlap of two filters determines the bandwidth of the cascaded filter. The measured 3-dB bandwidth tuning performance is shown in Fig. 4.11. This figure shows the transmission and group delay responses of the filter as the bandwidth is tuned across the tuning range. The overall filter achieves a bandwidth tuning of 20-100 MHz over more than 800 MHz tuning range while maintaining a stable in-band and out-of-band performance.

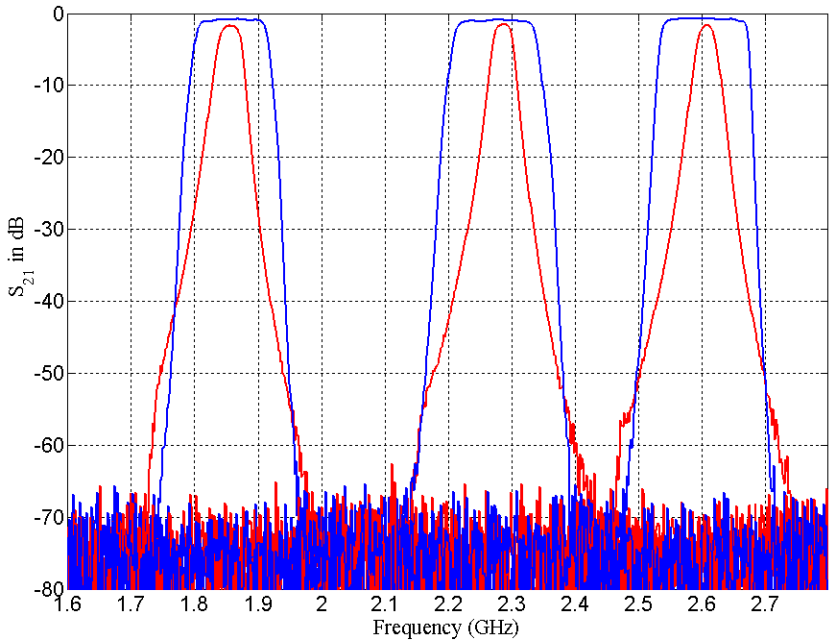

(a) Transmission Responses.

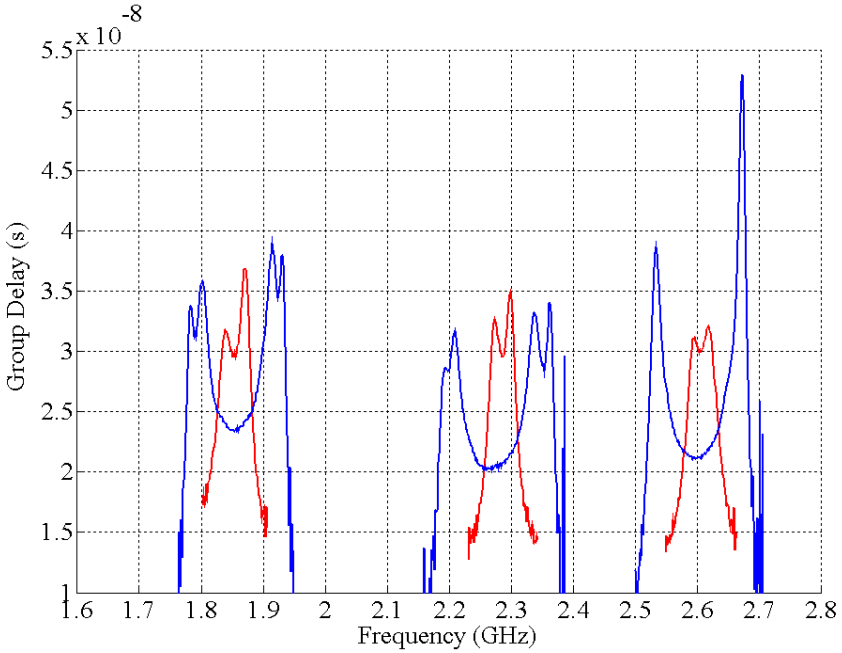

(b) Group Delay Response

Figure 4.11: Measured results of fully tunable filter.

The insertion loss of the cascaded filter is worse than that of each individual filter. The extra loss is partly due to the loss of the circulator and partly due to the addition of insertion loss of filters in the overlap area. One can see from Fig. 4.11 that the insertion loss increases as the bandwidth decreases. Moreover, the VSWR (Voltage Standing Wave Ratio) of the non-ideal isolator adversely affects the return loss response of the cascaded filter. In this design, the circulator has an insertion loss of approximately 0.4 dB and a VSWR of 1.25. The measured transmission and reflection response of the filter are depicted in Fig. 4.12. One can see that the return loss is better than 13 dB for different bandwidth

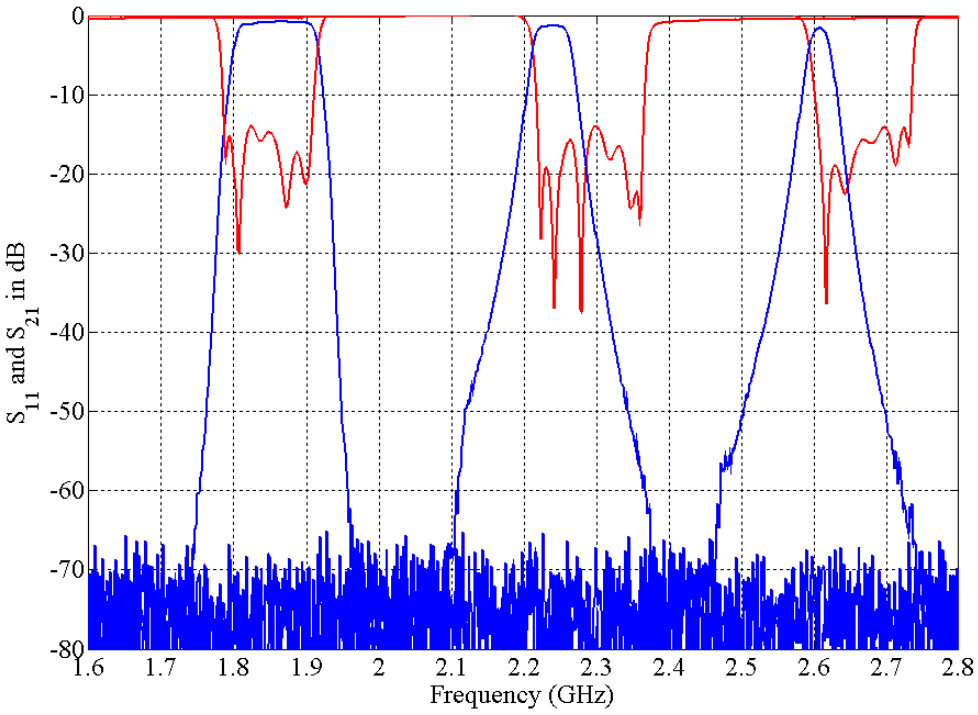

Figure 4.12: Transmission and return loss responses of the filter for different bandwidths over the tuning range.

over the tuning range.

Due to the non-reciprocity of the isolator, the cascaded filter is also non-reciprocal.

So, in case that we need to transmit and receive signals at each port, isolator should be replaced by a reciprocal element such as a transmission line.

Cascading by Transmission Line

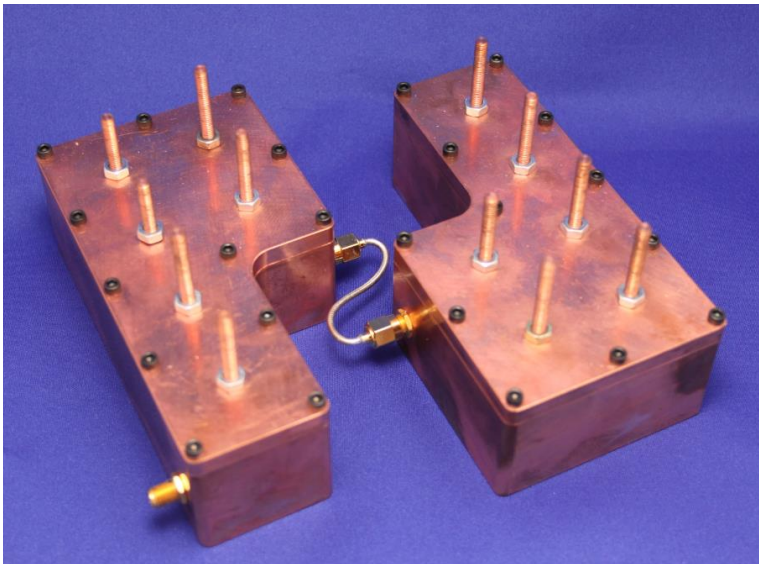

Figure 4.13: Cascading two 6-pole filters using Coaxial line.

When reciprocity is a requirement of filter design, one can use a transmission line to connect the fabricated 6-pole filters as shown in Fig. 4.13. As it was discussed earlier, the length of the inter-connecting transmission line can change the cascaded response. To see this, fabricated filters are connected to each other through transmission lines with different lengths and the cascaded filter response is depicted in Fig. 4.14. As one can see, when the interconnecting network is a transmission line, two spikes appear in the cascaded transmission response and the position and peak value of the spikes change with the length of transmission line. For a length of 17.5 cm, the transmission response has the maximum resemblance to the cascaded one using an isolator. As the filter centre frequency changes, the optimal length for the interconnecting transmission line also changes. Therefore, to

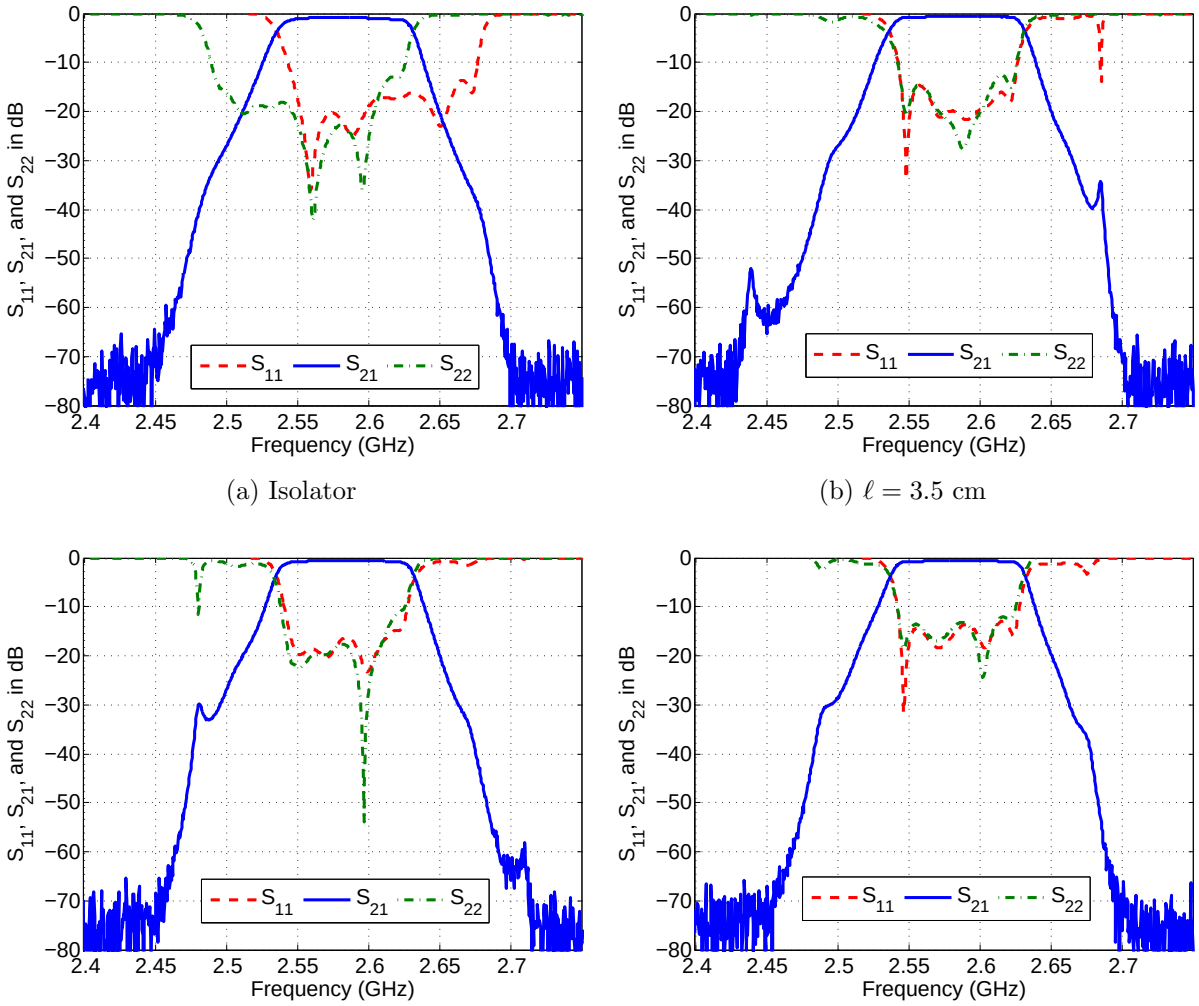

(a) Isolator

(b) $\ell = 3.5$ cm

(c) $\ell = 10.5$ cm

(d) $\ell = 17.5$ cm

Figure 4.14: Measured cascaded response using different interconnecting networks.

cover a wide tuning range, a phase shifter needs to be used as the interconnecting network. The cascaded response of the filter using an interconnecting phase shifter is depicted in Fig. 4.15 for different centre frequencies and bandwidths over the tuning range. One can see that the filter achieves a frequency tuning range of $1.9 - 2.57$ GHz and a bandwidth tuning range of $30 - 100$ MHz.

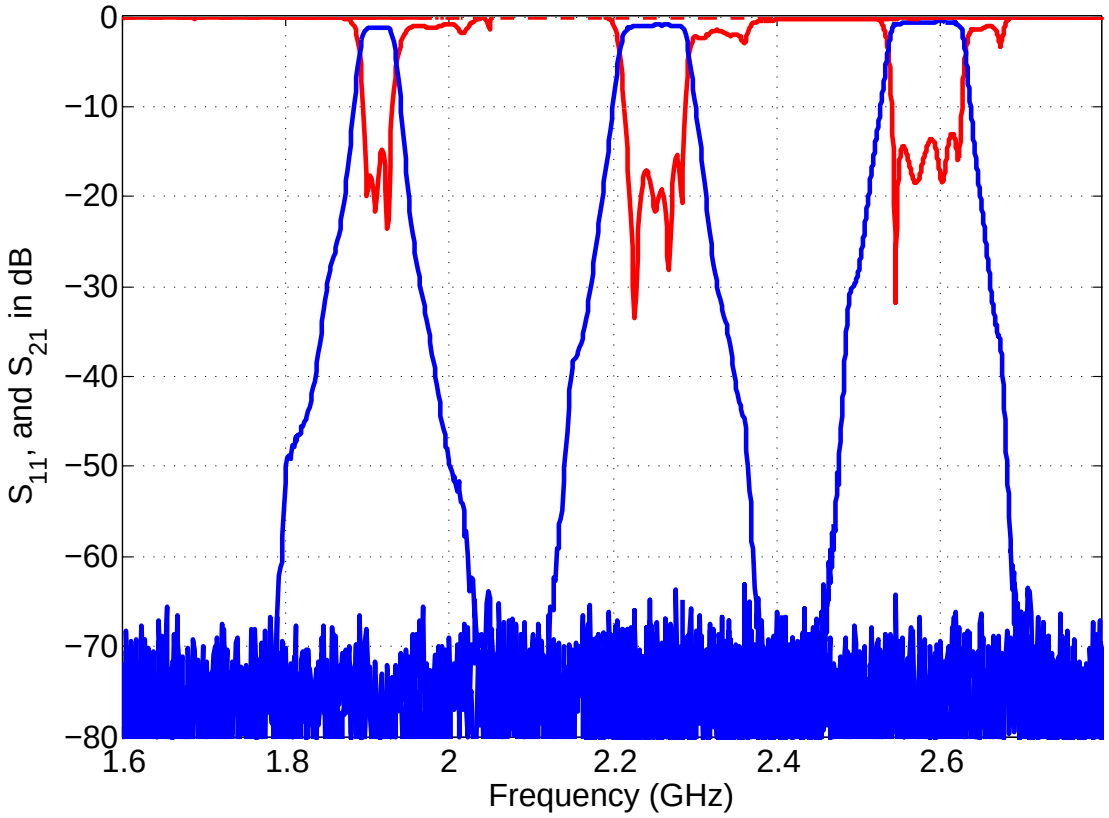

Figure 4.15: Transmission and return loss responses of the filter for different bandwidths over the tuning range.

4.5 Conclusions

The idea of constant return loss filter design was presented and used to design and fabricate two six-pole Chebyshev filters. These filters were then cascaded using an isolator or transmission line to form a fully tunable bandpass filter. The measured filter response has exhibited a 36% centre frequency tunable range from approximately 1.8 to 2.6 GHz with a bandwidth tunability of 20-100 MHz across the tuning range. The filter maintained a stable response with high selectivity and descent return loss over the wide tuning range.

Chapter 5

Fully Tunable Two Port Triplexer Design

5.1 Introduction

Supporting multi-band and multi-standard transmission/reception is an important requirement in the next generation cellular communication systems. To support multi-band communication, multiple fully tunable filters need to be integrated in a switch-less filter bank. For the case of dual band filters, various methods have been proposed. In [45], a fully tunable dual band filter is proposed which comprises two dual-mode single band filters using common input/output lines wherein each filter is realized using a varactor-loaded transmission line dual-mode resonator. Less attention has been directed toward the design of tunable triplexers. In this study, we propose a new structure to obtain a fully tunable two port triplexer. In this structure, three fully tunable bandpass filters are connected to each other by a channelizer at the input port and a combiner at the output port. The channelizer and combiner are realized using coaxial transmission line manifolds. The centre frequency of each band can be individually tuned over a tuning range of 250 MHz.

The 3 dB bandwidth of each band can also be independently tuned from approximately 20 MHz to around 100 MHz. The final design enjoys a high selectivity together with a small form factor. In the following, we describe the proposed structure in detail.

5.2 Objective

Our objective in this chapter is to design a fully tunable two port triplexer with the tuning requirements listed in Table 5.1. The centre frequency and/or bandwidth of each frequency band need to be independently tunable. A return loss better than 13 dB is required in the whole tuning range. Another important requirement is the filter reciprocity. That is exchanging the input and output ports should not change the transmission coefficient. In terms of size, the whole design should fit inside a 120mm×100mm×30mm box (length×width×height). Low loss and high selectivity are other important requirements.

Table 5.1: Frequency and bandwidth tuning requirement for the two port triplexer

	Band 1	Band 2	Band 3
Frequency tuning range (GHz)	$1.85 - 2.105$	$2.155 - 2.41$	$2.49 - 2.69$
Bandwidth tuning range (MHz)	$10 - 100$	$10 - 100$	$10 - 100$

5.3 Proposed Method

The proposed structure consists of three fully tunable bandpass filters which are connected to each other by a channelizer at the input port and a combiner at the output port as depicted in Fig. 5.1. Both channelizer and combiner are realized using coaxial line manifolds. In order to achieve bandwidth tunability as well as high selectivity, each bandpass filter

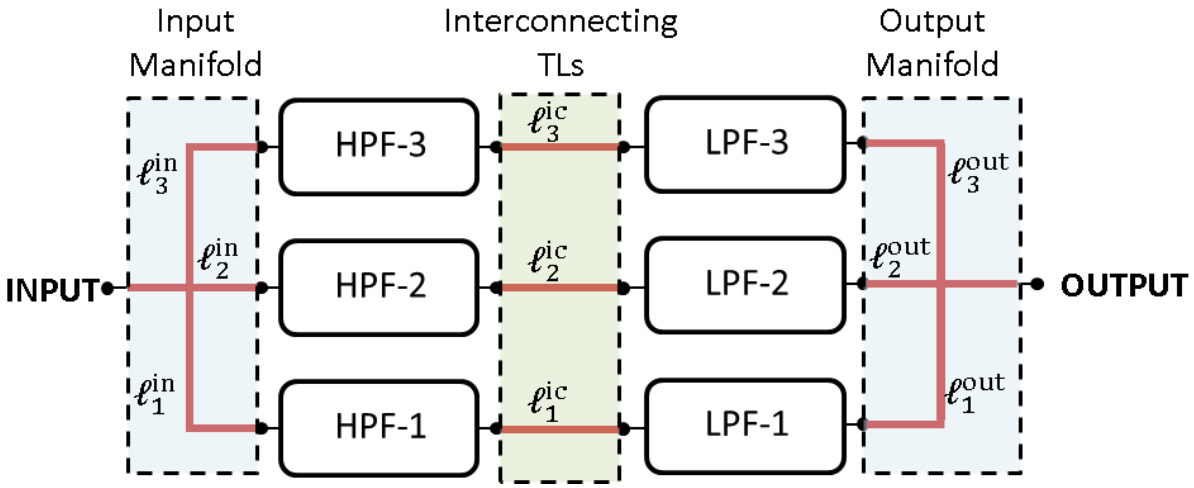

Figure 5.1: Proposed fully tunable two port triplexer structure

consists of two constant bandwidth tunable sub-filters cascaded through a coaxial transmission line. A high level of selectivity could be attained by concentration of rejection. That is to provide rejection only over the band where it is needed [46].

To this aim, in one of the constituent sub-filters, the rejection above the passband is increased while rejection below the passband is relaxed. This filter is referred to as a low-pass filter in the sequel. In the other constituent filter the situation is reversed. That is the rejection below the passband is increased while rejection above the passband is relaxed. This filter is referred to as a high-pass filter in the following. Each of the constituent low-pass or high-pass filters is realized using a 4-pole filter with a 100 MHz bandwidth. Note that the overall two-port network is reciprocal.

The design procedure then consists of the following steps:

- Filter design: This involves the design of the constant bandwidth tunable low-pass and high pass filters for each band and the lengths of the interconnecting transmission lines.

- Input/output manifold design: This involves the design of lengths of transmission lines in input and output manifold. That is $(\ell_1^{\text{in}}, \ell_2^{\text{in}}, \ell_3^{\text{in}})$ and $(\ell_1^{\text{out}}, \ell_2^{\text{out}}, \ell_3^{\text{out}})$ in Fig. 5.1.

5.4 Filter Design

5.4.1 Coupling Routing Diagrams

The canonical coupling routing diagram of a 4-pole Chebyshev filter with one transmission zero on the left or right side of the passband is depicted in Fig. 5.2. Note that the transmission zero is created by the cross coupling between resonators 2 and 4, namely M_{24}, in this configuration. Moreover, a positive M_{24} corresponds to a transmission zero on the right side of the passband. Similarly, a negative M_{24} corresponds to a transmission zero on the left side of the passband.

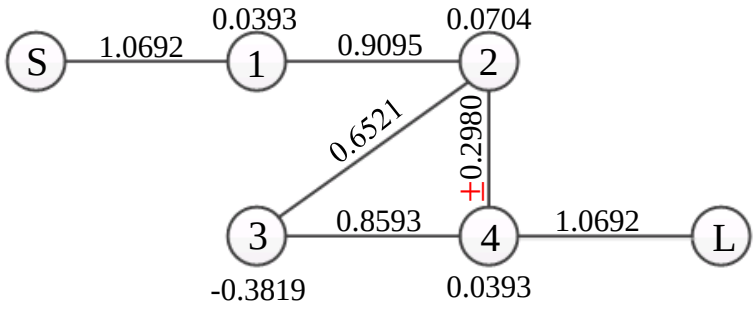

Figure 5.2: Coupling routing diagram for a 4-pole Chebyshev filter with one transmission zero

The positive cross coupling M_{24} can be realized by inductive coupling using an iris as described in the previous chapters. The negative cross coupling can be realized by

capacitive coupling using a capacitive probe*. A capacitive probe is basically an insulated section and usually supported by a dielectric sleeve inside an iris opening. The probe has close proximity to the resonating posts at both ends. Unlike the irises, capacitive probes do not lend themselves easily to constant bandwidth design. It is worth mentioning that the negative coupling can also in principle be realized using irises as in [47]. Such a realization, however, is not viable in the current design due to the relatively large bandwidth and small form factor requirements. To be more specific, the size specification of the design limits the size of each single cavity resonator to 20mm×20mm×30mm and the method described in [47] can not achieve the required coupling value using such a small resonator.

The constituent low-pass and high-pass filters are designed for the maximum bandwidth, i.e. 100 MHz and they need to maintain a constant bandwidth (or more generally a constant return loss) across the tuning range. As we will see in the next section, physical realization of the coupling routing diagram in Fig. 5.2 is not difficult to achieve when M_{24} is positive. However, this is not the case for negative M_{24} due to the fabrication complications of the diagonal coupling element. Therefore, alternative coupling routing diagrams need to be found for this case. Two possible candidates are the box section configuration [48] and the elliptic filter configuration as depicted in Fig. 5.3. As it can be seen from this figure, there is no diagonal coupling in these configurations. The input and output ports are at the opposite side corners in the box section configuration while they are at the same side in the elliptic filter configuration. The box section configuration creates a single transmission zero at the left side of the passband† while the elliptic filter creates two symmetrical transmission zeros at both sides of the passband. Therefore, a smaller

*Note that a capacitive or inductive cross coupling is determined according to their respective signs in the coupling matrix. That is when all elements of the coupling matrix have the same sign, the elements of the coupling matrix are either all inductive or all capacitive. By convention, a positive sign represents the inductive (magnetic) coupling and a negative sign represents the capacitive (electric) coupling.

†An interesting feature of the box section is that by changing the sign of the self couplings values, the transmission zero will appear on the opposite side of the passband. This can be easily achieved in practice by retuning the resonators.

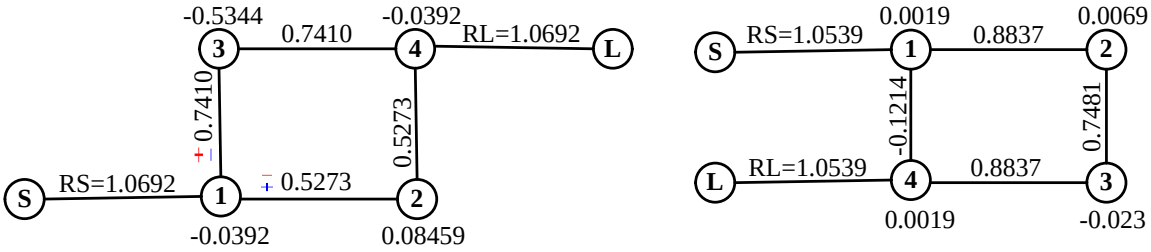

(a) The box section configuration

(b) The elliptic filter configuration

Figure 5.3: Alternative coupling routing diagrams for having a transmission zero on the left side of the passband

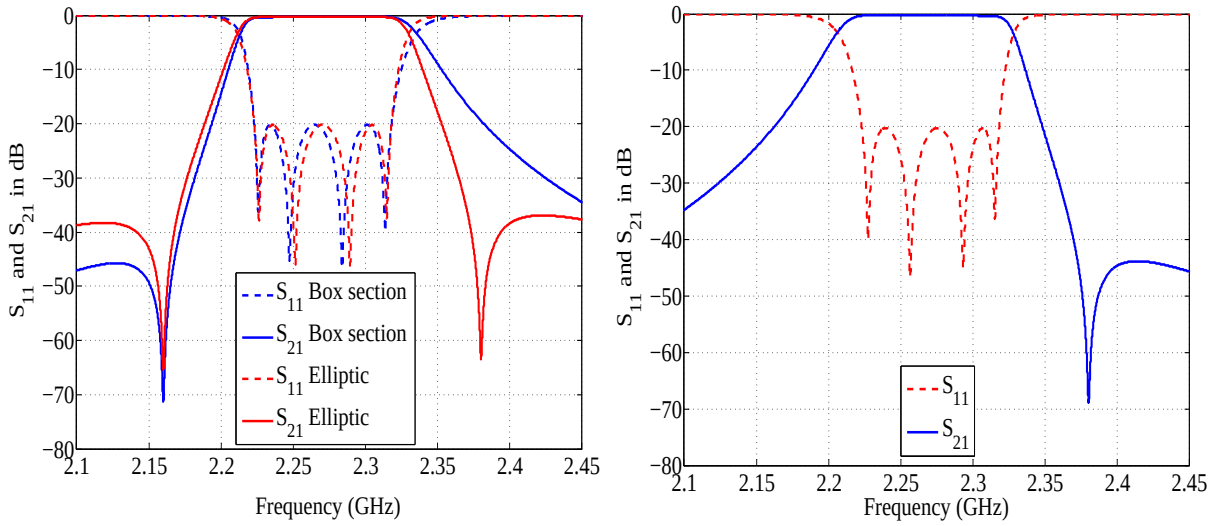

(a) high-pass filter

(b) low-pass filter

Figure 5.4: Ideal frequency response of the low-pass and high-pass filters

out of band rejection can be achieved at the left side of the passband using the elliptic filter configuration. The negative coupling in the box section could be either M_{12} or M_{13}. However, as it will be discussed in the next section, the negative M_{13} is preferred in terms of parasitic coupling behaviour. The ideal response of the low-pass and high-pass filters are depicted in Fig. 5.4.

One may notice that the value of the negative coupling in the box section configuration is almost 6 times bigger than that in the elliptic filter configuration. Due to the small form factor requirements, realizing large negative coupling values using capacitive probe turns out to be challenging especially in a constant bandwidth design. For this reason, the box section configuration is more limited in terms of the tuning range.

5.4.2 Low Pass Filter Design

Our objective in this section is to design three tunable low-pass[†] filters with a return loss of 20dB and a bandwidth of 100 MHz. The coupling routing diagram is depicted in Fig. 5.2 with positive sign for M_{24}. Each filter has to cover 250 MHz frequency tuning range. Compact size and low losses are other requirements. A cubical resonator is designed to cover the tuning range of 250 MHz with a quality factor better than 2000 in the tuning range. One can see from Fig. 5.5 that the variation of resonant frequency is almost linear with respect to gap variations. This feature is very useful during filter tuning especially for automated tuning. Also, the quality factor remains almost constant over the tuning range.

The resonator dimensions are 19mm×19mm×26mm (length ×width×height). In order to get an acceptable quality factor using such a small resonator, the filter order needs to be small and therefore it is selected to be 4. This yields an acceptable insertion loss over the tuning range. To realize constant adjacent and cross coupling values over the tuning range, vertical irises are exploited. Due to the required compact size and large

[†]See Section 5.3 for the definition of low-pass/high-pass filter in this context.

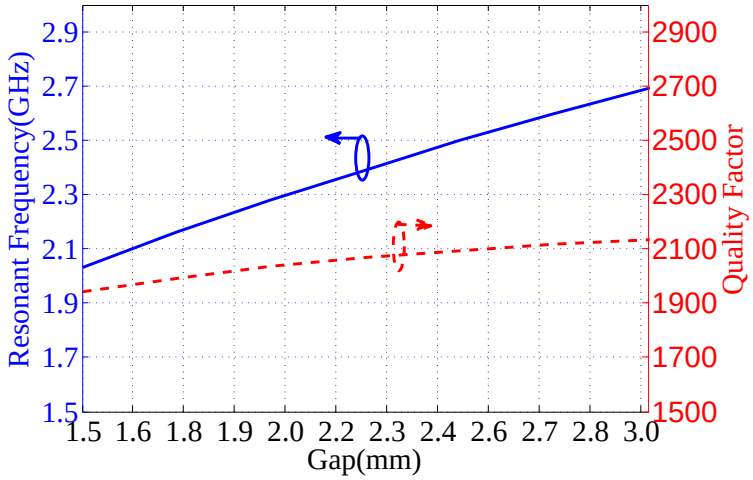

Figure 5.5: Coupling-routing diagram for realizing asymmetric 4-pole filter.

cross coupling M_{24}, physical realization of the filter needs a careful design. In specific, resonator 2 needs to have three iris openings to couple with all other resonators, and an asymmetric structure is required to support this as depicted in Fig. 5.6. Furthermore, in order to achieve the required coupling value of $M_{23} = 0.6521$, a metal bar is used to directly connect resonators 2 and 3. This metal bar passes through the iris opening and enhances the coupling between these resonators. Moreover, for realizing the large value of the input/output coupling, inductive probes are used which are tapped to the first and last resonator posts. The input/output coupling value is almost constant over the tuning range. The EM simulation results of all three bands at the middle of their tuning range are depicted in Fig. 5.7.

One can see that all three filters have a high concentration of rejection on their right side of the passband. This is partly due to the effect of the designed transmission zero and partly due to the parasitic transmission zero which is created by the parasitic coupling between resonators 1 and 4. Because of the required small size, all filters are selected to have the same cavity size. Therefore, in order to design the filter for the lowest frequency band, the height of the posts and the radius of the tuning disks are increased. The prototype

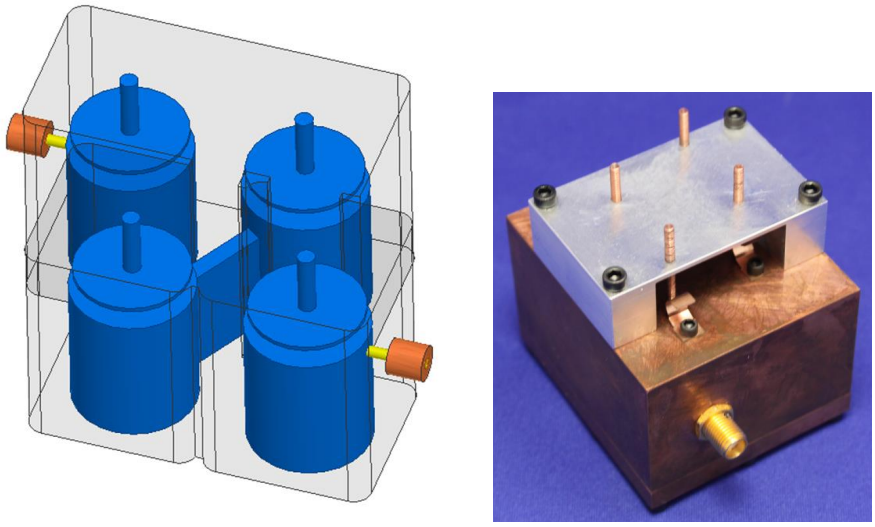

(a) EM model (b) Fabricated structure

Figure 5.6: Structure of the low-pass filter

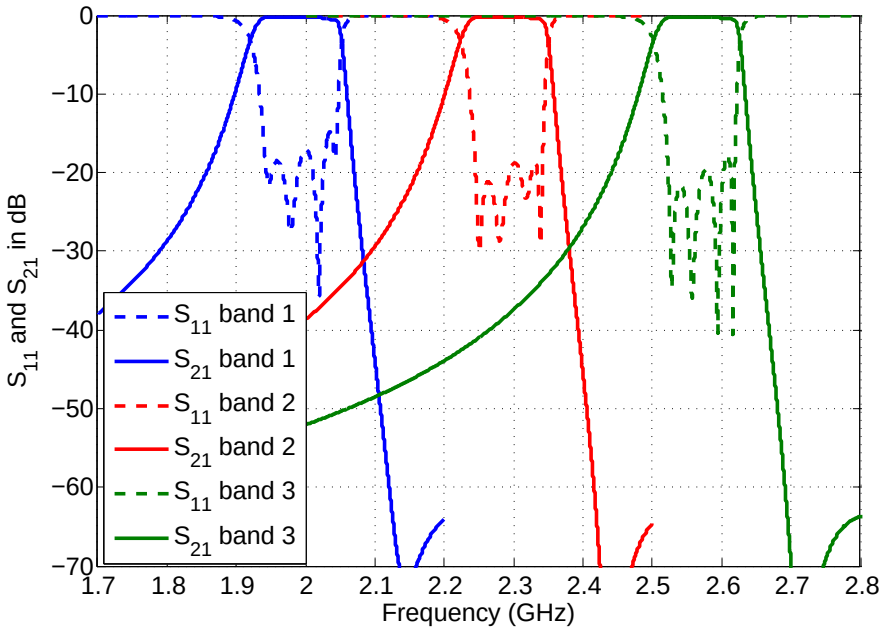

Figure 5.7: EM simulation results of 4-pole low-pass filters for different frequency bands

designed filter, fabricated with copper, is depicted in Fig. 5.6. The filter is manually tuned using the tuning screws. The measurement results of the first, second ,and third band filters over the tuning range is depicted in Fig. 5.8, Fig. 5.9,and Fig. 5.10 respectively. One can see that the filter covers the tuning range with a return loss better than 15 dB. Since the gap size is proportional to the filter centre frequency, tuning the filter in the lower frequency ranges requires the tuning screw to penetrate further which in turn increases the insertion loss as it can be seen from Fig. 5.8. The same procedure is repeated for the other two bands.

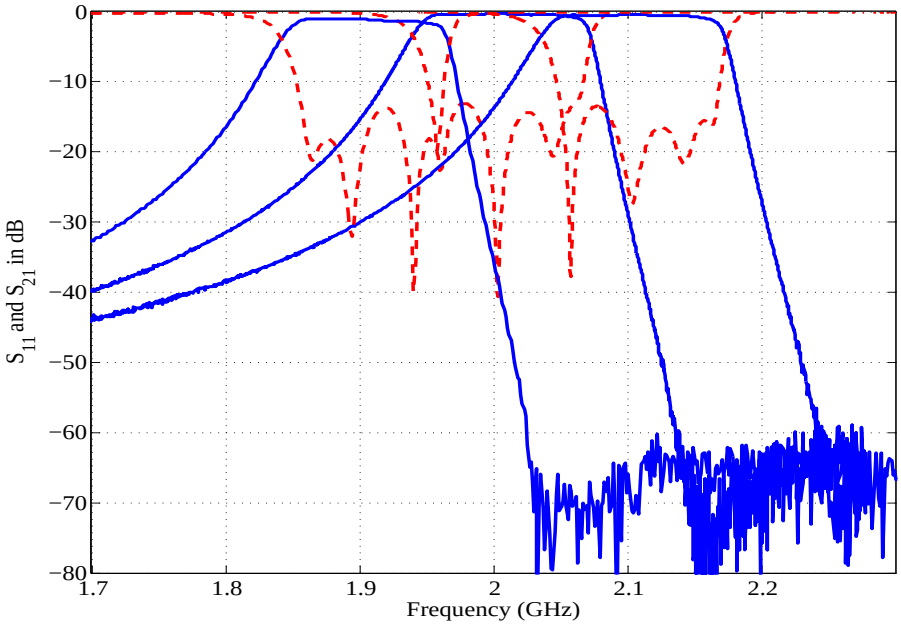

Figure 5.8: Measurement results for the first band filter across the tuning range.

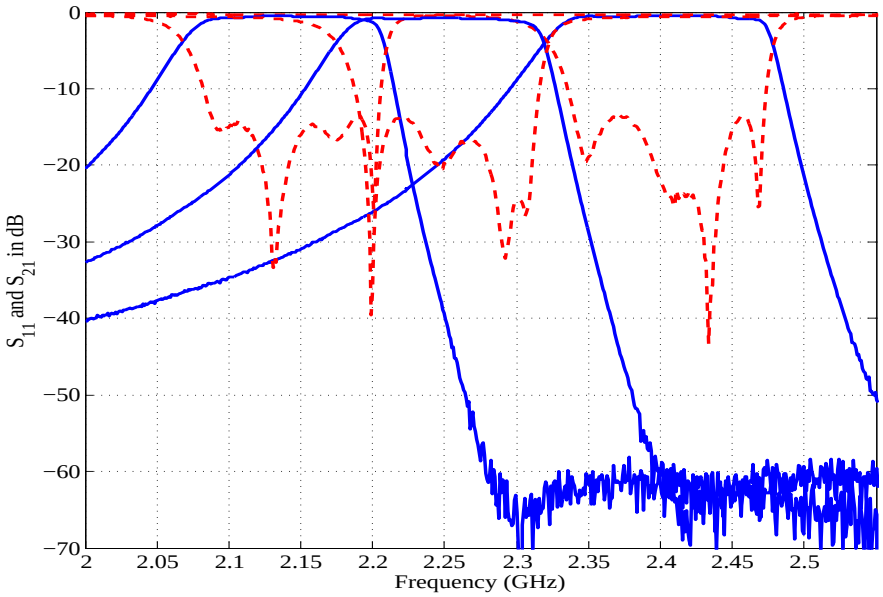

Figure 5.9: Measurement results for the second band filter across the tuning range.

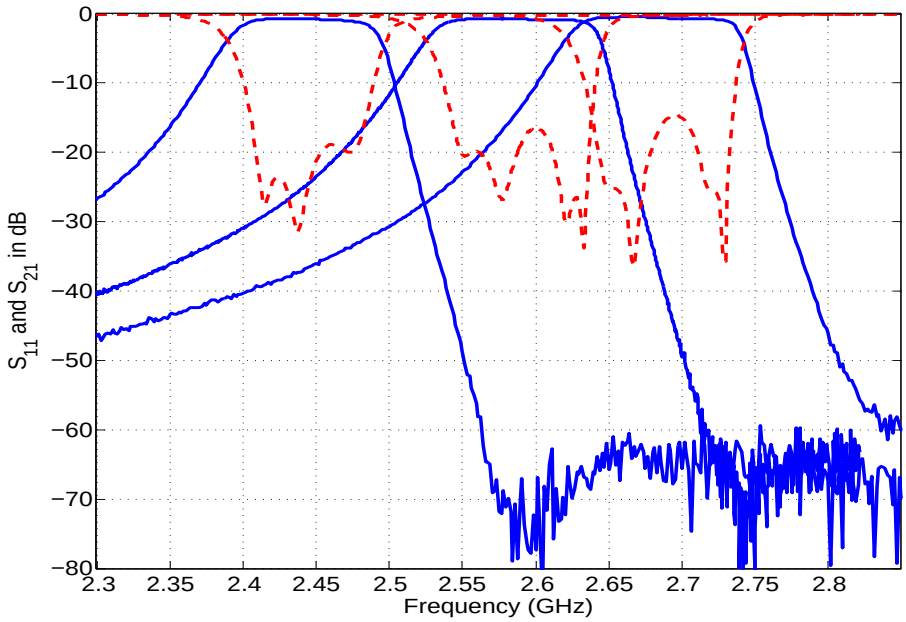

Figure 5.10: Measurement results for the third band filter across the tuning range.

5.4.3 High Pass Filter Design

Our objective in this section is to design three tunable high-pass† filters with a return loss of 20dB and a bandwidth of 100 MHz. Two different configurations (box section and elliptic) are considered as depicted in Fig. 5.3. The resonator dimensions are 20mm×20mm×30mm (length ×width×height). The size of the resonating post and the tuning disk are parameters that can be changed to realize the filter in other frequency bands.

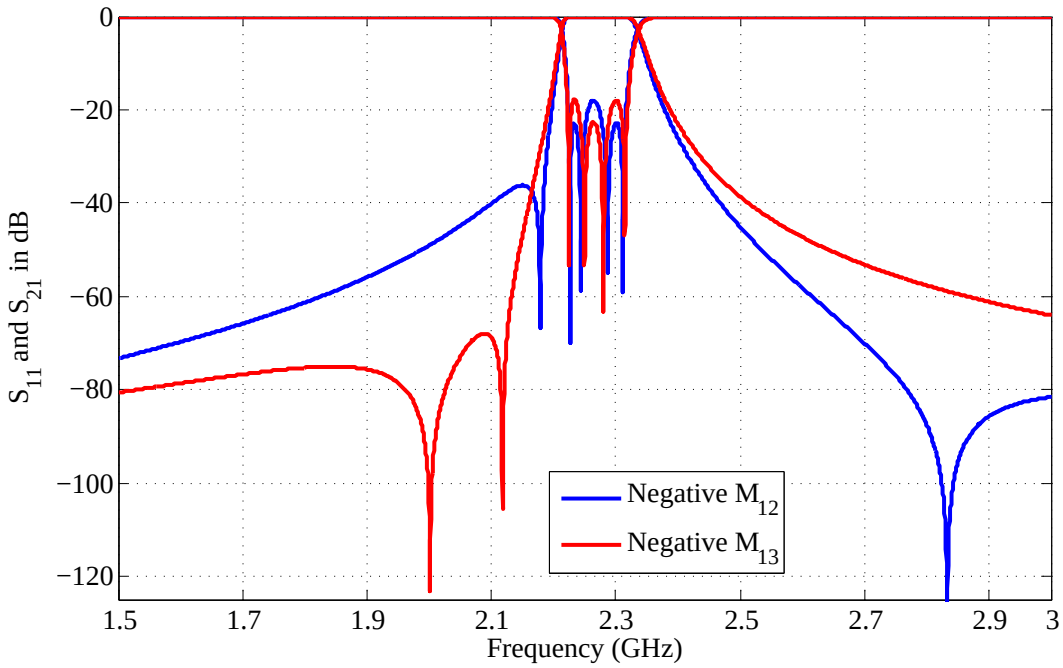

Figure 5.11: Impact of the parasitic coupling $M_{14} = 0.03$ on the filter response for two different realizations of the box section configuration.

In the box section design, vertical irises are exploited to realize constant positive coupling values over the tuning range according to the design principles described in Chapter 3. The negative coupling element could be either M_{12} or M_{13} as depicted in Fig. 5.3a. Even

†See Section 5.3 for the definition of low-pass/high-pass filter in this context.

though both cases yield the same response in ideal situation, the existence of parasitic coupling between resonators 1 and 4 is inevitable in practice due to the small size of the filter. Fig. 5.11 illustrates the impact of parasitic coupling $M_{14} = 0.03$ on the filter response for negative M_{12} and negative M_{13}. As it can be seen from this figure, one can achieve a better concentration of rejection on the left hand side of the passband using negative M_{13}. Therefore, the case of negative M_{13} is preferable in terms of our objective.

The negative coupling M_{13} is realized using a capacitive probe. As explained earlier, realizing constant large negative coupling values over a tuning range is challenging. The value of M_{13} determines the position of the transmission zero and simultaneously affects the filter bandwidth. Due to these limitations, the filter tuning range is limited to approximately 100 MHz in the box section configuration.

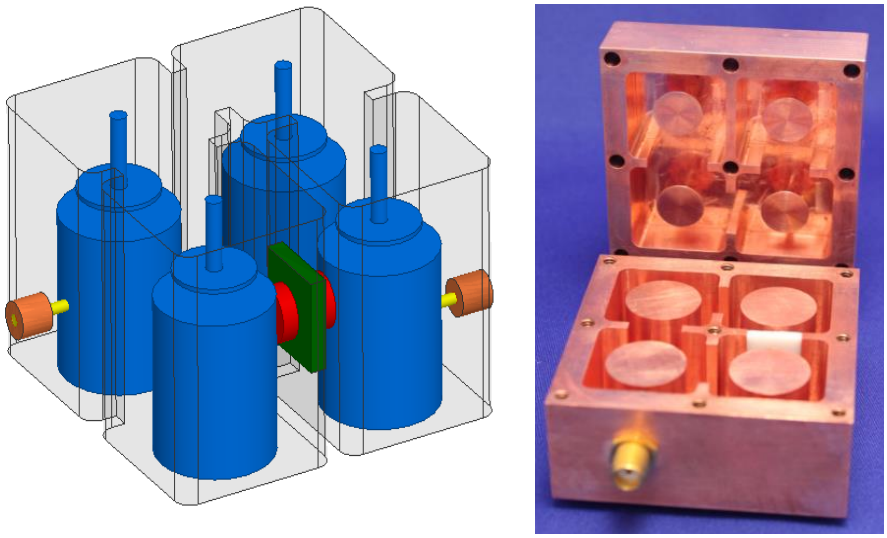

(a) EM model (b) Fabricated filter

Figure 5.12: Structure of the high-pass filter in the box section configuration.

The EM model of the filter is depicted in Fig. 5.12a. The EM simulation results of all three bands at the middle of their tuning range are depicted in Fig. 5.13. One can see that all three filters have a high concentration of rejection on their left side of the passband.

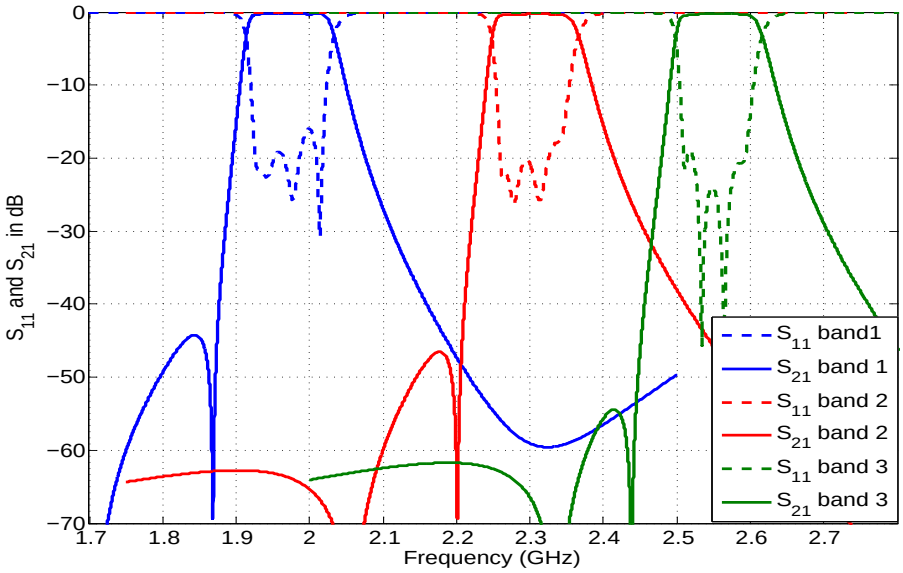

Figure 5.13: EM simulation results of 4-pole high-pass filters for different frequency bands using the box section configuration.

This is partly due to the effect of the designed transmission zero and partly due to the parasitic transmission zero which is created by the parasitic coupling between resonators 1 and 4.

The fabricated filter of band 3 is depicted in fig. 5.12b. The filter housing is made of copper. The measured response of the filter is depicted in Fig. 5.14. It is worth mentioning that self-coupling values in box section configuration not only adjust the resonant frequency of their respective resonators, they also change the position of the transmission zero. Therefore, the same filter can be tuned such that the transmission zero appears on the right side of the passband as depicted in Fig. 5.14b.

In elliptic configuration, the same dimensions for resonators and irises are used. In this configuration, the negative coupling M_{14} is relatively small and has minor variations over the tuning range. The EM simulation results of the second band filter using an elliptic configuration is depicted in Fig. 5.15. One can see that the filter covers the tuning

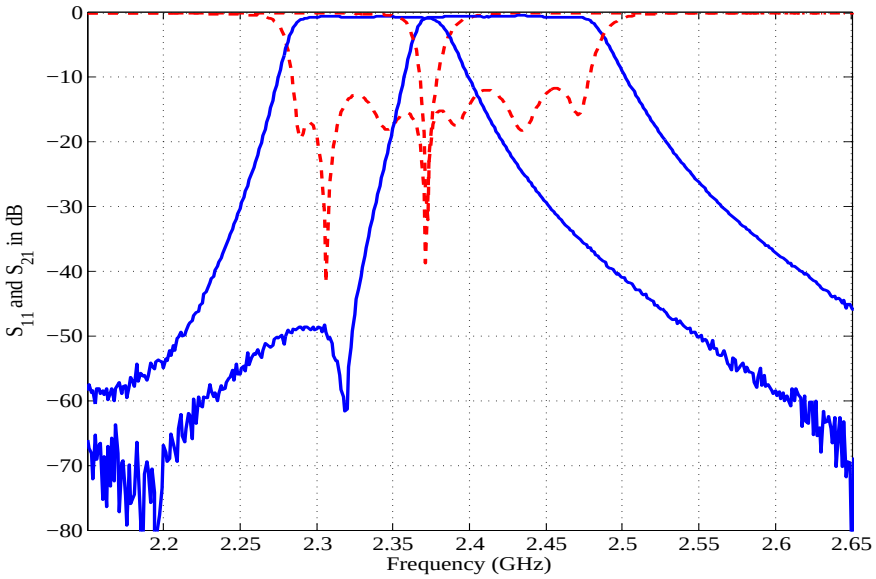

(a) High-pass filter

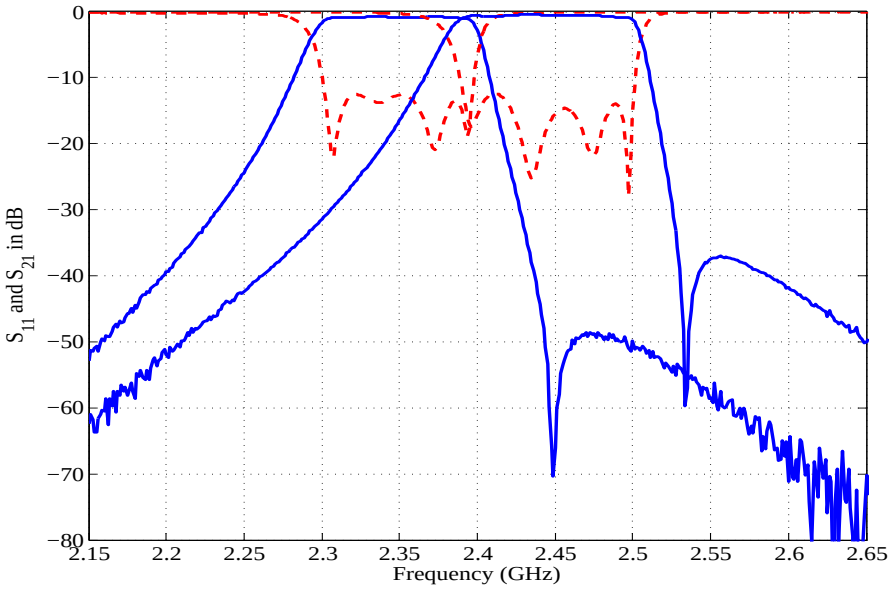

(b) Low-pass filter

Figure 5.14: Measured response of the third band 4-pole high-pass filter with box section configuration. Note that the same filter can be tuned such that the transmission zero will appear on the right side of the passband.

range with a return loss better than 18 dB. The distance of the transmission zeros to the filter centre frequency is inversely proportional to the M_{14} value. Since, as the frequency increases, the value of M_{14} also slightly increases, the position of transmission zeros are getting closer to the filter centre frequency for higher frequency ranges. Even though, the elliptic configuration has an inferior rejection on the left side of the passband with respect to the box section configuration, it covers all the tuning range with an acceptable return loss. Therefore, this configuration would be our choice for designing the two port triplexer.The prototype designed filter, fabricated with copper. The filter is manually tuned using the tuning screws. The measurement results of the first, second ,and third band filters over the tuning range is depicted in Fig. 5.16, Fig. 5.17,and Fig. 5.18 respectively. In order to achieve bandwidth tunability, fabricated Low-pass and elliptic filters are used in cascaded configuration using a transmission line. The measured cascaded response of all three bands at the middle of their tuning range is shown in Fig. 5.19.

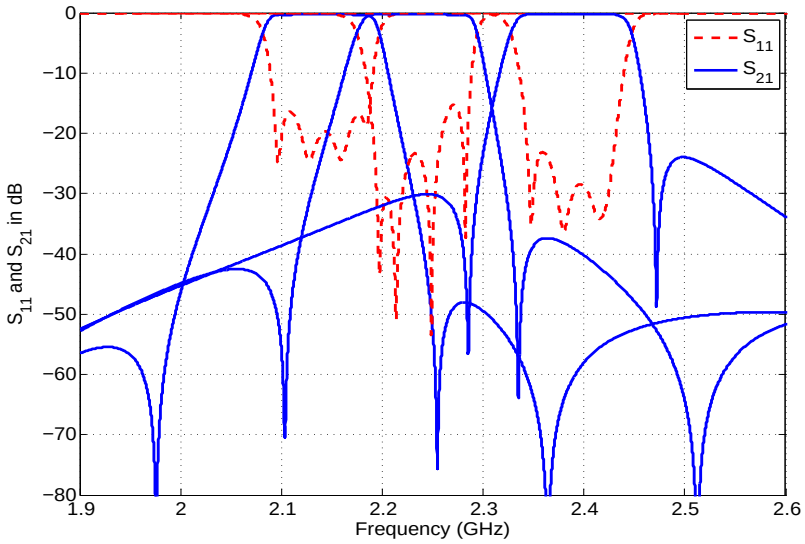

Figure 5.15: EM simulation results for the second band elliptic filter across the tuning range.

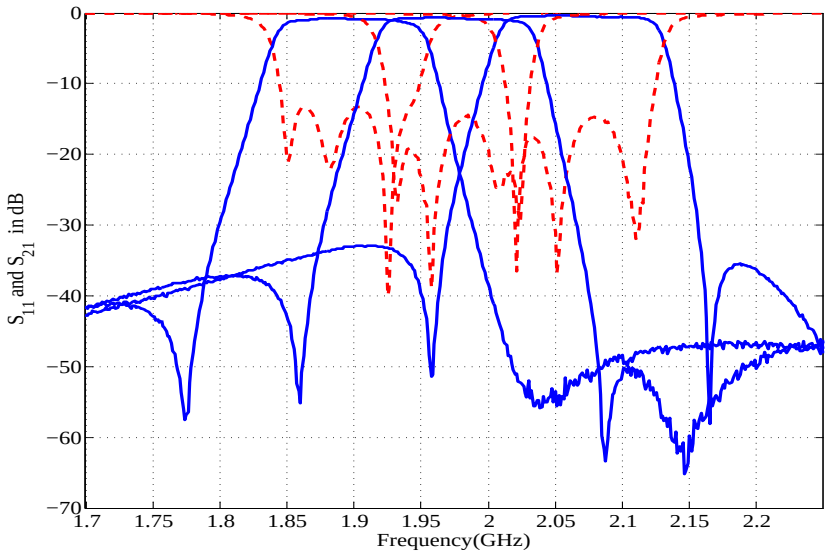

Figure 5.16: Measurement results for the first band elliptic filter across the tuning range.

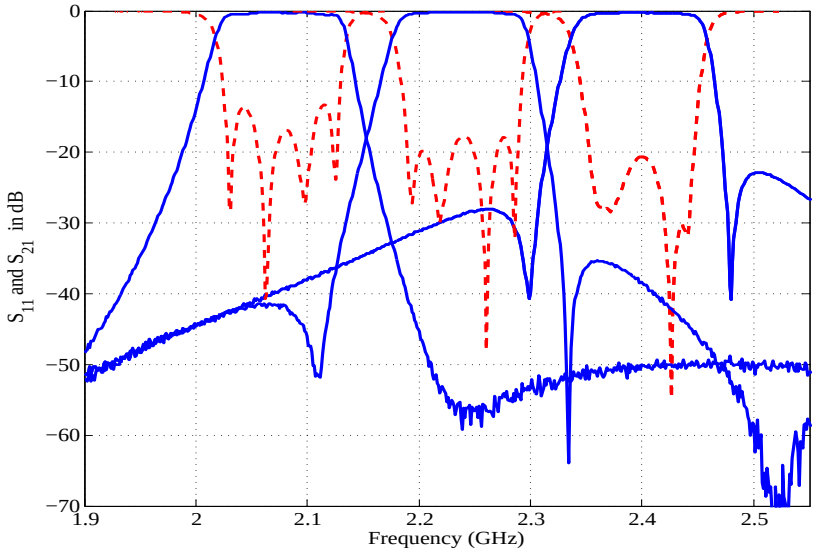

Figure 5.17: Measurement results for the second band elliptic filter across the tuning range.

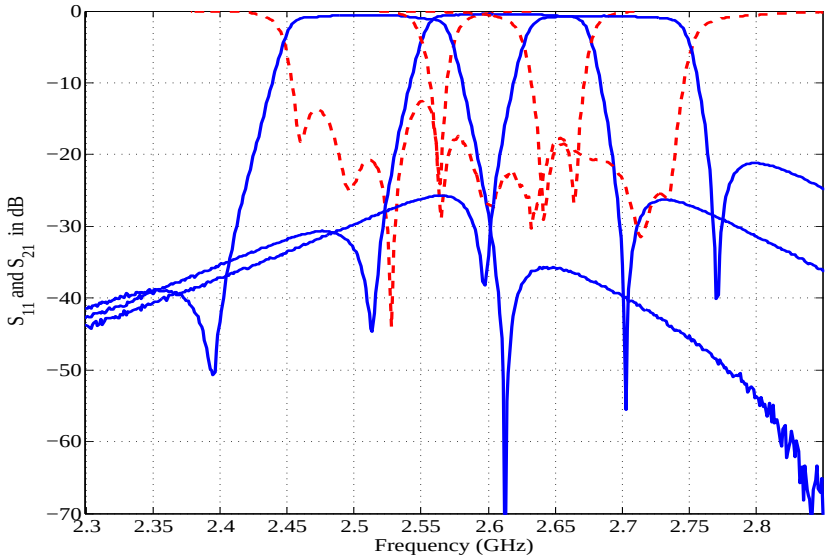

Figure 5.18: Measurement results for the third band elliptic filter across the tuning range.

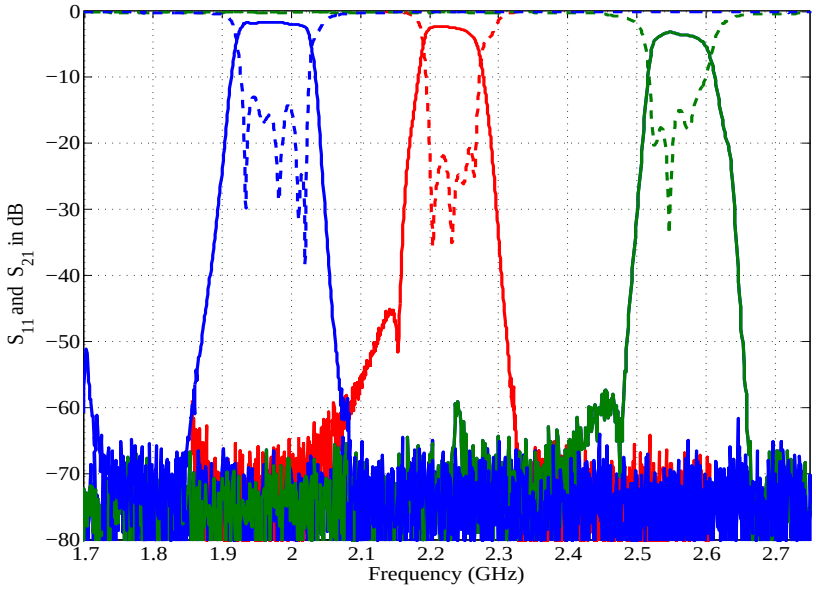

Figure 5.19: The measured cascaded response of all three bands.

5.5 Manifold Design

There are different configurations for design and implementation of multiplexing networks including hybrid-coupled, circulator coupled, directional filter, and manifold-coupled multiplexer. Since insertion loss and design size are our main concerns in this design, the manifold-coupled configuration seems to be the best option [49].

Manifold-coupled multiplexer is not usually amenable to flexible frequency structure; however, due to the small tuning range of each band, one can safely assume that the manifold response remains approximately constant across the tuning range. To see this, one can compare the wavelength variations across the tuning range to the centre wavelength of each band. Assuming a tuning range of $[f_0 - \Delta f/2, f_0 + \Delta f/2$, this ratio is given by

$$\Delta\lambda \approx -\frac{c\,\Delta f}{2f_0^2} \quad \rightarrow \quad \frac{\Delta\lambda}{\lambda_0} \approx -\frac{\Delta f}{2f_0}, \tag{5.1}$$

which for a tuning range of $\Delta f = 250$ MHz and the lowest centre frequency $f_0 = 1.97$ GHz yields 6.34% wavelength variation which is fairly small.

In this design, the combiner and channelizer are realized using coaxial manifolds. Manifold coupled multiplexer design requires the presence of all the channel filters so that the effect of channel interactions can be compensated in the manifold design process [49]. After designing six tunable combline filters, the next step is to find the manifold dimensions. Different analytical methods have been proposed to find the manifold lengths [34]. In this section, the numerical optimization method is used. To this aim, the equivalent circuit model of six filters are connected to each other through coaxial manifolds at the input and output in ADS. Then, numerical optimization algorithms are used to find the optimum manifold lengths that yield an acceptable return loss at the middle frequency point of each band. The optimization parameters include the length of the manifolds, the self-coupling values of the first resonator of three high-pass filters, and the self-coupling values of the last resonators of three low-pass filters. The optimized manifold response in ADS is depicted in Fig. 5.20. One can see from this figure that the return loss is better than 13 dB in

all three bands and there is an acceptable isolation between different bands. The centrer frequency of different bands are 1.97, 2.25, and 2.5 GHz and they have the same bandwidth of approximately 80 MHz. Hereafter, it is assumed that the manifold lengths are fixed to their optimal values.

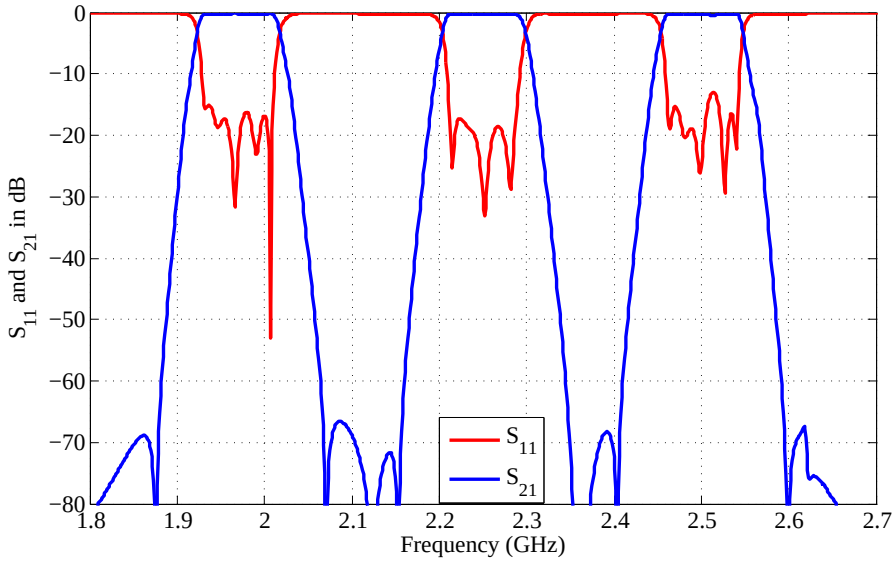

Figure 5.20: Two port triplexer response in ADS circuit simulator using optimized manifold lengths.

5.6 Simulation Results

In a fully tunable two port triplexer, the centre frequency and bandwidth of each band should be independently tunable. In this section, we test the tunability of the proposed two port triplexer using a circuit simulation in ADS. To this end, six tunable filters are connected to each other by input/output manifolds with the dimensions found in the previous section. The centre frequency and bandwidth of each band are tuned by changing

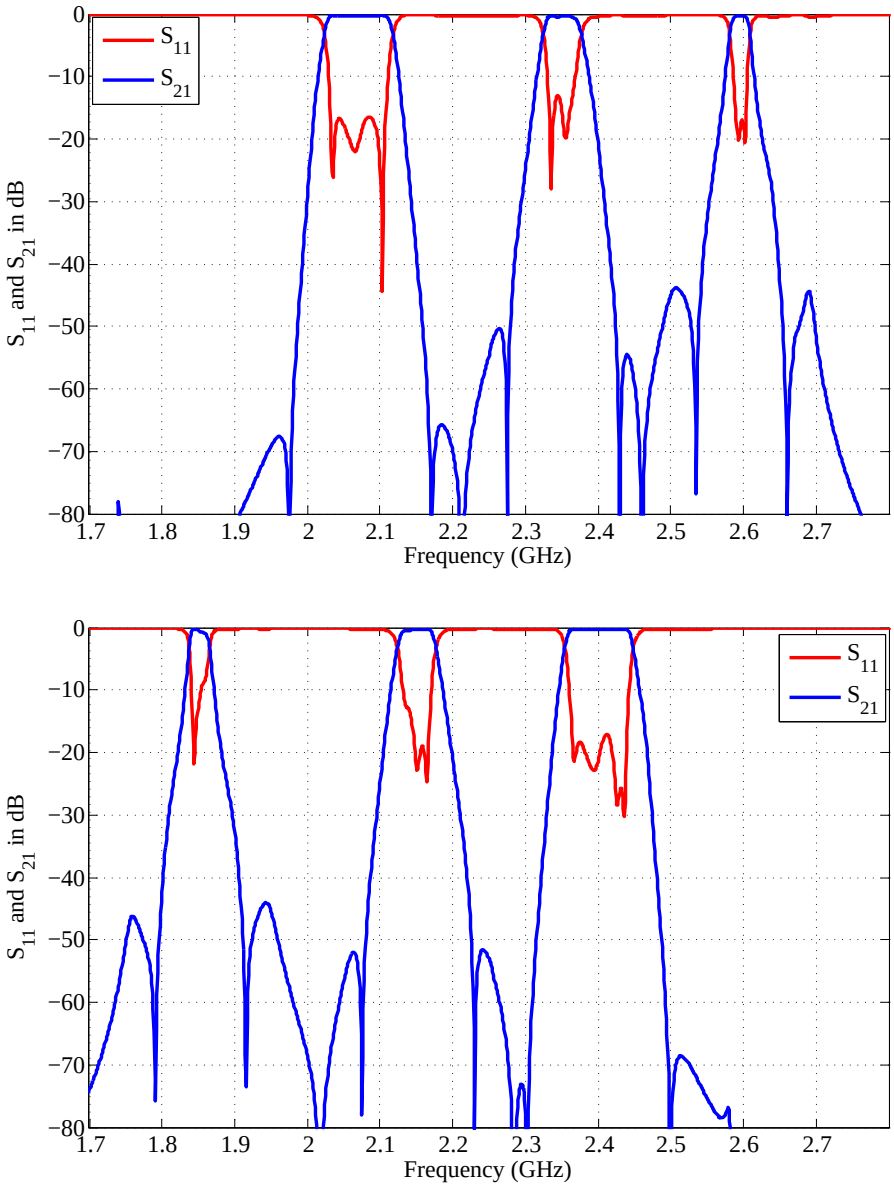

Figure 5.21: Bandwidth and centre frequency tuning of the two port triplexer in ADS circuit simulator.

the centre frequency of its corresponding low-pass and high-pass filters. The full tunability of the two port triplexer is demonstrated in Fig. 5.21. One can observe from Fig. 5.21 that the filter exhibits a good performance in terms of wide continuous tunability.

5.7 Conclusions

A fully tunable two port triplexer was proposed. The structure consists of three fully tunable bandpass filters connected to each other by a channelizer at the input and a combiner at the output. Using concentration of rejection, each filter exhibited two transmission zeros near its passband edges creating high inter-band isolation. The design concept was verified using ADS circuit simulator where the proposed filter demonstrated good insertion loss and passband selectivity. The small form factor and good power handling capability makes this structure a good candidate for wireless communication systems.

Chapter 6

Conclusions

6.1 Contributions

In this dissertation, we studied theoretical and practical aspects of fully tunable bandpass filters and two-port multiplexers. We selected 3D combline cavity structures to implement fully tunable filters as they can provide high Q and good power handling capability. Compare to a fixed bank of filters, a well-designed fully tunable filter can offer substantial advantages in terms of system performance and complexity.

In Chapter 3, we studied the design of constant absolute bandwidth tunable filters. Following the methodology developed in [1] based on optimizing the position of horizontal irises, we first designed and implemented a 5-pole C-band Chebyshev tunable filter with 40 MHz bandwidth and frequency tuning range of $4.9 - 6$ GHz. The fabricated filter exhibited a stable response over the tuning range with a bandwidth variation of $\pm 5.3\%$. Since horizontal irises could not provide the fairly large coupling values required in large bandwidth filters, we considered the use of other iris geometries to achieve constant absolute bandwidth in these filters. Relative to horizontal irises, semi-vertical irises can provide larger coupling values and they can offer constant absolute bandwidth using the same

optimization technique. We used semi-vertical irises to realized adjacent coupling values in a 7-pole X-band Chebyshev tunable filter with 80 MHz bandwidth and frequency tuning range of $7 - 7.9$ GHz. The fabricated filter exhibited a stable response over the tuning range with a bandwidth variation of $\pm 6.7\%$. We also showed that using vertical irises, the normalized coupling values remain almost independent of the cavity resonant frequency. This is in contrast to horizontal or semi-vertical irises where a tedious optimization is required to achieve the same goal. Since vertical irises can also provide versatile coupling values, they are the best candidates to realize constant absolute bandwidth tunable filters.

In Chapter 4, we considered the design of fully tunable bandpass filters with a wide tuning range. The bandwidth tunability was achieved by cascading two tunable filters. Since the tuning range was wide, each individual tunable filter can not be designed to have a constant absolute bandwidth. To achieve the wide tuning range requirement, we introduced the concept of constant return loss design. Constant return loss filters are a more general class of filters compared to constant absolute bandwidth filters as the bandwidth could change over the tuning range. To realize a constant return loss filter, all inter-resonator coupling elements as well as normalized input and output impedances need to scale with the same factor. We showed that this requirement can be achieved by careful design of filter geometry. In specific, we designed and implemented a constant return loss 6-pole tunable Chebyshev filter with tuning range of $1.8 - 2.6$ GHz. The bandwidth variation over the tuning range was $\pm 12.8\%$. Despite the large bandwidth variation, the return loss of the fabricated filter was better than 15 dB over the tuning range. Two of such filters were then cascaded by an isolator to provide the bandwidth tunability. The cascaded response revealed a tunable bandwidth of $20 - 100$ MHz.

The focus of Chapter 5 was on the design of two-port triplexers. Three fully tunable bandpass filters were connected to input and output manifolds to form a two-port triplexer. Manifold dimensions were optimized in ADS circuit simulator. It was shown that the bandwidth and centre frequency of each band can be independently tuned in the final structure.

6.2 Future Work

This dissertation can be followed in different directions, some of which are highlighted as follows:

As it was demonstrated, inductive coupling elements can be designed to be frequency independent by using carefully designed horizontal/semi-vertical or vertical irises. Capacitive coupling elements, on the other hand, do not easily lend themselves to a resonant-frequency independent design. An interesting future research direction would be to develop a similar methodology for the design of constant capacitive coupling elements.

The fully tunable two-port triplexer was realized using three individual fully tunable filters. An alternative approach would be to design a single fully tunable multi-band filter. Unlike the Chebyshev filters whose polynomial representation and synthesis are well established, little is known about multi-band filters. Furthermore, individual tuning of different bands in such multi-band design would be an interesting research problem.

APPENDICES

Appendix A

TULA motor control

The assembled TULA70-250 motor is shown in Fig. A.1. The mobile part is fixed between two metal plates. When a driving voltage is applied, the shaft moves upward/downward. Two methods can be used to actuate and control the motor:

- **Using the TULA controller (EV-KIT)**: This device is connected to the PC and can be controlled from inside Matlab. The Matlab code will be presented next.
- **Using a signal generator**: A square or ramp signal with a peak voltage of 1.2 V and a frequency between $20 - 150$ KHz is generated using the signal generator. Since the TULA motor working voltage should be between $10 - 30$ V, a piezo-amplifier is used to amplify the voltage by a factor of 10 to create a suitable drive voltage for TULA motor. The motor is controlled by changing the frequency and duty ratio of the driving voltage signal. For fine tuning, the burst mode of the signal generator can be used.

In the following, the Matlab code which is used to tune the TULA motor is presented:

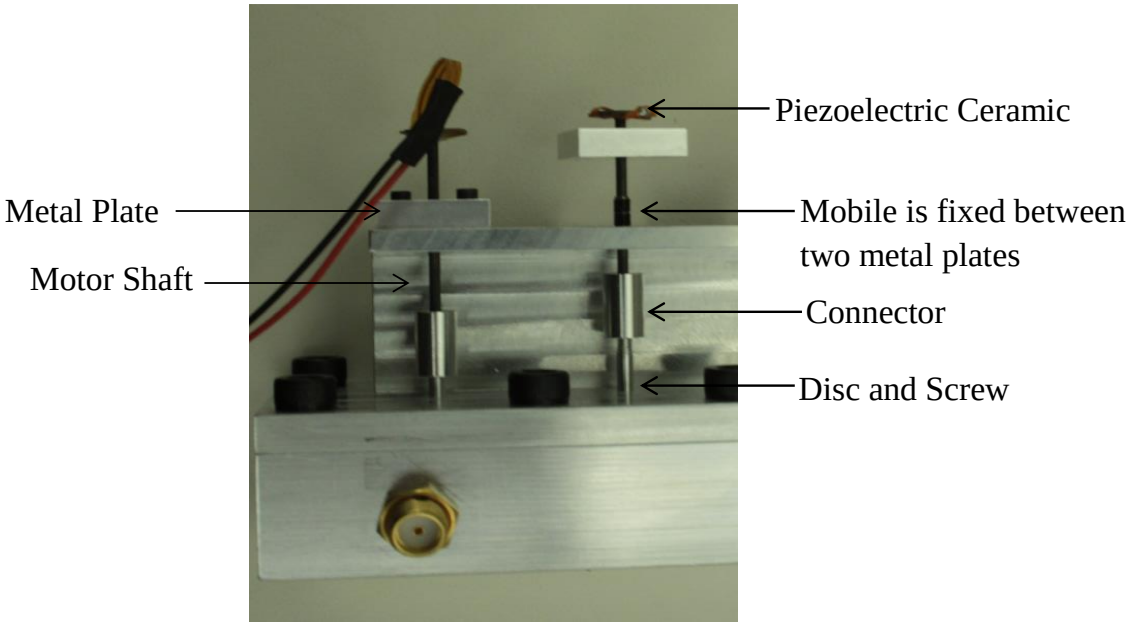

Figure A.1: Piezoelectric motor assembled on top of the resonator.

```
clc;clear all;
delete(instrfind);
%--Create the serial object
serialPort = {'/dev/tty.usbserial-A4003ODA'};
%--Set up 9600 8-N-1 on serial port
s = serial(serialPort,'BaudRate',19200,'DataBits',8,'Parity','none','StopBits',1);
s.InputBufferSize = 2048;
s.Terminator = 'CR';
fopen(s);
s.ReadAsyncMode = 'continuous';
fprintf(s, '>101');%online mode
fprintf(s, '>2220');%voltage
fprintf(s, '>120');%time mode
```

```
fprintf(s, '>2059000');%frequency (hz)
fprintf(s, '>2128');%duty cycle (%)
%fprintf (s, '>3029');
for i=1:8
    fprintf (s, '>313.2');%move up
    pause(1);
end
for i=1:1
    fprintf (s, '>323.2');%move down
end
fprintf (s, '>100'); %manual mode
fclose(s);
delete(s);
```

Bibliography

[1] H. Fengxi, *High Q tunable filters*. PhD thesis, University of Waterloo, 2012.

[2] R. Mansour, F. Huang, S. Fouladi, W. Yan, and M. Nasr, "High-q tunable filters: Challenges and potential," *Microwave Magazine, IEEE*, vol. 15, no. 5, pp. 70–82, 2014.

[3] R. J. Cameron, C. M. Kudsia, and R. R. Mansour, *Microwave filters for communication systems*. Wiley-Interscience, 2007.

[4] S. Fouladi, F. Huang, W. D. Yan, and R. Mansour, "Combline tunable bandpass filter using rf-mems switched capacitor bank," in *Microwave Symposium Digest (MTT), 2012 IEEE MTT-S International*, pp. 1–3, IEEE, 2012.

[5] J. Uher and W. J. Hoefer, "Tunable microwave and millimeter-wave band-pass filters," *Microwave Theory and Techniques, IEEE Transactions on*, vol. 39, no. 4, pp. 643–653, 1991.

[6] T. Shen, K. A. Zaki, and C. Wang, "Tunable dielectric resonators with dielectric tuning disks," *Microwave Theory and Techniques, IEEE Transactions on*, vol. 48, no. 12, pp. 2439–2445, 2000.

[7] S. Fouladi, F. Huang, W. D. Yan, and R. R. Mansour, "High-narrowband tunable combline bandpass filters using mems capacitor banks and piezomotors," *Microwave Theory and Techniques, IEEE Transactions on*, vol. 61, no. 1, pp. 393–402, 2013.

[8] M.Iskander, M. Nasr, and R. R. Mansour, "High-q tunable combline bandpass filter using angular tuning technique,." in Proc.European Microwave Symp. 201, to be published.

[9] J. Krupka, A. Abramowicz, and K. Derzakowski, "Magnetically tunable filters for cellular communication terminals," *Microwave Theory and Techniques, IEEE Transactions on*, vol. 54, no. 6, pp. 2329–2335, 2006.

[10] B.-W. Kim and S.-W. Yun, "Varactor-tuned combline bandpass filter using step-impedance microstrip lines," *Microwave Theory and Techniques, IEEE Transactions on*, vol. 52, no. 4, pp. 1279–1283, 2004.

[11] L. Dussopt and G. M. Rebeiz, "Intermodulation distortion and power handling in rf mems switches, varactors, and tunable filters," *Microwave Theory and Techniques, IEEE Transactions on*, vol. 51, no. 4, pp. 1247–1256, 2003.

[12] S.-J. Park, K.-Y. Lee, and G. M. Rebeiz, "Low-loss 5.15&# 8211; 5.70-ghz rf mems switchable filter for wireless lan applications," *Microwave Theory and Techniques, IEEE Transactions on*, vol. 54, no. 11, pp. 3931–3939, 2006.

[13] A. Abbaspour-Tamijani, L. Dussopt, and G. M. Rebeiz, "Miniature and tunable filters using mems capacitors," *Microwave Theory and Techniques, IEEE Transactions on*, vol. 51, no. 7, pp. 1878–1885, 2003.

[14] D. Peroulis, S. Pacheco, K. Sarabandi, and L. P. Katehi, "Tunable lumped components with applications to reconfigurable mems filters," in *Microwave Symposium Digest, 2001 IEEE MTT-S International*, vol. 1, pp. 341–344, IEEE, 2001.

[15] I. Hunter and J. D. Rhodes, "Electronically tunable microwave bandpass filters," *Microwave Theory and Techniques, IEEE Transactions on*, vol. 30, no. 9, pp. 1354–1360, 1982.

[16] S.-J. Park and G. M. Rebeiz, "Low-loss two-pole tunable filters with three different predefined bandwidth characteristics," *Microwave Theory and Techniques, IEEE Transactions on*, vol. 56, no. 5, pp. 1137–1148, 2008.

[17] G. L. Matthaei, "Narrow-band, fixed-tuned, and tunable bandpass filters with zig-zag hairpin-comb resonators," *Microwave Theory and Techniques, IEEE Transactions on*, vol. 51, no. 4, pp. 1214–1219, 2003.

[18] G. Tsuzuki, M. Hernandez, E. M. Prophet, S. Jimenez, and B. A. Willemsen, "Ultra-selective constant-bandwidth electromechanically tunable hts filters," in *2006 IEEE MTT-S Int. Symp. Dig., San Francisco, CA*, pp. 693–696, 2006.

[19] H. Joshi, H. H. Sigmarsson, S. Moon, D. Peroulis, and W. J. Chappell, "High-fully reconfigurable tunable bandpass filters," *Microwave Theory and Techniques, IEEE Transactions on*, vol. 57, no. 12, pp. 3525–3533, 2009.

[20] B. Yassini, M. Yu, D. Smith, and S. Kellett, "A-band high-tunable filter with stable tuning response," *Microwave Theory and Techniques, IEEE Transactions on*, vol. 57, no. 12, pp. 2948–2957, 2009.

[21] C.-C. Cheng and G. M. Rebeiz, "High-4–6-ghz suspended stripline rf mems tunable filter with bandwidth control," *Microwave Theory and Techniques, IEEE Transactions on*, vol. 59, no. 10, pp. 2469–2476, 2011.

[22] I. Reines, A. Brown, M. El-Tanani, A. Grichener, and G. Rebeiz, "1.6-2.4 ghz rf mems tunable 3-pole suspended combline filter," in *Microwave Symposium Digest, 2008 IEEE MTT-S International*, pp. 133–136, IEEE, 2008.

[23] A. Abunjaileh and I. Hunter, "Combline filter with tunable bandwidth and centre frequency," in *Microwave Symposium Digest (MTT), 2010 IEEE MTT-S International*, pp. 1476–1479, IEEE, 2010.

[24] B. Yassini, M. Yu, and B. Keats, "A Ka-band fully tunable cavity filter," *Microwave Theory and Techniques, IEEE Transactions on*, vol. 60, no. 12, pp. 4002–4012, 2012.

[25] J. Rhodes and R. Levy, "A generalized multiplexer theory," *Microwave Theory and Techniques, IEEE Transactions on*, vol. 27, no. 2, pp. 99–111, 1979.

[26] C. Kudsia, R. Cameron, and T. WAI-CHEUNG, "Innovations in microwave filters and multiplexing networks for communications satellite systems," *IEEE transactions on microwave theory and techniques*, vol. 40, no. 6, pp. 1133–1149, 1992.

[27] M. Guglielmi, "Simple cad procedure for microwave filters and multiplexers," *Microwave Theory and Techniques, IEEE Transactions on*, vol. 42, no. 7, pp. 1347–1352, 1994.

[28] K. Saitou and K. Kageyama, "Tunable duplexer having multilayer structure using ltcc," in *Microwave Symposium Digest, 2003 IEEE MTT-S International*, vol. 3, pp. 1763–1766, IEEE, 2003.

[29] T. Yang and G. M. Rebeiz, "Three-pole 1.3–2.4-ghz diplexer and 1.1–2.45-ghz dual-band filter with common resonator topology and flexible tuning capabilities," 2013.

[30] C.-F. Chen, C.-Y. Lin, B.-H. Tseng, and S.-F. Chang, "A compact tunable microstrip diplexer using varactor-tuned dual-mode stub-loaded resonators," in *Microwave Symposium (IMS), 2014 IEEE MTT-S International*, pp. 1–3, IEEE, 2014.

[31] R. Kihlén, "Stripline triplexer for use in narrow-bandwidth multichannel filters," 1972.

[32] T. Ohno, K. Wada, and O. Hashimoto, "A class of a planar triplexer by manipulating multiple attenuation poles," in *Microwave Conference, 2004. 34th European*, vol. 2, pp. 625–628, IEEE, 2004.

[33] H. Joshi, H. H. Sigmarsson, S. Moon, D. Peroulis, and W. J. Chappell, "Tunable high q narrow-band triplexer," in *Microwave Symposium Digest, 2009. MTT'09. IEEE MTT-S International*, pp. 1477–1480, IEEE, 2009.

[34] P. Laforge, *Tunable Superconducting Microwave Filters*. PhD thesis, University of Waterloo, 2010.

[35] F. Huang, S. Fouladi, M. Nasr, and R. R. Mansour, "Three dimensional tunable filters with absolute constant bandwidth." Patent Pending.

[36] J. W. Bandler, R. Biernacki, S. H. Chen, R. H. Hemmers, and K. Madsen, "Electromagnetic optimization exploiting aggressive space mapping," *Microwave Theory and Techniques, IEEE Transactions on*, vol. 43, no. 12, pp. 2874–2882, 1995.

[37] J. W. Bandler, R. Biernacki, S. H. Chen, and Y. F. Huang, "Design optimization of interdigital filters using aggressive space mapping and decomposition," *Microwave Theory and Techniques, IEEE Transactions on*, vol. 45, no. 5, pp. 761–769, 1997.

[38] F. C. Chen, Q. X. Chu, and J. S. Yang, "An improved group-delay approach to the tuning of coupled-resonators fiilter," in *Microwave and Millimeter Wave Technology, 2007. ICMMT'07. International Conference on*, pp. 1–4, IEEE, 2007.

[39] J. B. Ness, "A unified approach to the design, measurement, and tuning of coupled-resonator filters," *Microwave Theory and Techniques, IEEE Transactions on*, vol. 46, no. 4, pp. 343–351, 1998.

[40] H.-P. Ko, S. Kim, S. N. Borodinas, P. E. Vasiljev, C.-Y. Kang, and S.-J. Yoon, "A novel tiny ultrasonic linear motor using the radial mode of a bimorph," *Sensors and Actuators A: physical*, vol. 125, no. 2, pp. 477–481, 2006.

[41] H.-P. Ko, C.-Y. Kang, J.-S. Kim, S. N. Borodin, S. Kim, and S.-J. Yoon, "Constructions and characteristics of a tiny piezoelectric linear motor using radial mode vibrations," *Journal of electroceramics*, vol. 17, no. 2-4, pp. 603–608, 2006.

[42] R. Snyder, "Coupling probe having an adjustable tuning conductor," Aug. 2 2005. US Patent 6,924,718.

[43] M. Sánchez-Renedo, R. Gómez-García, J. I. Alonso, and C. Briso-Rodríguez, "Tunable combline filter with continuous control of center frequency and bandwidth," *Microwave Theory and Techniques, IEEE Transactions on*, vol. 53, no. 1, pp. 191–199, 2005.

[44] R. Gómez-García, M. Sanchez-Soriano, K. Tam, and Q. Xue, "Flexible filters: Reconfigurable-bandwidth bandpass planar filters with ultralarge tuning ratio," *Microwave Magazine, IEEE*, vol. 15, no. 5, pp. 43–54, 2014.

[45] G. Chaudhary, Y. Jeong, and J. Lim, "Dual-band bandpass filter with independently tunable center frequencies and bandwidths," *Microwave Theory and Techniques, IEEE Transactions on*, vol. 61, no. 1, pp. 107–116, 2013.

[46] J. B. Thomas, "Cross-coupling in coaxial cavity filters-a tutorial overview," *Microwave Theory and Techniques, IEEE Transactions on*, vol. 51, no. 4, pp. 1368–1376, 2003.

[47] M. El Sabbagh, K. A. Zaki, H.-W. Yao, and M. Yu, "Full-wave analysis of coupling between combline resonators and its application to combline filters with canonical configurations," *Microwave Theory and Techniques, IEEE Transactions on*, vol. 49, no. 12, pp. 2384–2393, 2001.

[48] R. J. Cameron, A. Harish, and C. J. Radcliffe, "Synthesis of advanced microwave filters without diagonal cross-couplings," *Microwave Theory and Techniques, IEEE Transactions on*, vol. 50, no. 12, pp. 2862–2872, 2002.

[49] R. J. Cameron and M. Yu, "Design of manifold-coupled multiplexers," *Microwave Magazine, IEEE*, vol. 8, no. 5, pp. 46–59, 2007.